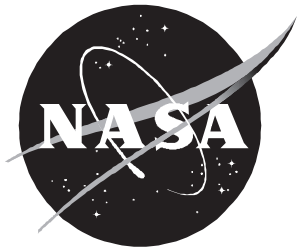

NASA Contractor Report 4781

The Joint Damping Experiment (JDX)

Steven L. Folkman, Jeff G. Bingham, Jess R. Crookston, Joseph D. Dutson, Brook D. Ferney, Greg D. Ferney, and Edwin A. Rowsell

Contract NAS1-19418
Prepared for Langley Research Center

June 1997

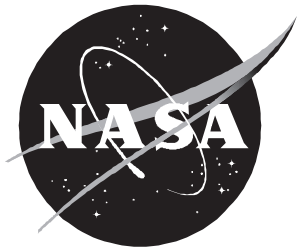

NASA Contractor Report 4781

The Joint Damping Experiment (JDX)

Steven L. Folkman, Jeff G. Bingham, Jess R. Crookston, Joseph D. Dutson, Brook D. Ferney, Greg D. Ferney, and Edwin A. Rowsell
Utah State University • Logan, Utah

National Aeronautics and Space Administration
Langley Research Center • Hampton, Virginia 23681-0001

Prepared for Langley Research Center
under Contract NAS1-19418

June 1997

Available electronically at the following URL address: http://techreports.larc.nasa.gov/ltrs/ltrs.html

Printed copies available from the following:

NASA Center for AeroSpace Information
800 Elkridge Landing Road
Linthicum Heights, MD 21090-2934
(301) 621-0390

National Technical Information Service (NTIS)
5285 Port Royal Road
Springfield, VA 22161-2171
(703) 487-4650

TABLE OF CONTENTS

1.0 SUMMARY 1
2.0 INTRODUCTION 2
2.1 Experiment Description 2
2.2 Mission Objectives 3
2.3 Literature Review 4
3.0 EXPERIMENT DESIGN 6
3.1 Strut Design 8
3.2 Tip Mass and Base Plate 11
3.3 Excitation System and Locking Mechanism 14
3.4 Experiment Controller, Data Acquisition, and Power 15
3.5 Truss Assembly 17
4.0 GROUND TESTING 17
4.1 Ground Testing Setup 18
4.2 Joint Gap Sizes and Pin Selection 21
4.3 Baseline Testing 28
4.4 Cold Cell Testing 32
5.0 LOW-G AIRCRAFT TESTING 34
6.0 TORSION MODE GROUND AND LOW-G TEST RESULTS 37
7.0 SPACE FLIGHT TESTING 41
7.1 Modeling of Bridge Coupling 43
7.2 Flight Results 46
7.3 Postflight Ground Testing 49
8.0 STRUT CHARACTERIZATION TESTS 51
8.1 Experimental Setup 51
8.2 Force State Map Results 53
8.3 Finite Element Modeling Development 57
9.0 NONLINEAR FINITE ELEMENT MODEL OF THE JDX TRUSS 62
9.1 Determination of Model Parameters from Force-State Map Test Results 64
9.2 Finite Element Model of the Truss 68
10.0 CONCLUSIONS 76
10.1 Recommendations for Future Work 78
11.0 REFERENCES 79
APPENDIX B - ELECTRICAL DIAGRAM FOR JDX 86
APPENDIX C - JDX FLIGHT MODEL TRUSS TWANG TESTS 88
APPENDIX D - LOGARITHMIC DECREMENT CURVES 102

ACKNOWLEDGMENTS

The authors would like to acknowledge the valuable contributions of the following individuals who assisted in this effort. Mark Lake of NASA LaRC was technical advisor throughout this project was always willing to assist in every aspect and he provided many valuable suggestions. Burton Lightner and Sherwin Beck of NASA LaRC, Project Managers during the project, provided very valuable guidance and suggestions. Technical assistance was provided by Gordon May, Terry Zollinger, and David Jones at Utah State University on the truss design and fabrication of the experiment. USU's Space Dynamics Laboratory Machine Shop were provided guidance in fabrication and did a very good job with the high precision fabrication of the truss. We also with to thank the students who are not listed as authors, but have assisted in this effort. They include Henry Cieslak, Paul Wheelwright, Steven Strong, Brandon Ferney, and Ruth Moser.

1.0 SUMMARY

The Joint Damping Experiment (JDX) is an experiment to measure the influence of gravity on the structural damping of a three bay truss. JDX was a project funded by NASA's IN-STEP program and was administered through NASA Langley. All hardware development, ground testing, and data reduction was performed at Utah State University (USU). The JDX mission objectives were to develop a small-scale Shuttle flight experiment which allows researchers to:

1) Measure vibration damping of a small-scale, pin-jointed truss to determine how pin gaps give rise to gravity-dependent damping rates.
2) Evaluate the applicability of ground and low-g aircraft tests for predicting on-orbit behavior.
3) Evaluate the ability of current nonlinear finite element codes to model the dynamic behavior of the truss.

Two small trusses with joints which provide gravity dependent damping were constructed. The first truss is described as an Engineering Model truss. This truss was used to obtain an initial characterization of the truss behavior. Based on these results, the design of the second truss, described as the Flight Model truss, was modified so that we obtained a high precision truss which exhibited gravity dependent damping. Ground-based testing was completed to measure damping of the truss with 1-g loads. The experiment flew on the Space Shuttle Endeavor (STS-69) as Get Away Special (GAS) payload G-726, on September 7-18, 1995 to measure damping in a micro-gravity environment. The damping of the truss was inferred from relatively simple "Twang" tests conducted in orbit. A twang test is conducted by plucking the truss structure and then recording the decay of the oscillations. Low-g aircraft testing of this experiment was also used. The short time period and the vibration environment of an aircraft made low-g aircraft testing difficult. However, the flight testing on the Shuttle provided a needed reference point to verify the low-g aircraft test results.

If a truss structure utilizes pinned joints with clearance fit pins, the joints can become the significant source of damping in the structure if large preloads are not present in the structure. The measured data from the JDX truss clearly shows that as gravity induced preloads are decreased, damping increases. Friction and impacting in the joints are suspected to be primary mechanisms causing damping in the joints. Impacting is demonstrated by the observation of high frequency hash in the decay data. Driving of higher modes by impacting is suspected to be a significant source of damping. However, the measured data also confirms that friction damping is a significant factor. Measurements during low-g aircraft and Shuttle flight tests show that damping is further increased as gravity loads are removed from the structure. The above conclusions assume the truss has been carefully assembled so that no preloads are induced during assembly so that as gravity loads are removed, strut preloads go to zero and joints can traverse their deadband zone.

Observations from the test results are summarized as follows. 1) Damping rates can change by a factor of 3 to 8 as a result of simply changing the orientation of a truss. 2) The addition of a few pinned joints to a truss structure can increase the damping by a factor as high as 30. 3) Damping is amplitude dependent. 4) As gravity induced preloads become large (by orienting the long axis

of the truss perpendicular to the gravity vector) the damping is similar to a truss without pinned joints. 5) Impacting in joints drives higher modes in the structure. 6) The torsion mode disappears if gravity induced preloads are low. It is significant that a mode expected from a linear finite element model of a structure could disappear due to the presence of pinned joints.

An approach has been demonstrated which can successfully simulate the gravity dependent behavior of the JDX truss. Using nonlinear modeling techniques available in the program LS-DYNA3D, one can model the deadband, impacting, and friction characteristics of a clearance fit pinned joint. Although the approach outlined does have deficiencies, it is a significant step toward modeling structures with loose connections.

2.0 INTRODUCTION

An experiment titled the Joint Damping Experiment (JDX) has been developed by researchers at Utah State University (USU) to measure the influence of gravity on joint damping in a pin-jointed truss. The JDX project is funded through NASA's IN-Space Technology Experiments Program (IN-STEP), and flew on the Space Shuttle Endeavor on September 7-18, 1995 as a Get Away Special (GAS) payload. Flying JDX as a GAS payload allowed the experiment to perform tests in a microgravity environment.

2.1 Experiment Description

The JDX experiment consists of a small-scale, three-bay truss with clearance fit pinned joints. The truss is attached to a stiff base plate at one end to provide a cantilevered boundary condition. The opposite end of the truss is attached to a rigid plate or tip mass, which lowers the natural frequency of the truss. Tests designed to study the dynamic and damping characteristics of the truss are executed by exciting different modes of the truss and recording the free decay of the oscillations. These free decay tests are described here as twang tests. There are three different modes that can be excited. The first two modes of the truss are orthogonal bending modes. They are referred to as "bend 1" and "bend 2," and represent a rocking motion of the truss, in their respective directions, which are 90 degrees apart. The lacing of the struts in the truss is such that it separates the two bending modes into distinct frequencies that are easy to identify. The bending modes are excited by displacing the truss in a direction perpendicular to the long axis of the truss. The third mode is a torsional mode, and is excited by twisting the truss about the long axis. A truss called the "Engineering Model truss" was built to examine the general behavior of the truss and allow refinement of the design of the joints. Testing of the Engineering Model truss led to recommendations for changes in the design of several components of the Flight Model truss. The Flight Model truss is the final model of the truss and was the GAS payload that flew on the Space Shuttle.

Data gathered from these tests was analyzed to determine logarithmic decrement of the decay.

The logarithmic decrement is a measure of the damping present in the structure. The influence of gravity on damping was determined by comparing the logarithmic decrement data from tests conducted in different environments. Also, the acceleration time history measured from the free decay can be compared with predictions from nonlinear finite element models of the truss.

2.2 Mission Objectives

JDX was designed to: 1) Measure vibration damping of a small-scale, pin-jointed truss to determine how pin gaps give rise to gravity-dependent damping rates. 2) Evaluate the applicability of ground and low-g aircraft tests for predicting on-orbit behavior. 3) Evaluate the ability of current nonlinear finite element codes to model the dynamic behavior of the truss.

The first objective is to establish a correlation between joint pin gap and gravity dependent damping rates in pin-jointed trusses. Quantitatively the results reported here will only be applicable to the small-scale truss article tested. However, the results demonstrate qualitative behaviors that apply to any size structure. One of the early observations was that only a few pinned joints with very small pin gaps were needed in a structure to dramatically influence its behavior.

The second objective of this experiment was to correlate ground and low-g aircraft test results with on-orbit tests and to examine the ability to predict on-orbit damping from on-ground and low-g aircraft test results. It was shown that if a structure is oriented and/or supported during ground tests such that gravity induced preloads in the truss are minimal, the damping measured in those tests will be similar to microgravity tests. The low-g aircraft testing of this experiment was very successful. The short time period and the vibration environment of an aircraft made low-g aircraft testing difficult. However, it was found that only by free floating the experiment inside the aircraft cabin, good data could be obtained. However, the JDX truss requires a cantilevered boundary condition and this was only approximated in the free-float tests conducted inside the aircraft. Indeed, flight testing on the Shuttle provided the needed reference point to verify the accuracy of the low-g aircraft test results.

The third objective was to see if theoretical models can be used to accurately predict the truss dynamics and damping. From the standpoint of modeling, pinned joints add significant difficulties for precise modeling. Because of the "slop" in the joints and imprecision in the lengths of the joints, load paths become difficult to assess when the truss is lightly loaded. As the gaps in the joints close, the force/deflection characteristics of the truss become nonlinear. These pin jointed structures could be described as "a bunch of loose parts floating in space". The word "loose" is a term whose meaning is relative to some reference point. For an antenna whose shape is to be controlled to within a micron, a "loose" structure might be one with a few microns of "slop". An approach for modeling a structure with loose joints structure was developed and successfully simulated many of the observed truss characteristics.

2.3 Literature Review

The need for further research in the area of space structure damping has long been recognized by the scientific community. Nurre[1] recommended ground testing individual components of a structure in order to characterize complete structures and listed the following as key issues in structural dynamics testing.

1. Zero-g effects.
2. Low natural frequencies with high modal density.
3. Joint/interface characteristics.
4. Damping (distributed and lumped).

Joint damping models are usually obtained from two different damping mechanisms-- friction and impacting. Friction damping is attributed to rotary or extensional joint motions, while impacting occurs when two previously separated surfaces collide during the cycles of an oscillatory motion.

There are two models generally used to describe friction damping--macroslip and microslip. In macroslip damping, no damping is assumed to have occurred until there is relative motion between two surfaces. When this motion occurs the forces in the joint exceed the Coulomb friction forces acting parallel to the interface. Den Hartog[2] analyzed the classic friction model and showed that for small loads the energy dissipation increases linearly with the displacement. In microslip friction models there is no slippage between the surfaces and damping is assumed to occur because of localized, microscopic slippage. So while the joint remains "locked," surface imperfections cause the contact pressure to be distributed unevenly allowing localized slippage. Microslip friction is difficult to predict and as Plunket[3] reported we are still far from being able to predict damping due to this phenomena.

The damping due to impacting in a joint is also difficult to predict. It has been suggested by Crawley, Sigler, and Van Schoor[4] that one measure of energy dissipation could be the coefficient of restitution. However, the coefficient of restitution is not only dependent on the material properties, it is also dependent on the geometries of the surfaces involved in the impacting. For this reason coefficients of restitution are usually found through empirical study and a new study would be required for each joint configuration. At this time there are no general models available to describe the damping in pinned joints with “deadband” or gaps present.
Folkman and Redd[5] have shown the damping in a pinned joint structure is dominated by the pinned joints when deadband is present in the joints. Therefore, there is a need for ground testing on pinned, jointed structures to help verify the analytical models being developed to model these kinds of structures.

Mathematical models have been proposed which try to account for deadband and friction. Ferri[6] created a model of a nonlinear sleeve joint and concluded that the three major sources of energy dissipation were damping due to Coulomb friction, damping due to impact, and material damping. He also showed that the overall damping was similar to viscous damping. Lankarani and

Nikravesh[7] created a model for impacting of two elastic bodies. They concluded that energy dissipation during impact was a function of initial velocity, coefficient of restitution, and material properties. Tzou and Rong[8] presented a mathematical model of a three-dimensional spherical joint, which included the effects of friction and impacting. Onoda, Sano, and Minesugi[9] showed that impacting causes energy to be transferred from lower to higher modes. The excitation of higher modes results in greater structural damping. Folkman[10] created models for extensional friction damping, rotational friction damping, and impact damping.

In recent years force-state-mapping techniques have been used to characterize the dynamic properties of struts containing pinned joints.[11-13] Individual struts from a truss are subjected to dynamic loading and the resulting displacements, accelerations, and applied forces are measured. These data can be used to produce a map of the force-displacement-velocity domain. Parameters such as nonlinear stiffness and damping can then be obtained from this map for use in modeling the entire truss.

Several finite element analysis (FEA) programs are available that are capable of modeling the nonlinearities associated with impacting and friction.[14-17] MSC/NASTRAN is a FEA program that includes an adaptive gap element, the CGAP element, for modeling points that come into contact. The CGAP element can also be used to model macroslip between two bodies. Folkman attempted to use gap elements to model a truss with pinned joints but was unsuccessful.[10] Although numerous mathematical models of pinned joints have been developed, the literature does not describe attempts to model the dynamic response of pinned joints using commercial FEA programs.

3.0 EXPERIMENT DESIGN

The JDX project was designed to be flown as a GAS payload; therefore, the experiment is required to fit inside a GAS canister, which has a volume of five cubic feet. This limited the size of the components that make up the truss, excitation system, and data acquisition devices. The truss dimensions are nominally 24 inches by 8 inches by 8 inches. The truss has 34 struts connected to 16 hubs. A photograph of the truss is shown in Fig. 1. The tang and clevis portions of each strut are identical. However, the length of the strut tube connecting the two ends can be varied, depending on whether the strut is one of the 14 "cross" struts or 20 "primary" struts. Cross struts connect the hubs diagonally and have a tube length of 5.76 inches. Primary struts connect the hubs both horizontally and vertically, and have a tube length of 2.45 inches.

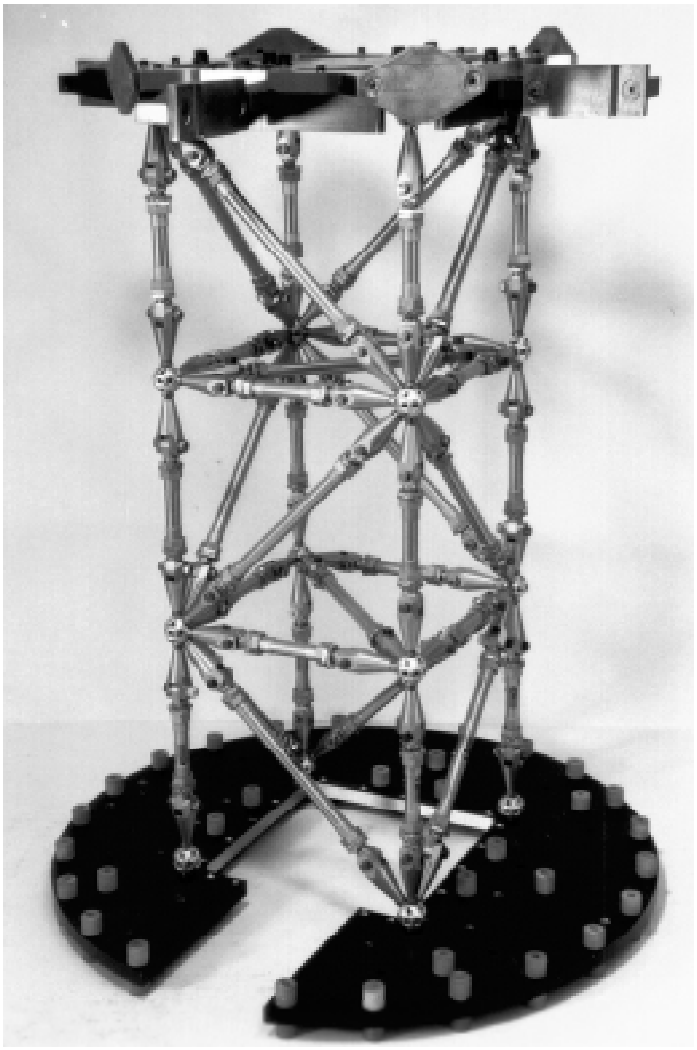

Fig. 1. Photograph of the truss.

Surrounding the truss are twelve 1.0-inch square aluminum support posts that run from the base plate to a top plate. These support posts provide mounting places for the experiment controller and data acquisition system, as well as portions of the excitation system. Figure 2 shows the framework of support posts and the top plate with the excitation system components attached. These posts also provided the structural support normally required by NASA for GAS payloads.[18] Also attached to the top plate are three bumpers. These bumpers provide lateral support for the experiment. Two of the bumpers are located at 90° to each other and the third is 135° from the first two. Figure 3 is an illustration of the bumper placement.

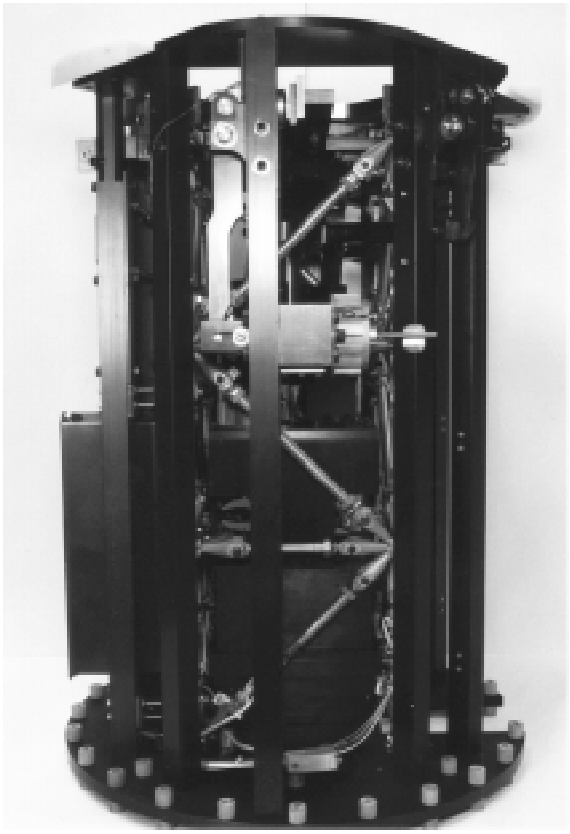

Fig. 2. Photograph of the framework posts which surround the truss.

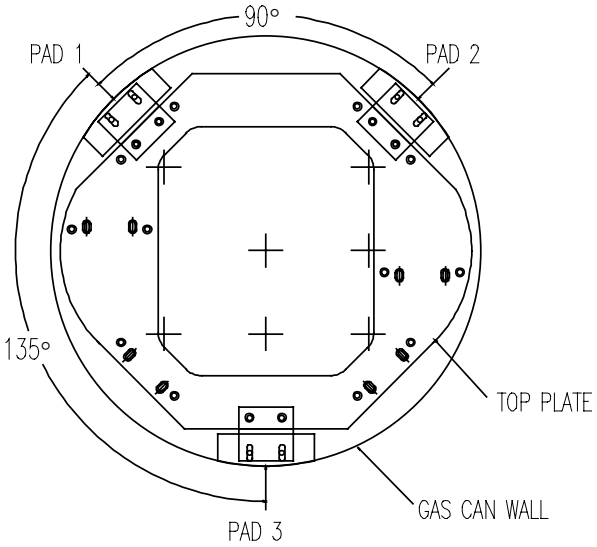

Fig. 3. Illustration of the bumper pads.

Because of the GAS payload volume constraints it was necessary to utilize the open space inside the truss. The battery box and remaining excitation system components are mounted in this space. Figure 4 illustrates the battery box/support box configuration. A sealed battery box was used in accordance with NASA GAS payload specifications.[19]

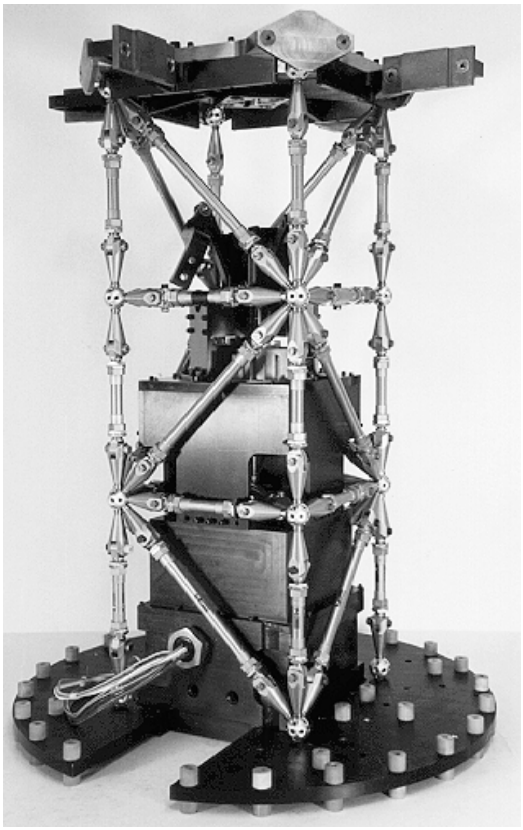

Fig. 4. Photograph showing the items located inside the truss bays.

3.1 Strut Design

The JDX Flight Model Strut is composed of two major parts: the strut tube or body, and the clevis/tang end attachments. This is seen in Fig. 5. All clevises, tangs, and strut bodies are made from 6061-T6 aluminum, and have been anodized with a gold color for cosmetic purposes. Each clevis/tang interface is connected by a pinned joint. The nature of this pinned joint varies according to the strut position in the truss. For all joints in the top two bays of the truss and all eight joints at the base plate, a 0.001-inch shim was placed between the clevis/tang interface, a 0.251-inch, shoulder bolt was pressed into the 0.250-inch holes, and a nut was tightened on the shoulder bolt. This system effectively locked 60 of the 68 joints, by first removing the joint deadband, and second by clamping the joint together to prevent rotations. This type of joint is described as a locked joint.

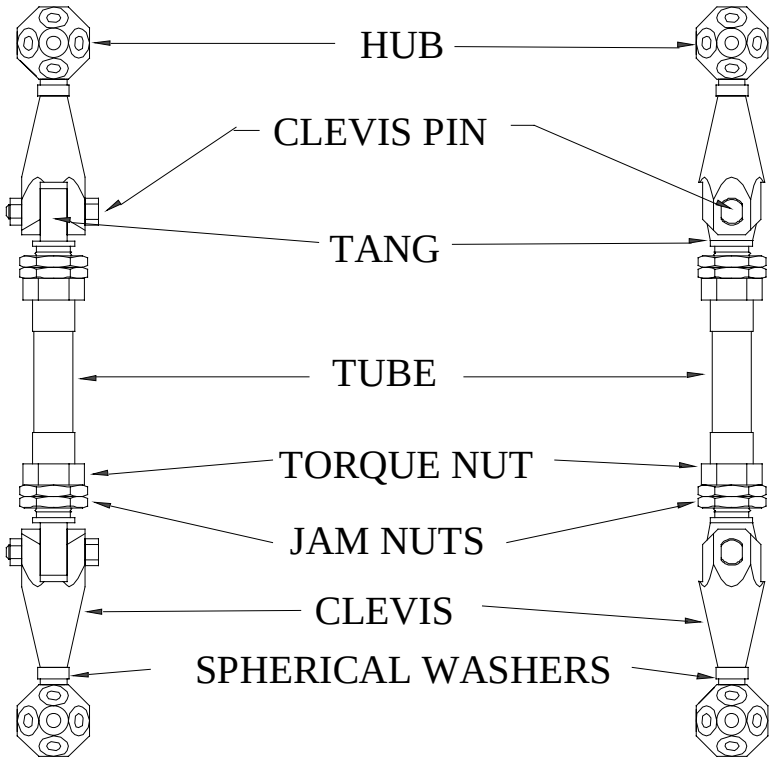

Fig. 5. Illustration of the strut design.

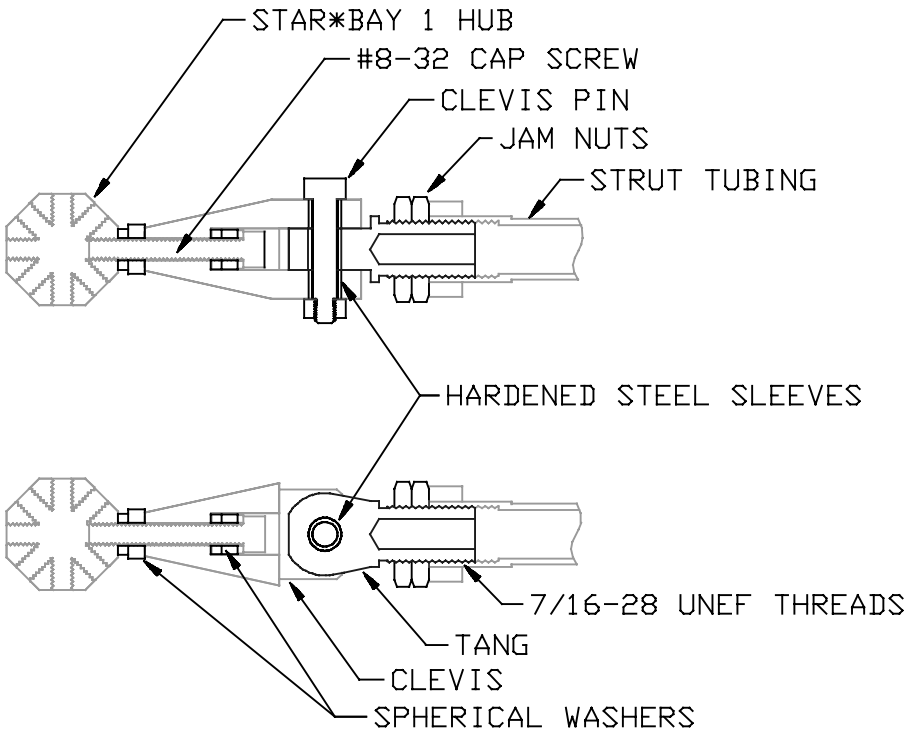

Fig. 6. Illustration of the pinned joint design.

The remaining eight joints are described as unlocked joints. To minimize joint wear, the unlocked joints have hardened steel sleeves, with inner diameters of 0.1875 inches and an outer diameter of 0.251 inches, press fit into the clevis/tang through holes. This gave the sleeves an interference fit of 0.001 inches. The sleeves were made from 1144 steel that was hardened to RC 32-34. It was imperative that the sleeves be inserted so as to maintain a precision alignment and avoid "out-of-round" effects. This was accomplished by heating the clevis or tang and then gently pressing the sleeve into the heat enlarged hole. Depending on the gap size desired, a hardened steel shoulder bolt with a shoulder diameter of 0.18635 inches to 0.18690 inches was used in the joint as the pin. All shoulder bolts were manufactured from 1144 stress-proof steel that had been hardened to RC 32-34. The same vendor (Carr Lane Manufacturing Co.) supplied both the sleeves and the shoulder bolts. An 8-32 UNC lock nut was placed on the end of each shoulder bolt but was tightened only enough to keep the shoulder bolt from vibrating out of the joint. No clamping force is applied by the lock nut to the joint and the joint is free to experience rotational motions. Figure 6 illustrates the unlocked joints.

An unlocked joint could be converted to a locked joint by installing a shim between the clevis and tang pieces and using an appropriately sized washer on the shoulder bolt. When the shoulder bolt is tightened, the clevis and tang faces are highly preloaded, preventing deadband and rotations from occurring in the joint.

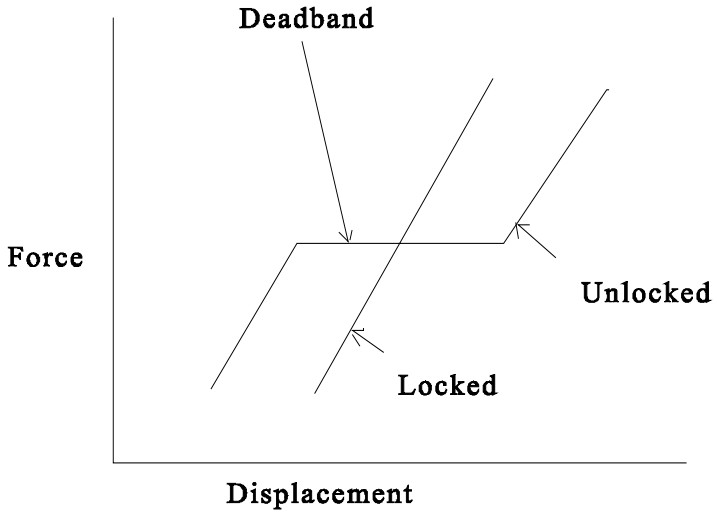

Fig. 7. Illustration of joint deadband effects on the force-displacement relationship of a strut.

The deadband in a joint is related to the amount of gap between the pin and the clevis and tang. When a joint moves slowly through the deadband region, no force would be transmitted by the joint. Figure 7 illustrates the conceptual force versus displacement relation for a locked and unlocked joint. The curve for the locked joint is linear and there is no movement through the deadband. The unlocked joint however exhibits nonlinear behavior as the joint moves through the deadband. It is seen that as the joint moves through the deadband the force is relatively constant while the displacement continues.

The strut tube has 7/16-28 UNEF internal threads at either end that provide attachment points for the tangs. These threaded connections also allow each strut length to be tailored to the length required to alleviate preloads in the joints. The threads at one end of the strut body are right-hand threads, and the threads at the other end are left- hand threads. This allows the strut tube to act as a turnbuckle, shortening or lengthening when turned. The strut tube is hollow and has an inside diameter of 0.370 inches. There are two different outer diameters because the strut is larger on the ends where it is threaded. The smaller diameter is 0.460 inches, whereas the larger diameter is 0.500 inches. A hexagonal torque nut was attached to each end of the strut tube, using Armstrong A-12 epoxy, so that a wrench could be used to adjust the strut length.

Attached to the end of both the locked and unlocked clevis/tang connections is a set of 18-8 stainless steel spherical washers. These washers help prevent misalignment in the joints that could cause preloads to be applied across the joint. During the truss assembly Armstrong A-12 epoxy was placed between the spherical washers to prevent them from slipping and thereby forming an additional source of damping in the joint.

Inside the clevis is a 1.25-inch 8-32 cap screw. This screw bolts the clevis to the hub. Another set of 18-8 stainless steel spherical washers is used to alleviate misalignments in the hub-clevis interface. These washers were also held in their preload free position by Armstrong A-12 epoxy.

The hubs used in the Flight Model truss are modified 1/4 scale Star-Bay hubs. The hubs were modified by removing eight of the original 26 mounting points since they were never used. All of the mounting points on the hubs have 8-32 locking threaded inserts placed in them. The inserts provide greater tensile strength than would have existed in a wholly aluminum hub, while also providing a locking mechanism for the clevis-hub interface. To provide another locking mechanism, Locktite brand thread locker was applied to the cap screw threads before they were screwed into the hubs.

Two 7/16-28 UNEF jam nuts were placed on each tang. The jam nuts were made from 18-8 stainless steel. The nuts were used to prevent the strut tube from rotating and thus fix the strut length. The jam nuts were also locked in place using Locktite brand thread locker.

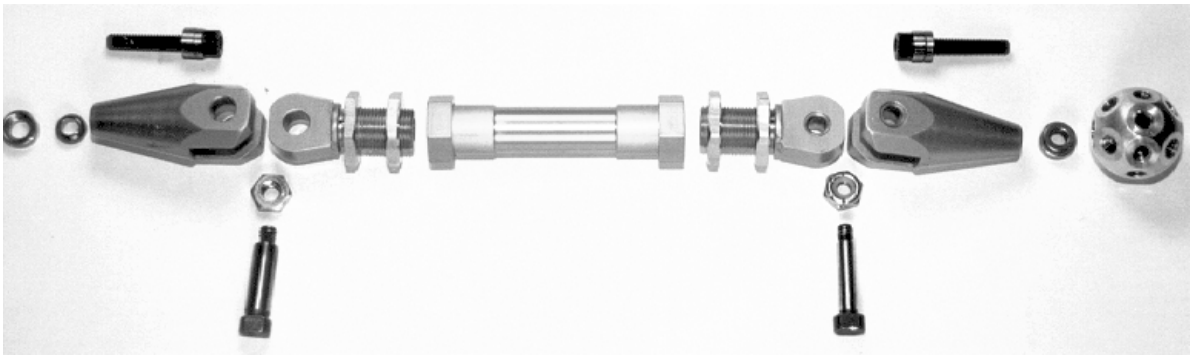

Fig. 8. Photograph of a strut.

Figure 8 is a photograph of a disassembled strut with one of the clevis/tang attachments having stainless steel inserts that would provide gap, and one clevis/tang attachment that would be locked. Appendix A contains additional drawings illustrating the strut design.

3.2 Tip Mass and Base Plate

Attached to the top and bottom of the Flight Model truss are respectively the tip mass and base plate. Figure 1 shows the truss attached to both the tip mass and the base plate. The base plate is a 0.5-inch thick 6061-T6 aluminum plate with a radius of 9.875 inches. Therefore, the base plate provides a cantilevered boundary condition for the truss since it bolts directly to the lid of the GAS can, which is called the GAS Experiment Mounting Plate (EMP). The base plate is bolted to the EMP by 36 10-32 UNC cap screws. These 36 points also provide thermal isolation for the experiment through the use of G-10 fiberglass epoxy spacers. The spacers have an outer diameter of 0.625 inches, an inner diameter of 0.25 inches, and are 0.65 inches long. A spacer is set on either side of each hole in the base plate as shown in Fig. 1. The G-10 spacers have a low thermal conductivity and thus lower the rate heat is lost by the experiment to deep space. The cap screws are locked in place through the use of safety wire. The wire is placed through holes drilled in the heads of the cap screw.

The base plate has a 4.01-inch wide by 6.475-inch deep section machined out to provide space for the battery box venting mechanism which is mounted to the EMP. There is also a 7.25 by 7.25-inch section machined out of the center of the plate to provide for easy battery box removal.

The stainless steel tip mass provides a mass at the free end of the truss that effectively lowers the natural frequency of the truss. Furthermore, the tip mass provides locations that can be used to excite the three fundamental truss modes. Each of the corners of the tip mass has a low carbon steel plate attached. These steel plates can be used to provide an attachment point for the excitation system's electromagnets. Four aluminum arms, each with a steel plate, were also attached to the tip mass to allow excitation of a truss torsion mode. Figure 9 illustrates the tip mass geometry and the four magnets used to excite the truss. Note that only four of the eight steel magnet plates are actually used by the excitation system. The four extra steel plates were attached to maintain the symmetry of the tip mass. The tip mass is made from 0.5-inch thick nonmagnetic stainless steel. A sleeve for locking the tip mass in place is attached underneath the tip mass view shown in Fig. 9. With all the attachments the weight of the tip mass is 15.3 pounds. This weight is sufficient to allow the weight of the truss to be neglected in analysis and still provide accurate results. Table 1 lists the measured mass distribution of the truss and tip mass. Table 2 gives a breakdown of the mass of the components making up the truss.

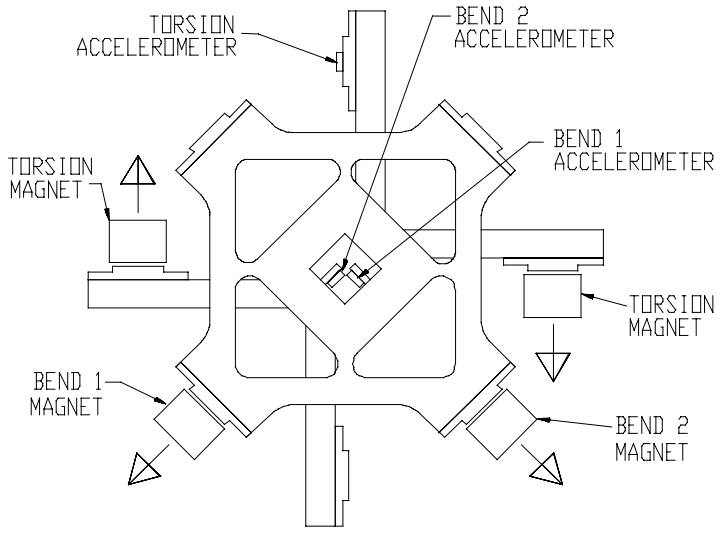

Fig. 9. Top view of the tip mass showing the magnets and the accelerometer locations.

Table 1. Truss mass summary.

Item	Weight (lb)
Truss (Hubs + Struts)	8.2
Tip Mass	10.0
Magnet Plates	3.1
Torsion Arms	1.8
Locker Sleeve	0.4

Table 2. Detailed mass breakdown of the truss and tip mass

Description	Quantity	Mass (g)	Mass (lb)
Long tube	1	19	0.042
Short tube	1	9	0.020
Single hex ball	1	13	0.029
Unlocked clevis and # 8 screw and washers	1	22	0.049
Unlocked pin and nut	1	6	0.013
Unlocked tang and two jam nuts	1	17	0.037
Locked tang and two jam nuts	1	15	0.033
Locked pin and nut	1	9	0.020
Locked clevis and #8 screw and washers	1	21	0.046
Combined Components			
Short unlocked-locked strut	1	99	0.218
Short locked-locked strut	1	99	0.218
Long unlocked-locked strut	1	109	0.240
Long locked-locked strut	1	109	0.240
All short unlocked-locked struts	4	396	0.873
All short locked-locked struts	16	1584	3.492
All long unlocked-locked struts	4	436	0.961
All long locked-locked struts	10	1090	2.403
All hex balls	16	208	0.459
Total Truss Mass		3714	8.188

3.3 Excitation System and Locking Mechanism

The JDX excitation system is used to displace the truss in preparation for a twang test. The excitation system consists of four linear actuators, connected to four linkage systems. The linkage systems are each connected to an electromagnet with a maximum pulling force of 40 pounds. When a linear actuator is activated, the linkage system guides the electromagnet to a steel plate on the tip mass. The electromagnet is able to take hold of the plate, and the linear actuator reverses direction. This effectively displaces the truss in the desired direction. Figure 10 shows a linkage system for the bend one mode and the linear actuator that guides the electromagnet. The two linear actuators that are used to displace the truss in the bend one and bend two directions are located on the support box inside the truss (see Fig. 4). There are two linear actuators used to excite the torsional mode of the truss. These two actuators and their respective linkages and electromagnets are mounted to the support posts that surround the truss (see Fig. 2). In order to excite the torsional mode the linear actuators must be run in unison. This provides a true twisting displacement motion, since both electromagnets displace the tip mass arms the same distance at the same time.

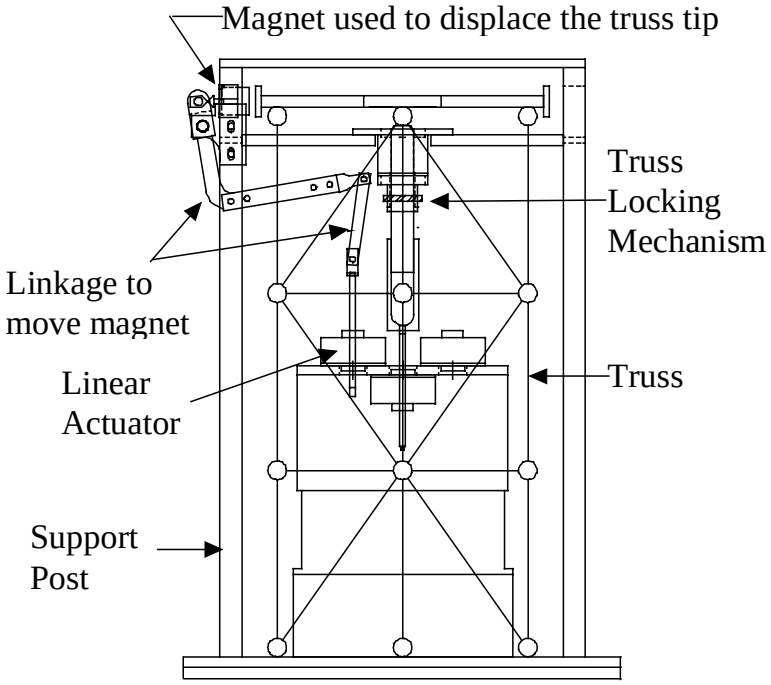

Fig. 10. Illustration of the Bend 1 mode excitation system and the truss locking mechanism.

Figure 10 illustrates the locking mechanism for the truss. Since the JDX experiment is to be flown on the space shuttle it was desired that the truss be kept from moving during the highly dynamic launch process. This minimizes the potential for joint wear and/or changes in alignment during launch. The primary mechanism for locking the truss is a 1.0-inch outer diameter, 0.5-inch inner diameter, stainless steel pin. The pin is moved upward into a locking sleeve attached to the bottom of the tip mass by a linear actuator. The original locker pin was made from solid aluminum and had a hardened steel dowel pin inserted perpendicular to its long axis to prevent torsional movements. During random vibration testing it was determined that the aluminum was not hard enough to withstand the impacts caused by the vibrating tip mass. At this time it was also found that the dowel pin made it difficult to lock the truss since it often was misaligned with the slot it was supposed to fit in. This caused the locker to jam only half way into the locked

position. For these reasons a new stainless steel locker pin was made with no torsion pin. A secondary method of truss restraint are four set screws attached to the outer support posts. These set screws limit the truss movement in the two bend directions. The set screws are only a backup measure to limit the possible motion of the truss tip mass.

3.4 Experiment Controller, Data Acquisition, and Power

During space flight the JDX experiment is controlled by a Campbell Scientific CR10 controller. This controller is responsible for moving the linear actuators, turning magnets on and off, triggering the data acquisition system, and monitoring experiment temperature. The CR10 controls the motors and magnets by switching on and off 32 switches on two Campbell Scientific SMD CD16's that are interfaced to the CR10. When the space shuttle reaches an altitude of about 100,000 feet, a baro-switch closes, powering up the CR10. At this point the CR10 logs time and temperature at various points in the experiment until about 8 hours into the flight when an astronaut toggles another switch. When this switch, designated Relay B, is closed, it signals the CR10 that testing is to begin. The CR10 immediately unlocks the truss then waits 4 hours. At this time the astronauts are in a sleep period. During the sleep period there are minimum thruster firings, and the chance of ruining tests as a result is minimized. The CR10 then executes 30 twang tests. Each mode, bend one, bend two, and torsion, is excited ten times. During each test the CR10 logs the time, temperatures, and battery voltages. When the testing is complete, the CR10 locks the truss and continues to log temperatures until the CR10 memory is full. Temperatures were logged for roughly one week.

There were several contingencies built into the CR10 program to provide for scenarios less perfect than the one just described. If the astronauts fail to toggle Relay B, the experiment will begin testing on its own near the beginning of the first sleep period. If an emergency landing must be made, the astronauts can toggle Relay B a second time. When this occurs the CR10 suspends testing and locks the truss. If the battery box temperature drops to an unacceptable level before Relay B is toggled, the CR10 will unlock the truss and begin testing in an attempt to get data before battery power is lost.

Six Kistler K-Beam capacitive accelerometers (model 8302A10) are used to measure the accelerations of the truss during twang testing. Three accelerometers are mounted to the tip mass and three are mounted to the base plate. Two of the tip mass accelerometers are mounted in the bend one and bend two directions, while the third is mounted to one of the unused torsion arms. The locations of these accelerometers are illustrated in Fig. 9. Two of the base plate accelerometers are also oriented in the bend one and bend two directions, while the third is mounted in the Z direction, which is the direction of the long axis of the truss. The base plate accelerometers are used to measure input vibrations from external sources. All six accelerometers measure accelerations in the range of 10.0 g's. Originally, K-Beam accelerometers with a range of 2.0 g's were used to measure vibrations. These accelerometers had better resolution but had to be replaced because they were very fragile and might not survive the high vibration environment

of space launch.

The accelerometer signals were recorded by a Campbell Scientific CR9000 data logger. The CR9000 was programmed to sample each of the six accelerometers at a rate of 3000 samples per second for a period of 1.5 seconds. The CR9000 included a two- megabyte EEPROM memory card with sufficient storage space to record 30 tests, as well as the program and operating system. Because of its high power draw, the CR9000 is powered down between tests. Figure 11 shows a photograph of JDX which indicates the locations of the CR10, CR9000, and the accelerometer signal conditioners.

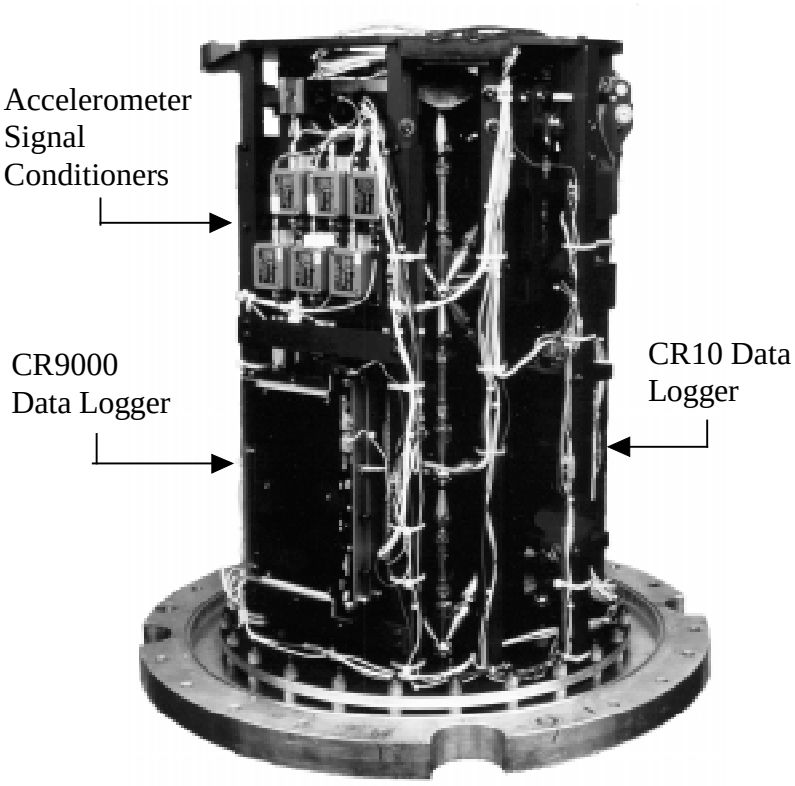

Fig. 11. Photograph of JDX showing the locations of the CR10 and CR9000 data loggers and the accelerometer signal conditioners.

The experiment power is provided by two 12-volt battery packs. One battery pack consists of 12 Gates D-cell sealed lead-acid batteries connected in two strings to form two parallel 12-volt voltage sources. The other pack contains 12 Gates X-cell sealed lead-acid batteries similarly connected. Both battery packs are rechargeable 200 to 2000 times depending on the depth of discharge used. The D-cells provide power for the CR10, CR9000, and accelerometers. The X-cells provide power for the linear actuators and electromagnets. The linear actuators and electromagnets require more power, so it was necessary to use the X cells to power them since they have twice the amp-hour rating of the D cells. To protect the battery circuits the battery packs are fused with 5-amp fast blow fuses. However, these fuses are located inside the battery box and are difficult to change once the box is in place. Therefore, a 3-amp fast blow fuse was added externally to each battery pack circuit. Appendix B shows a top-level circuit diagram for the experiment.

3.5 Truss Assembly

Assembling the Flight Model truss is a long and arduous process. The truss had to be assembled with enough precision to eliminate preloads in the joints. This is very difficult, and is more of an art than a science. Figure 12 shows the assembly jig that was used to aid in the truss assembly. The assembly jig provides exact location of the hubs with respect to each other, while also supporting the weight of the truss. Once the hubs are attached, the struts are placed between them starting at the top. The strut length must be adjusted by turning the tube past the preload free position and bringing it back to that position by tightening the jam nuts. This is a difficult procedure but becomes easier with experience. When the truss is completely assembled, the jig is removed and the excitation system is placed around it. At this point it is difficult to remove the entire excitation system in order to adjust the truss, so any further modifications must be done in place.

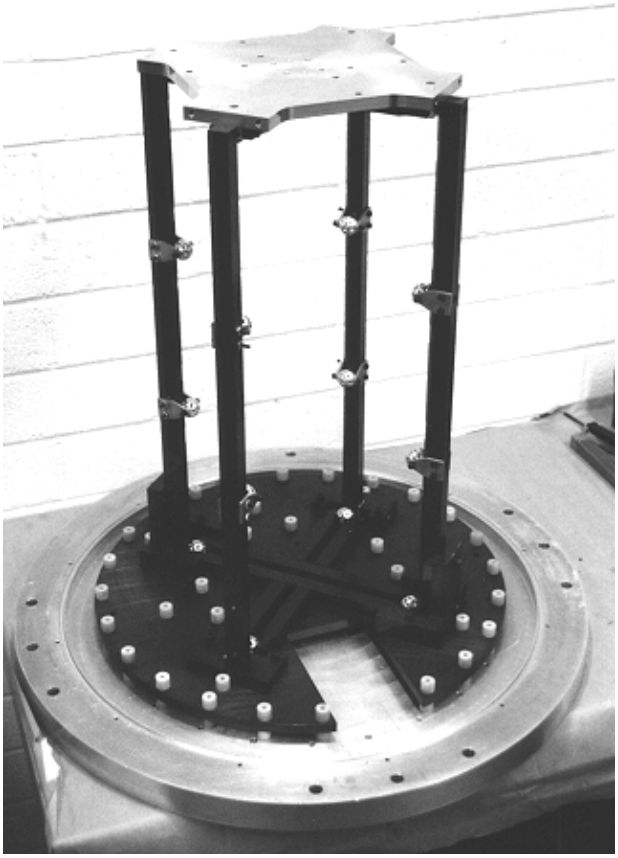

Fig. 12. Photograph of the truss assembly jig.

4.0 GROUND TESTING

Before ground testing of the Flight Model truss could begin, an appropriate site to conduct the tests needed to be selected. The ground testing of the Engineering Model truss was performed in the basement of the Petersen Engineering Building at Utah State University. However, this location proved inconvenient and it was hoped that the Flight Model tests could be taken on the second floor of the Petersen Engineering Building. A large steel plate weighing approximately 650 pounds was bolted to the floor to provide a rigid and massive attach point. When the experiment was mounted to the steel plate and twang tests were conducted, it was found that the vibrations damped much more quickly than was expected. Upon further study it was determined that the floor did not provide an adequately stiff mount for the experiment, and subsequent testing would have to take place in the basement. This illustrated the extreme sensitivity of the experiment to its mounting conditions and provided insight into problems that would occur in the low-G aircraft and space shuttle testing.

4.1 Ground Testing Setup

To perform ground tests on the Flight Model truss the experiment was bolted into an aluminum canister. The canister, shown in Fig. 13, has dimensions that are similar to an actual GAS can, and was used to simulate the test setup of a GAS can. Like the actual GAS can, the aluminum canister provided the experiment with added stiffness by allowing the lateral support pad illustrated in Fig. 3 to be engaged against the canister wall. The excitation system depends on the lateral support pads and the canister to hold the excitation framework in a fixed position as the truss is deflected.

Fig. 13. Photograph of JDX mounted to the floor for ground tests.

A problem involving the lateral supports and locker mechanism was discovered when it was observed that the locker mechanism often failed to lock the truss after the lateral support pads were engaged. When the lateral supports were engaged, they tended to displace the outer excitation framework relative to the tip mass. This would cause misalignment between the locker and the locker sleeve attached to the tip mass. In order to prevent this, movements in the excitation framework relative to the tip mass were monitored as the support pads were seated against the canister wall. To do this, hardware was temporarily attached to the experiment. A bracket with two perpendicular plates was clamped to the tip mass. Next, two dial micrometers were clamped to the top plate with the sensor

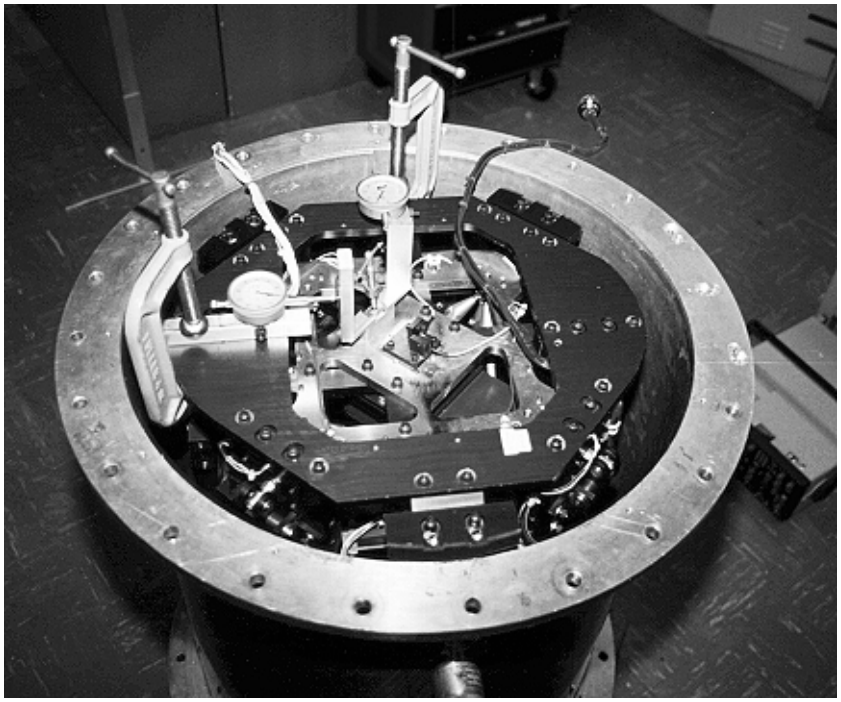

Fig. 14. Photograph showing how movements in the framework were monitered while the lateral support pads were tightened

arms in contact with the perpendicular bracket plates. This setup is shown in Fig. 14. The micrometers were zeroed and the lateral supports were engaged. When the final support was in place, the lateral supports were tightened and loosened until the micrometers indicated that the excitation framework was once again in the zero position. The micrometers and bracket were then removed and the canister was ready to be placed in its testing orientation.

Ground tests were taken with three orientations with respect to the gravity vector. The first orientation placed the long axis of the truss parallel to the gravity vector and is called the 0° orientation. The second orientation occurs when the long axis of the truss is placed perpendicular to the gravity vector. This is called the 90° orientation. The final orientation in which ground tests were taken is the 180° orientation. This orientation is similar to the 0° orientation; however, the truss is turned upside down so that the tip mass puts the struts in tension rather than compression. Figure 15 illustrates these three positions.

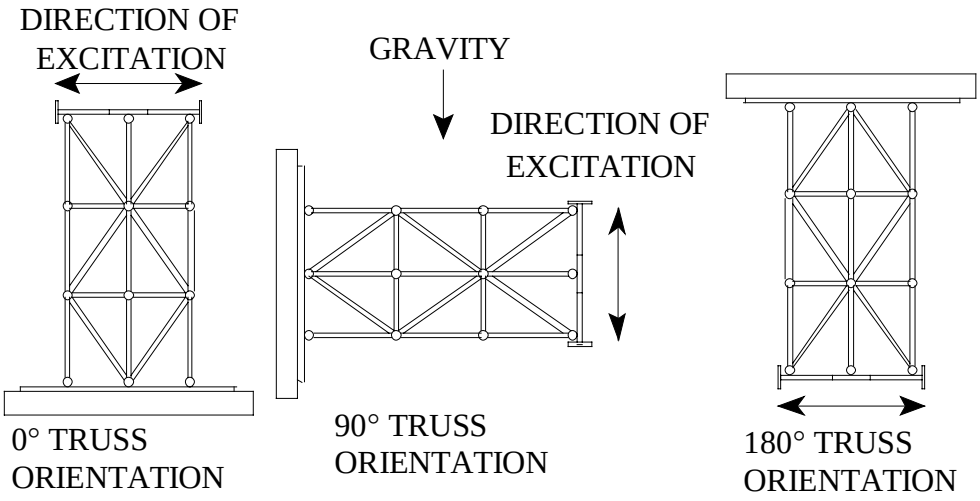

Fig. 15. Illustrations of the truss orientations used for ground tests.

When the tests were taken in the 0° orientation, the canister end plate was securely fastened to three steel plates that were bolted together in 40 locations. Each of the steel plates was 0.375 inches thick, 35 inches in diameter, and weighed 102 pounds. The canister was attached to these plates in three places and had a set of spherical washers at each point. This alleviated any warping that might otherwise occur if the canister was mounted flush to these plates. Warping was a serious concern since any warping in the canister end plate was found to cause preloads in the joints, thus seriously changing the twang test results. The three steel plates were fastened to an aluminum plate that bolted securely to the floor. This test setup is seen in Fig. 13. When the truss is in the 0° orientation, preloads due to gravity are minimized.

When 90° tests were taken, the canister had a bracket attached to the side, which allowed the experiment to be turned on its side and mounted to the steel plates. However, this test setup had

to be altered since it was discovered that the mounting bracket was not sufficiently rigid and the truss was exchanging energy with vibration modes of the canister and the mounting bracket. These motions were easily identified by examining the output of the accelerometers attached to the base plate of the experiment. This energy exchange caused the low amplitude signals to grow and die instead of steadily decaying. Several attempts were made either to stiffen the mount or make it more massive. The final mounting configuration stiffened the mount and made it more massive. Two pieces of angle iron were bolted between the canister end plate and the basement floor to provide greater stiffness. In addition, three steel bars, weighing approximately 200 pounds each, were bolted to the canister end plate. A photograph of this configuration is seen in Fig. 16. When the truss is placed in the 90° orientation, preloads due to the gravity vector are maximized.

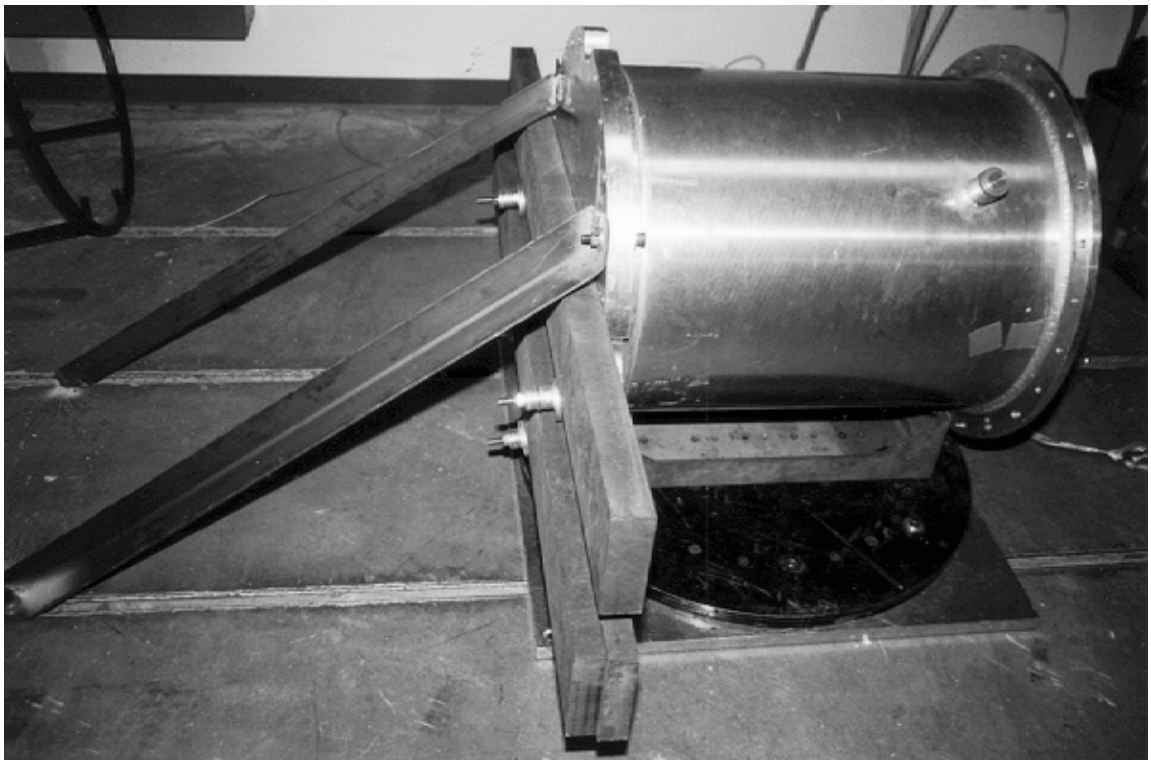

Fig. 16. Photograph of the 90° truss orientation test setup.

The 180° testing orientation required that the top of the canister be bolted to the aluminum plate which is attached to the floor. Three spherical washers were placed between the top of the canister and the aluminum plate. Again, initial tests showed that the mount was not sufficiently rigid and vibration modes of the canister system would couple with the bending modes of the truss. The three round, steel plates were bolted to the base plate of the test canister (note, in the 180° orientation, the base plate is on top). To further increase the mass attached to the baseplate, several large pieces of steel were also bolted to the top. Several steel cables were also attached between the basement floor and the top of the can in an attempt to stiffen the mount. The

addition of this steel and cables reduced coupling enough to get meaningful data from this configuration. This test setup is seen in Fig. 17.

Fig. 17. Photograph of the 180° truss orientation test setup.

4.2 Joint Gap Sizes and Pin Selection

The first twang tests performed on the Flight Model truss were done to determine the size of the diametrical gaps desired for each joint. Joint gap refers to the between the pin and holes in the clevis and tang assembly. By using small diameter pins, the joint gap is increased. In order to determine what size shoulder bolts to use as the clevis pins, three sets of shoulder bolts were found. These three sets were designated pin sets "one," "two," and "three." Pin set one had the largest diameters and pin set three the smallest. The holes in the clevis and tang assembly were fabricated and assembled using the best tolerance control that was available given our budget constraints. It was hoped that by using an interference fit of only 0.001 inches between the holes and the stainless steel inserts, defects such as the holes being out of round and having unpredictable sizes would be minimized. This was only partially successful. After inserting many sleeves it became apparent that an out-of-round of 0.00005 inches would have to be accepted on about half the inserts. A similar standard was applied to the shoulder bolts. If a shoulder bolt had more than a 0.0001-inch taper or was more than 0.00005 inches out of round, it could not be used. This limited the supply of shoulder bolts that could be used since most did not meet these stringent specifications.

The final pin set selected for use in the Flight Model truss was chosen on the basis of the measured decay in twang tests performed with each pin set and twang tests done on a completely locked truss. The decays were dependent on the amount of gap in the joints. It was important to find a set of pins with a very small amount of gap that would still demonstrate damping, which was very dependent on gravity-induced preloads. Pin set one had diametrical gaps ranging from 0.00025 to 0.00055 inches. Pin set two had diametrical gaps ranging from 0.0005 to 0.0008 inches. Pin set three has diametrical gaps ranging from 0.0008 to 0.001 inches.

The first twang tests performed were done with all 68 joints locked. A graph of the accelerations recorded during a bend one mode test in the 0° truss orientation with all joints locked is shown in Fig. 18. The vibrational decay shown follows the typical exponential decay that is expected in such a system. The vibrations take roughly 6 seconds to damp out, and are indicative of a lightly damped system. These tests provide a reference point for pin size testing since the damping rates of various pin and gap sizes can be compared to this setup in which there is no gap present. The bend two mode tests results are very similar to the bend one mode and only the bend one mode tests are presented here. The torsional results are discussed separately in section 6.0 of this report. Decays from typical bend two and torsion mode tests are illustrated in Appendix C.

Figure 19 shows the measured decay for a twang test, using pin set one, in the bend one direction, with the truss in a 0° truss orientation. The damping is dramatically increased. However, after one full second there is still some vibration in the bend one direction. It was noted that some of the pins in pin set one could not be easily inserted into the joints. It is suspected that slight misalignments between the separate clevis and tang fitting effectively eliminated most of the joint gap. This might explain the low damping observed at small amplitudes.

The acceleration time history for a twang test, in the bend one mode direction, using pin set two is shown in Fig. 20. The signal is seen to damp out in roughly one second. Figure 21 illustrates the vibrational decay of a bend one mode twang test when pin set three was employed. The data show the vibrations are completely decayed around 0.6 seconds. Furthermore, the damping at low amplitudes was much greater than the previous two pin sets. This is thought to occur primarily because at low amplitudes the gravity-induced preloads prevent the joint from traversing the deadband region when the gaps are small. Thus, a major component of joint damping was absent at lower amplitudes. Pin set two was selected for additional testing since it provided a good compromise between keeping pin gaps small and yet still having a significant increase in damping due to the joints.

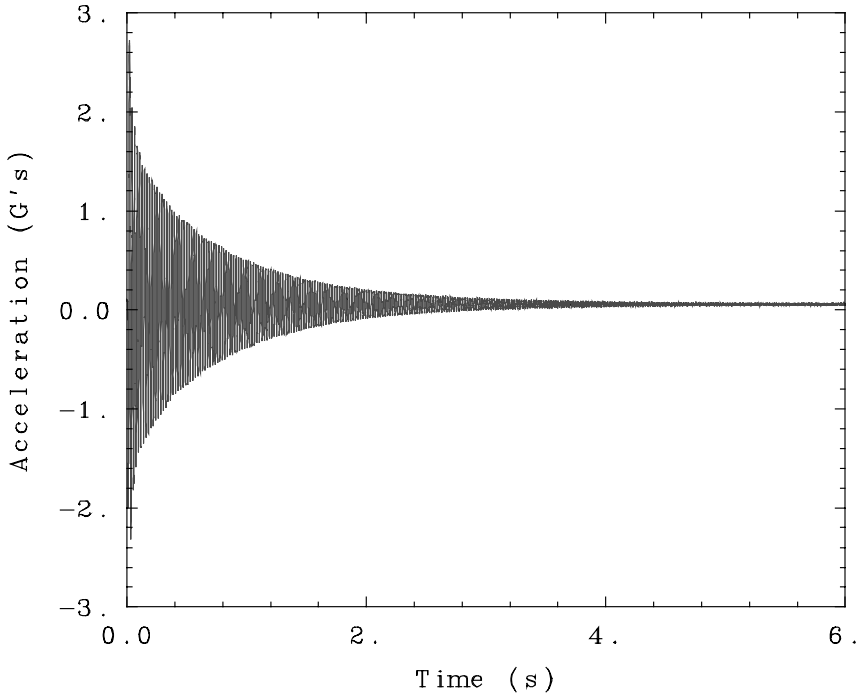

Fig. 18. Bend 1 mode twang test will all joints locked, 0° truss orientation.

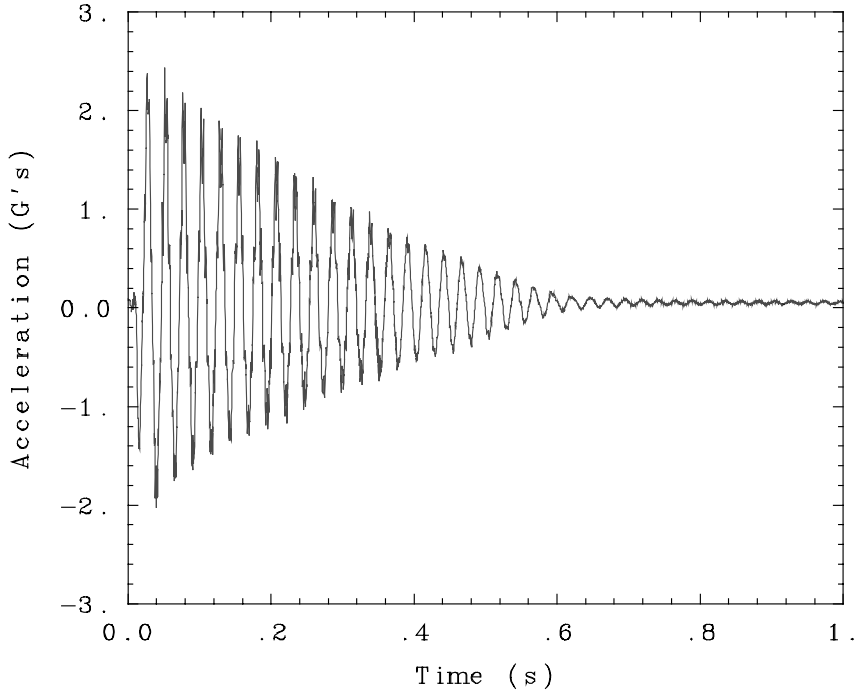

Fig. 19. Bend 1 mode twang test with pin set 1, 0° truss orientation.

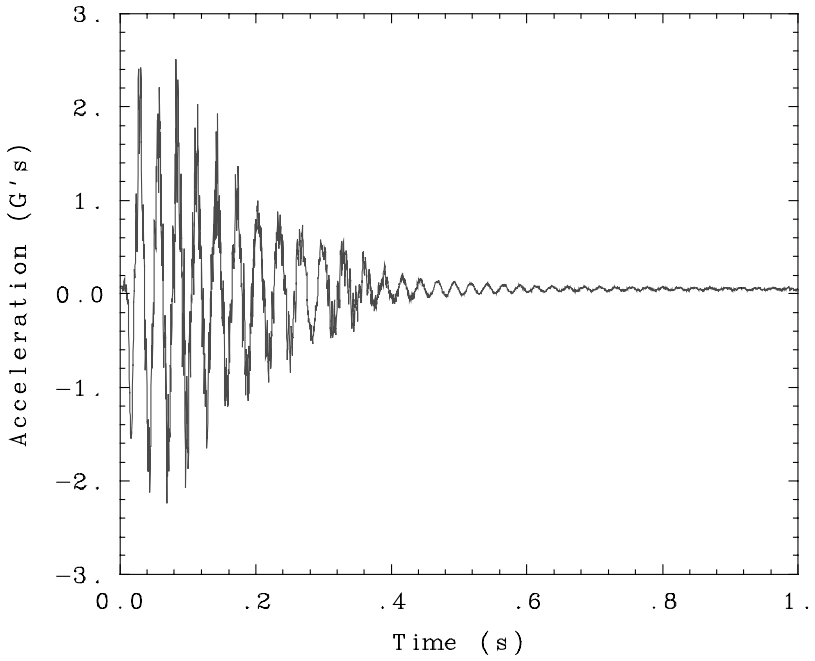

Fig. 20. Bend 1 mode twang test with pin set 2, 0° truss orientation.

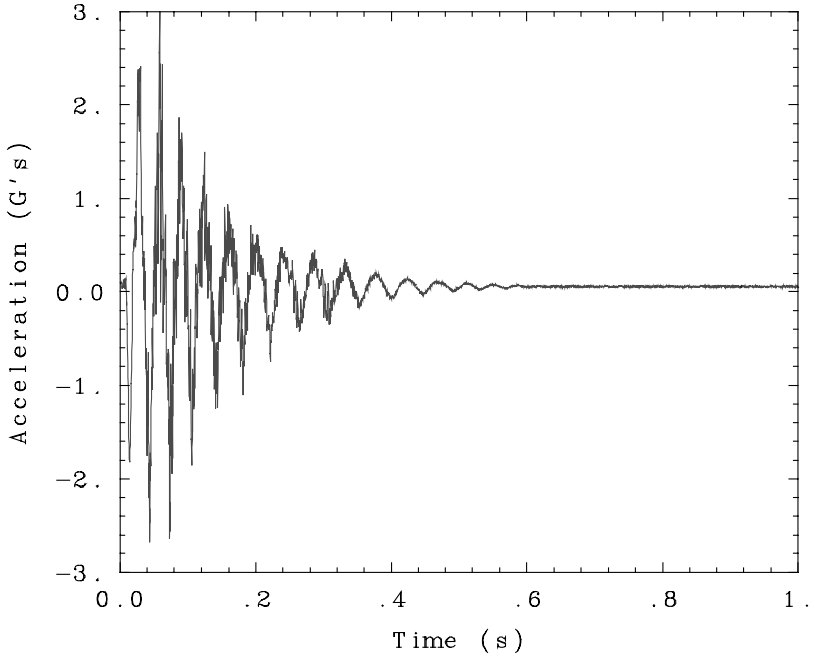

Fig. 21. Bend 1 mode twang test with pin set 3, 0° truss orientation.

Further testing showed some of the gaps were either too large or too small so new pins were tried in these joints. The pin sizes, clevis hole sizes, tang hole sizes, and gap sizes for the truss are listed in Table 3. It should be noted that the first number listed under the heading Pin Number represents the joint the pin was intended for, and the second number represents the pin set it came from. Therefore, the 4-1 listed for joint number one means the pin was originally intended to be placed in joint four, and belongs in pin set one. This had to be done since the desired gap could not be achieved by pins intended for joint one, and the supply of pins that met the taper and out-of-round specifications was quite small.

Table 3. JDX Flight Model truss final pin set, clevis, and tang sizes

Joint Number	First Clevis Diameter	Second Clevis Diameter	Tang Diameter	Pin Number	Pin Diameter	Diametric Gap
1	0.18715	0.18725	0.18705	4-1	0.18660	0.00045
2	0.18725	0.18720	0.18720	2-3	0.18660	0.00060
3	0.18730	0.18720	0.18725	3-1	0.18665	0.00055
4	0.18715	0.18705	0.18720	4-2	0.18640	0.00065
5	0.18720	0.18715	0.18715	5-2	0.18670	0.00045
6	0.18720	0.18715	0.18725	6-2	0.18640	0.00075
7	0.18720	0.18730	0.18725	7-1	0.18645	0.00075
8	0.18725	0.18720	0.18720	8-2	0.18635	0.0008

Figure 22 shows the locations of all eight unlocked joints. It is seen that the odd- numbered joints correspond to the primary struts, while the even-numbered struts correspond to the cross struts.

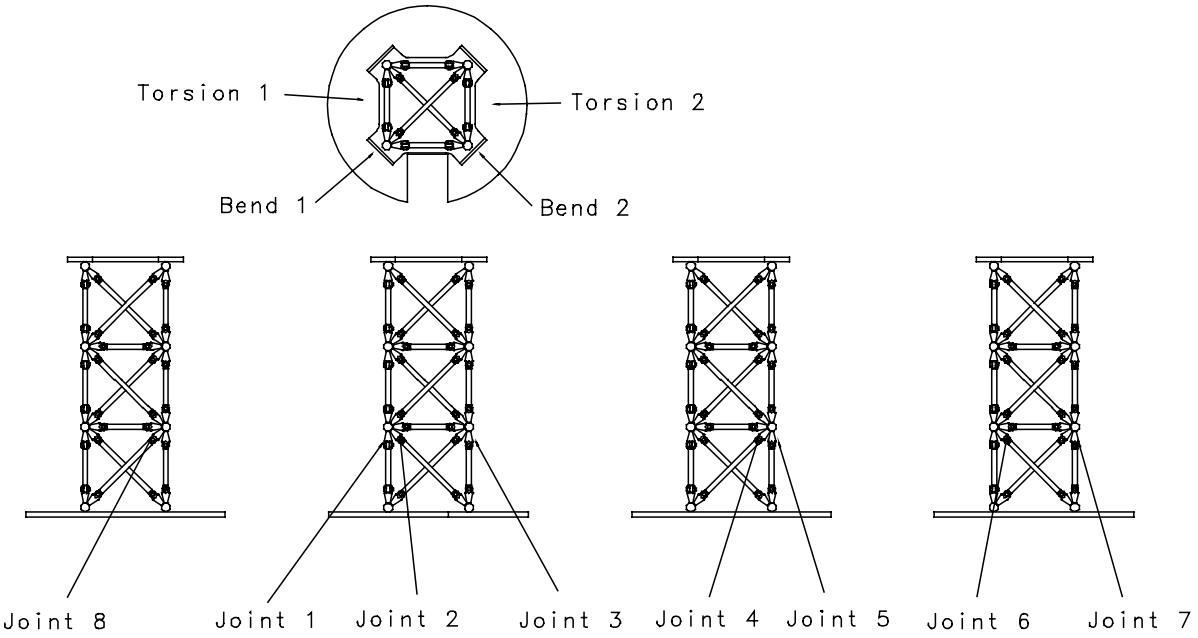

Fig. 22. Illustration of the pinned joint locations and identification numbers.

While general damping information can be inferred by simple inspection of the decay of various twang tests, it was desired to examine how the damping varied with oscillation amplitude. This was done through the use of a FORTRAN computer code that calculated the logarithmic decrement of the various signals. The logarithmic decrement is a measure of damping in a single-degree-of-freedom system. The logarithmic decrement relates the decay of a vibration's peak amplitudes to damping and is given by Eq. 1.

$$\delta = \frac{1}{n}\ln\left(\frac{A_o}{A_n}\right) \qquad \textbf{Eq. 1}$$

where: δ = logarithmic decrement
n = number of cycles
A_o = initial peak amplitude
A_n = peak amplitude after n cycles

The logarithmic decrement was computed over each cycle (n = 1) of the twang tests. The two amplitudes used to compute the logarithmic decrement are averaged and plotted against the logarithmic decrement to show how the damping varies with amplitude. The average amplitudes are slightly lower than the twang test acceleration amplitudes since the data was smoothed before logarithmic decrements were computed. The decays were smoothed to remove the high frequency hash, which is seen in Figs. 19, 20, and 21. With the hash removed the computer program could easily determine the peak amplitudes appropriate for each oscillation. Smoothing was found to have no measurable effect on the logarithmic decrement calculations since all the peaks are smoothed uniformly. The smoothing did reduce average amplitudes by approximately 10%.

The twang tests of the JDX truss can be treated as basically single degree of freedom system if only one mode of the truss is excited. This is not to say that no torsional or bend two mode excitation occurs during a bend one test, for example. However, the excitation of other modes is small enough that a single-degree-of-freedom measurement of damping such as the logarithmic decrement yields meaningful damping data. An illustration of the relative amplitudes of the bend one and bend two modes during a bend one mode test can be found in Appendix C. Figure 23 is a chart of the logarithmic decrement values for the various pin sets plotted versus the average amplitude. The data points shown are strictly for identification of the various curves and were generated by curve fitting the measured data. Complete curve fit equations for all logarithmic decrement curves can be found in Appendix D. The data points shown in the plots in Appendix D are the logarithmic decrement values computed from 10 twang tests. The scatter in the measured data can be seen in these plots. The logarithmic decrements of the various pin sets clearly indicate that as the amount of deadband in the joints increases, so does the damping.

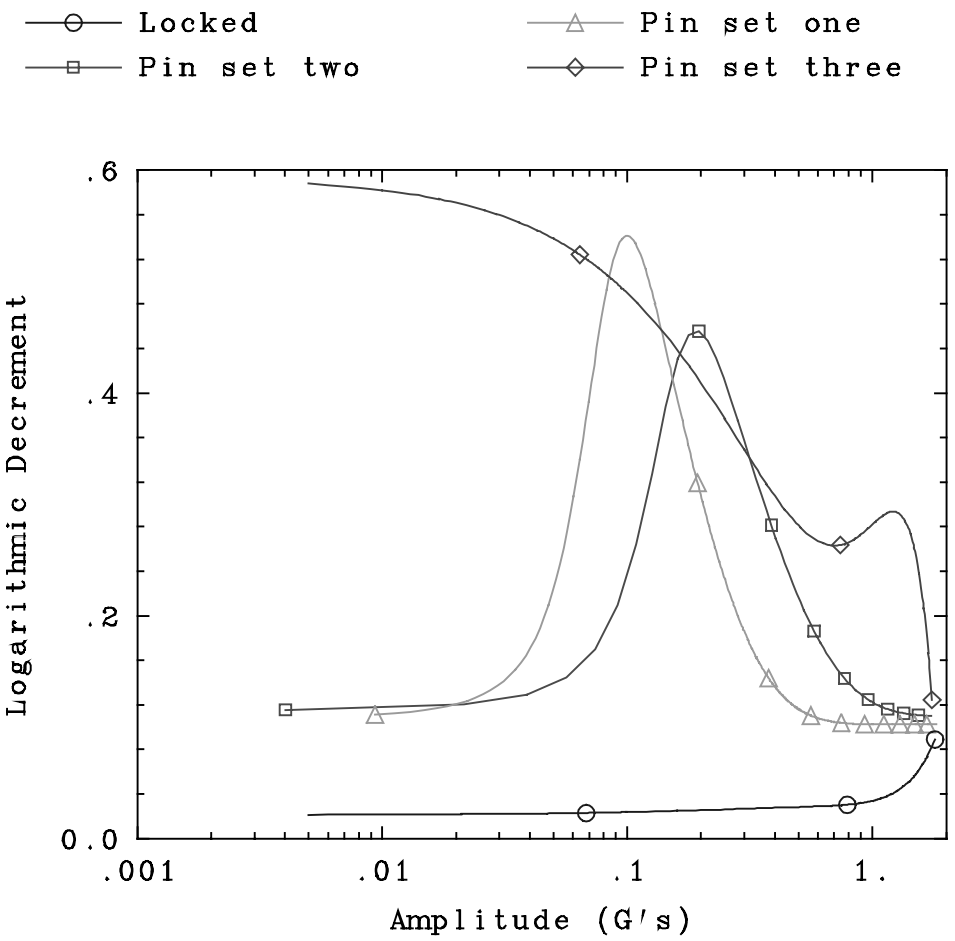

Fig. 23. Logarithmic decrement data from the three pins sets and for a locked truss.

4.3 Baseline Testing

After the final pin set had been chosen, baseline twang tests were taken to record the dynamic characteristics of the Flight Model truss. The baseline tests were taken in all three truss orientations shown in Fig. 22. By comparing the twang tests in the various positions the influence of gravity on damping can be observed. Figure 24 illustrates the first 1.0 seconds of decay during a bend one mode twang test performed with all joints locked with a 0° truss orientation. The truss has low damping. Figure 25 illustrates a bend one mode twang test with eight unlocked joints in the 0° truss orientation. Comparing Fig. 24 and Fig. 25 demonstrates that the addition of the eight unlocked joints changes the dynamics of the truss considerably. The damping in the truss increases significantly, and the peaks of the acceleration are no longer smooth. The hash seen in the peaks of this twang test are suspected to be attributed to impacting in the joints. Impacting occurs when the joint moves completely through the dead band, causing the strut to go from tension to compression or vice versa. Impacting is suspected to be a major contributor to the damping in the Flight Model truss.

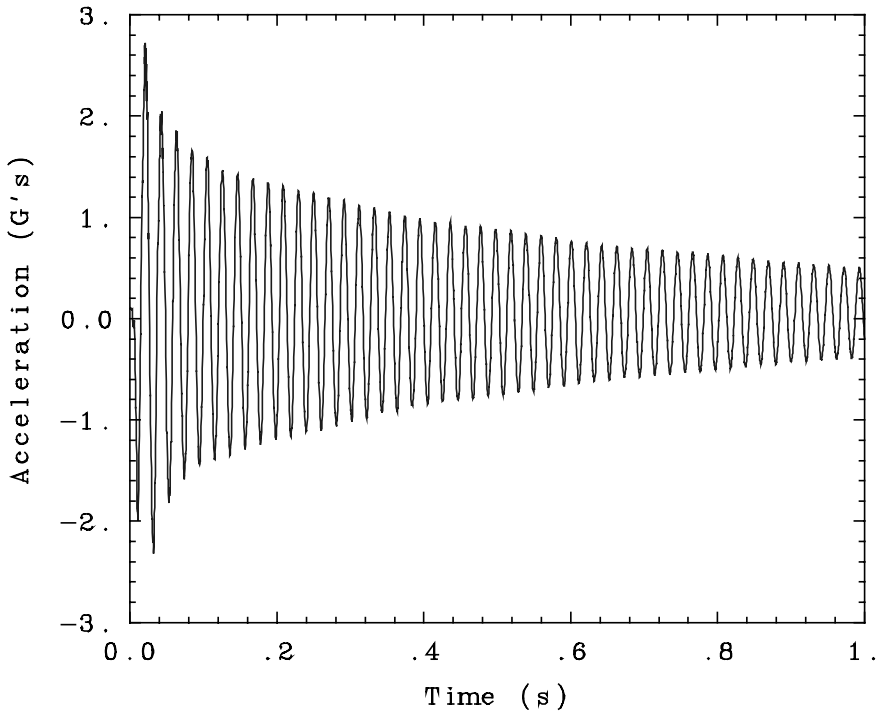

Fig. 24. Bend 1 mode twang test in the 0° truss orientation with all joints locked.

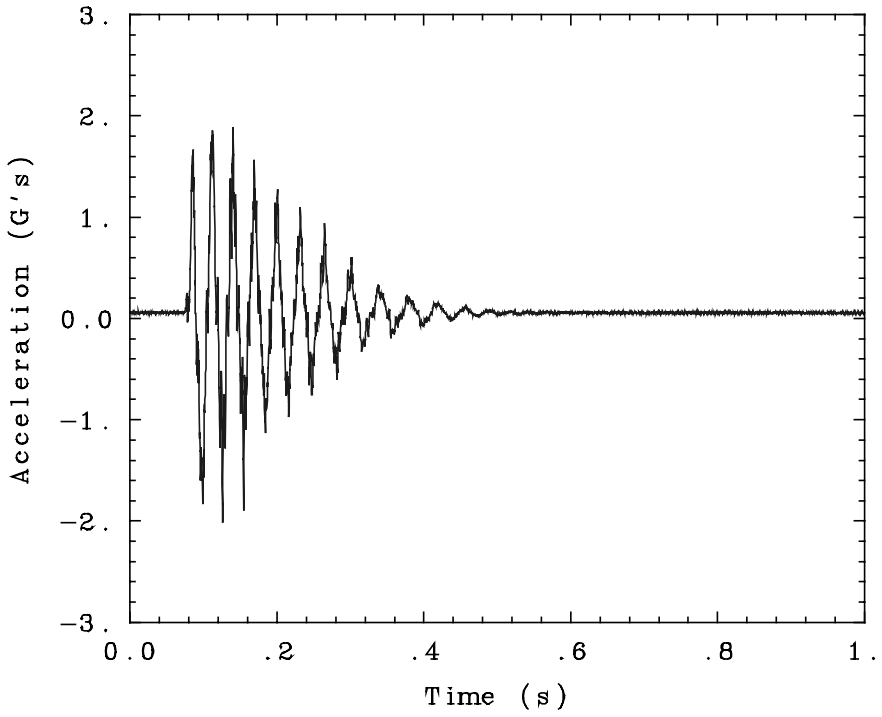

Fig. 25. Bend 1 mode baseline twang test in the 0° truss orientation.

When the truss is placed in the 90° orientation, the maximum effect of gravity preloads is seen. Figure 26 shows a bend one test taken in the 90° truss orientation. Note that the Kistler K-beam accelerometers used can sense constant or "DC" accelerations. Thus the equilibrium acceleration in Fig. 26 is approximately -1 g, since in the 90° truss orientation, gravity acts in the negative direction on this accelerometer. The initial decay of the 90° test has a damping rate similar to the decay of the 0° test. However, the initial oscillations are not symmetrical and appear truncated in the positive direction. The hash attributed to impacting is clearly seen. As the amplitude of the vibrations decreases, the behavior of the truss changes. Joint movement through the deadband can only occur when the truss moves upward far enough to release its weight off the joint. The initial oscillations appear truncated near the zero acceleration level, which should correspond to the deadband region for the joints. Thus as the acceleration amplitude of the tip mass drops below one G, the ability of the joint to move through the deadband will be inhibited. This is shown in Fig. 26 when the peaks begin to show less hash. When there is no movement through the joint deadband region, the damping decreases dramatically, and the acceleration data becomes closer to that of the locked truss than the unlocked truss.

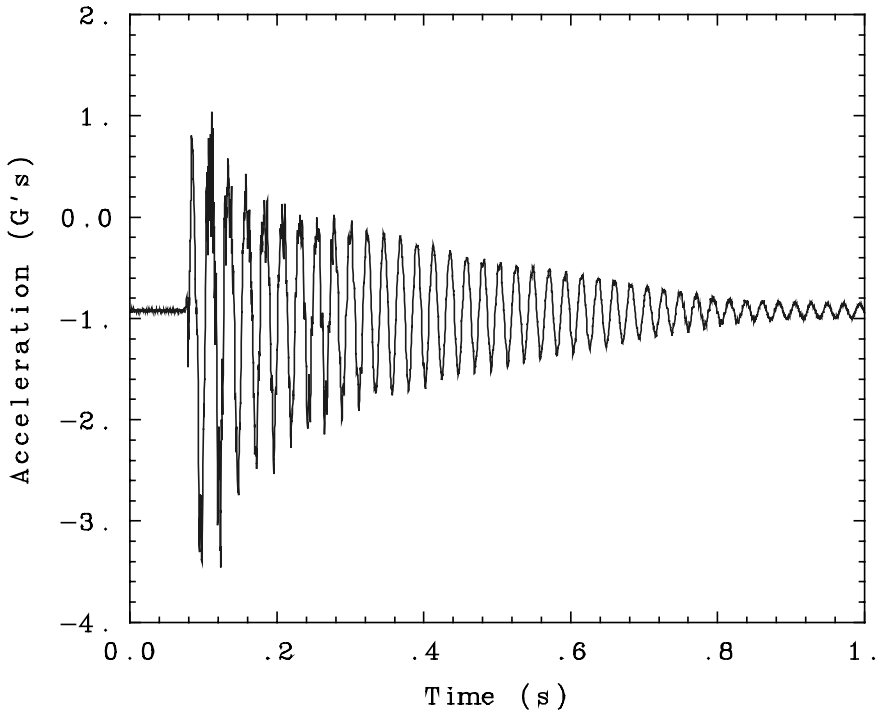

Fig. 26. Bend 1 mode baseline twang test in the 90° truss orientation.

When the twang tests are taken in the 180° orientation, it is reasonable to expect that the data would be very similar to data recorded in 0° tests. Figure 27 shows that this is indeed the case. The same characteristic hash of a lightly preloaded structure is evident and the decay time is similar.

The logarithmic decrement plots of the four above mentioned tests are shown in Fig. 28. It is important to note that there were two logarithmic decrement curves generated for the 90° orientation tests. This is because of the nonsymmetric nature of the acceleration time histories in the 90° orientation. Therefore, one logarithmic decrement curve is generated for the positive peaks and another is generated for the negative peaks. The curve plotted in Fig. 28 is the logarithmic decrement of the negative peaks. The similarities between the logarithmic decrement of the 90° orientation tests to the locked tests are obvious. The 180° and 0° orientation tests also have an obvious similarity. From these tests it is evident that the effect of gravity on the dynamic characteristics of the truss is significant, and the orientation of the truss with respect to the gravity vector is very important.

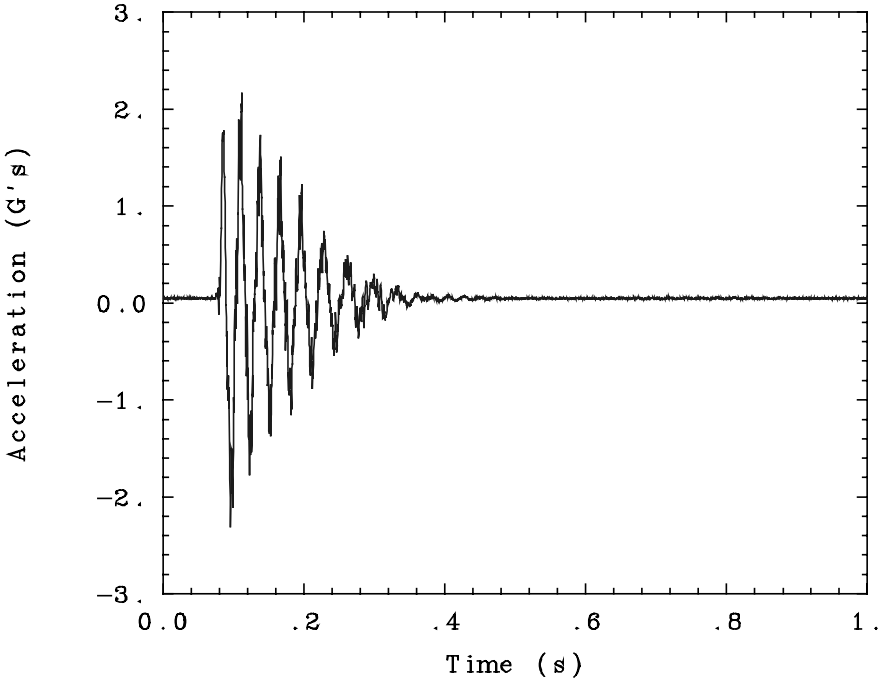

Fig. 27. Bend 1 mode baseline twang test in the 180° truss orientation.

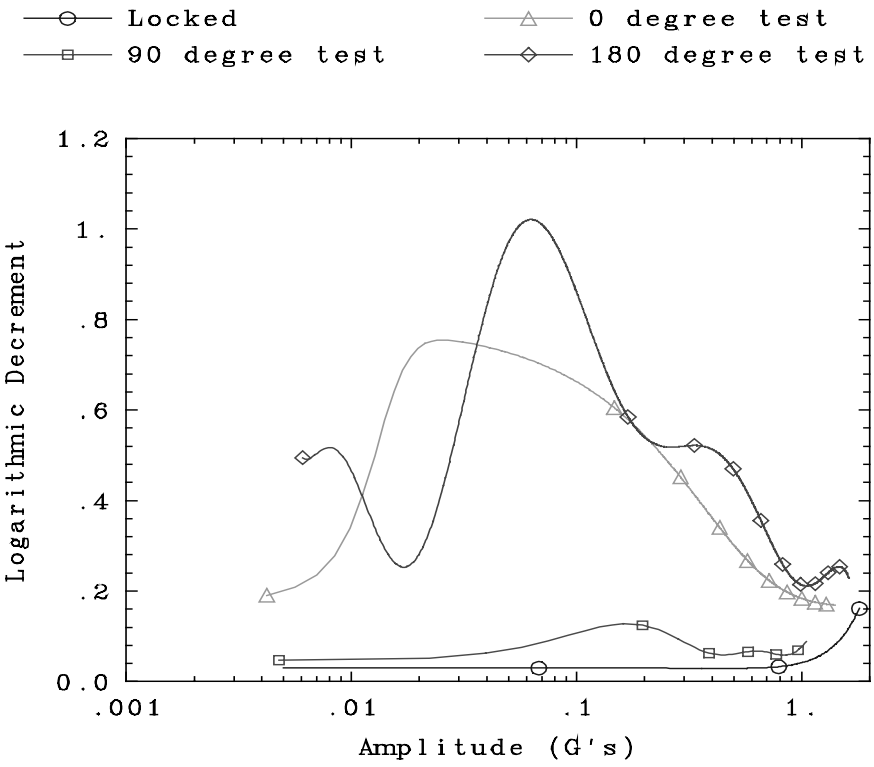

Fig. 28. Logarithmic decrement curves for the Bend 1 mode baseline tests.

4.4 Cold Cell Testing

The Space Shuttle flight on which JDX was scheduled to fly was designated a "cold" mission. This meant the space shuttle's cargo bay doors would be open and facing deep space for much of the mission. Accordingly, the performance of the experiment at low temperatures was a concern. In order to assure that the experiment would function correctly over a wide temperature range, tests were conducted in a thermal vacuum chamber. The thermal vacuum chamber or cold cell is located in the Space Dynamics Laboratory facilities in the Petersen Engineering Building. The tests were taken at 20° C, 10° C, 0° C, -10° C, and -20° C. The test setup for these tests is shown in Fig. 29.

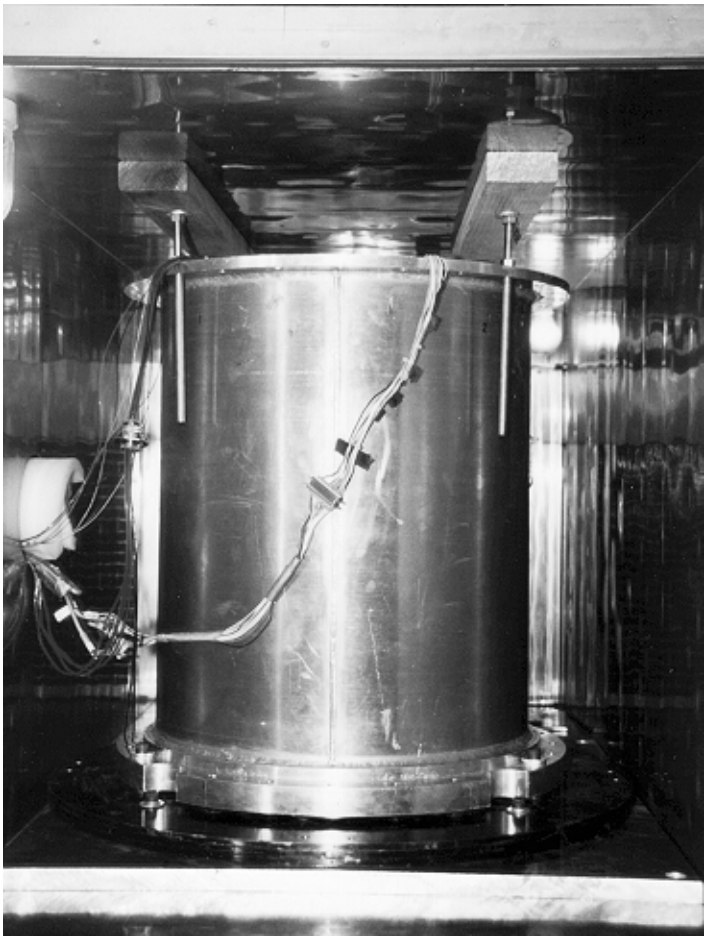

Fig. 29. Photograph of JDX inside the cold cell.

The experiment was placed in the experiment canister with the three round steel plates and aluminum plate bolted to the bottom of the canister. The cold cell did not have any mounting points that would allow the experiment to be bolted to the floor. Therefore, four thread rods were preloaded against two wooden blocks that pushed against the chamber ceiling in an attempt to provide a stiffer mount. When nuts were tightened on the thread rod, the experiment was forced solidly against the ceiling and floor. Even with the thread rods the mount was less than perfect and some coupling with the cold cell did occur. Testing was performed in only the 0° orientation because the purpose of these tests was to gain insight into the effects of temperature on the truss, not the effects of temperature and gravity on the truss. The battery packs that would be used on the space shuttle flight were used to power the experiment during these tests in order to insure they could provide the necessary power at the various temperatures.

It was found that the batteries could perform 90 twang tests before the voltage dropped to unacceptable levels. Only 30 tests would be performed during the space shuttle flight so this was deemed acceptable. However, one problem with the power system at low temperatures was brought to light by these tests. At temperatures lower than -20° C, the diodes that protect the

batteries suffered large voltage drops across them, causing malfunctions in the data logger and experiment controller. Therefore, it was important that the experiment only operate at temperatures above -20° C.

Another concern with low temperature operation was the locker mechanism. Because of aforementioned difficulties with the locker, there was concern that at lower temperatures the lubricants used would stiffen and would prevent its normal operation. For this reason the locker was tested numerous times, but no problems were detected.

The logarithmic decrement of bend one tests in the cold cell at the various temperatures is shown in Fig. 30. From this some important conclusions about the low temperature effects on the truss can be drawn. It is seen that all of the curves except the -20° C curve have the same basic shape and very similar amplitudes. This implies that temperature has very little effect on the dynamics of the Flight Model truss until it drops to about -20° C. The testing on the space shuttle was scheduled to begin during the first day of the mission so the temperature of the experiment was not expected to be lower than 0° C. From the data gathered during cold cell testing, no problems due to low temperatures were anticipated.

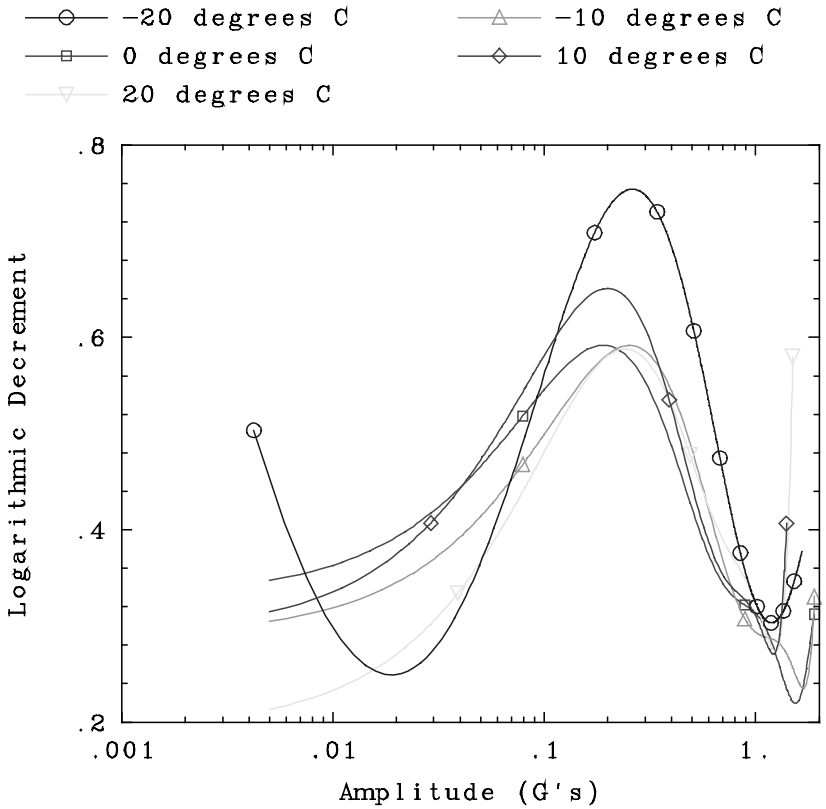

Fig. 30. Logarithmic decrement curves for the Bend 1 mode cold cell twang tests.

5.0 LOW-G AIRCRAFT TESTING

To simulate the microgravity environment of space, JDX was tested aboard NASA's KC-135 low-G aircraft. In theory this testing would allow data to be taken in a gravitational environment similar to the space shuttle cargo bay. The aircraft simulates microgravity by flying large parabolas which provide over 20 seconds of microgravity during each parabola. This was ample time to complete a twang test. However, it was not clear whether or not the experiment would be isolated sufficiently from input vibrations. To give the experiment the best chance of recording useful data, tests were taken in two different setups. In each of the setups, the experiment was placed in the testing canister with the three round, steel plates bolted to the bottom of the canister. A railing that completely surrounded the can was bolted to the steel plates to provide ease of handling during the microgravity tests.

In the first setup, illustrated in Fig. 31, the experiment is bolted to the floor of the aircraft. Because of the high sensitivity of the truss to vibration inputs from the base, this setup was not expected to be particularly successful.

Fig. 31. Photograph of JDX attached to the aircraft floor for testing.

The second setup available in the low-G aircraft is the free-float test. This is shown in Fig. 32. During a free-float test the experiment is not secured to any structure and is allowed to float in the microgravity environment. Based on previous tests of the Engineering Model truss on the aircraft, it was believed that this configuration would provide the greatest chance of generating useful data. The total mass of the test article was 554 pounds, which was the upper limit NASA personnel felt comfortable with. The steel plates attached to the base were designed to provide a stiff and massive base. A linear finite element model of the free float test predicted only an 8% shift in frequency of the two bending modes when compared with a fixed boundary condition. This indicates that this setup is close to a cantilevered boundary condition.

Fig. 32. Photograph of JDX during a free float test onboard the KC-135 aircraft.

The testing aboard the low-G aircraft for the Flight Model truss took place over four days from October 25 to October 28, 1994. During the first 2 days of the flight, testing was done in the first configuration. As anticipated, the data from these tests was unusable because of input vibrations from the aircraft and an insufficiently stiff mount. The third day of low-G testing was canceled because of rough air, leaving only one day to perform the free-float tests. On the fourth and final day of testing, successful free float tests were accomplished. Figure 33 illustrates a bend one test taken during free float. There are several significant factors to note in Fig. 33. First, the decay of the signal is faster than even the 0° orientation ground tests. Second, the hash that was observed in the unlocked truss decays is present at even the lowest amplitudes of the low-G test. This gives insight into the greater damping observed in the micro gravity environment. The hash in the peaks of the signal has previously been attributed to impacting in the joint. In the 0° truss orientation ground tests there were gravity-induced preloads in the truss. At sufficiently small amplitudes these preloads are large enough to prohibit the joint from moving through the deadband. However, the microgravity tests had no such preloads and impacting occurred during the entire decay. The only significant preloads that could have existed in the truss during these tests would be due to assembly. As previously mentioned, those preloads were minimized by a rigorous assembly process. The increase in damping is further illustrated in Fig. 34, which compares the logarithmic decrements of a bend one mode test in a 0° truss orientation with a low-G test. This clearly shows the damping in the truss is further increased in the microgravity environment.

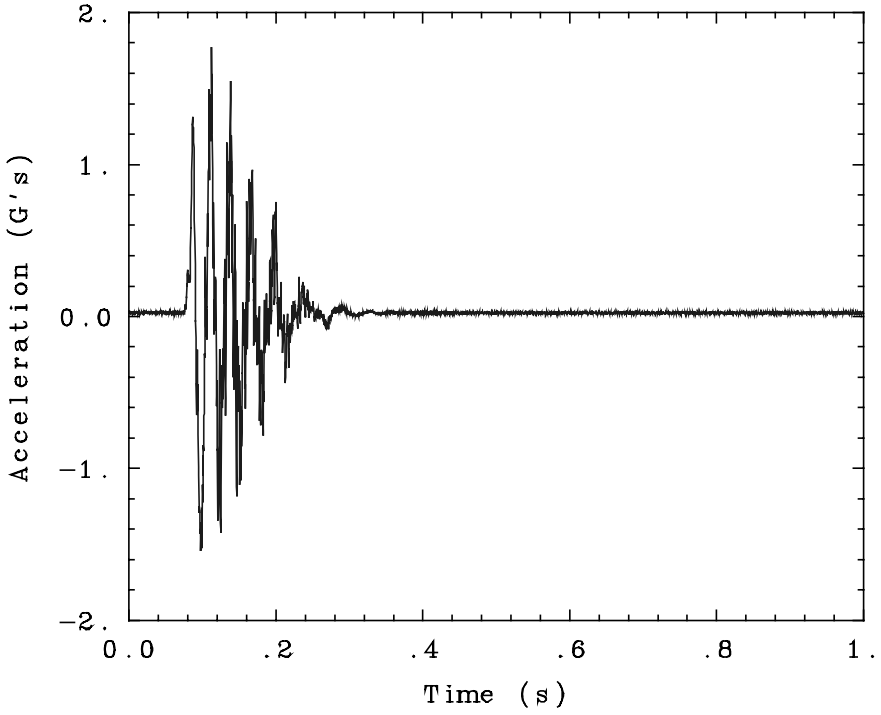

Fig. 33. Bend 1 mode free float twang test conducted aboard the low-G aircraft.

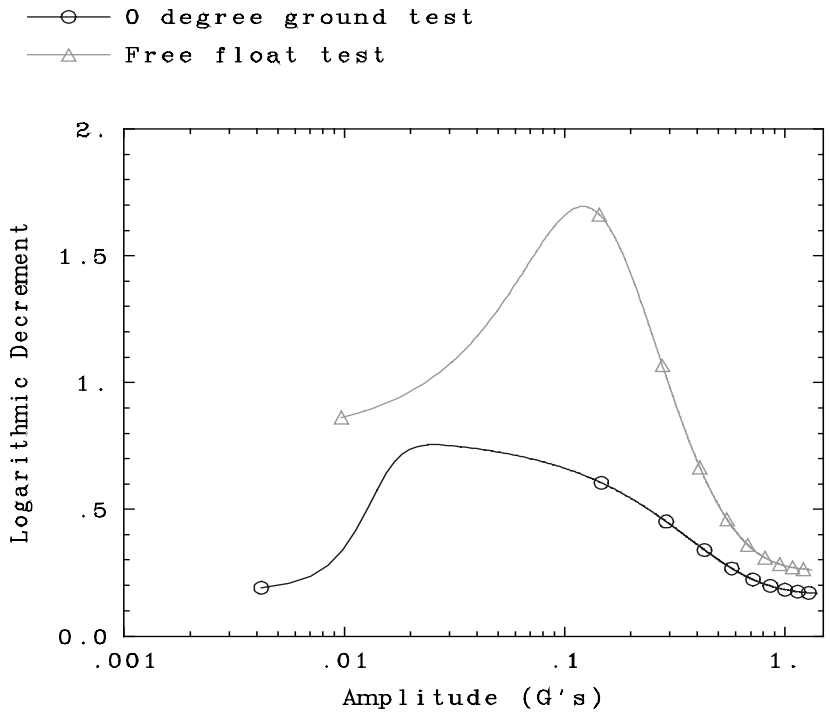

Fig. 34. Logarithmic decrement curves for the bend 1 mode low-G twang tests.

6.0 TORSION MODE GROUND AND LOW-G TEST RESULTS

Up to this point only the results from tests of the bend one mode of the truss have been used to draw conclusions. As previously mentioned, the bend two mode tests gave very similar results to the bend one mode. The bend two mode tests results are documented in Appendix C. However, the torsion mode in the truss has very different behavior when there is gap in the joints. A linear finite element model of the truss predicted a torsion mode occurring at approximately 118 Hz. When all 68 joints of the truss are locked, the torsion mode can be readily identified. Figure 35 shows a torsion mode test taken with all joints locked in the 0° orientation. When a Fast Fourier Transform (FFT) is done on this time history, as seen in Fig. 36, the two bending modes and the torsion mode can be seen. The bending modes are easily excited during a torsion mode test. The large spike at about 118 Hz is the observed torsion mode. However, when the eight unlocked joints are introduced the torsion mode disappears and is replaced by higher frequency modes. The decay of a torsion mode ground test taken in the 0° truss orientation with eight unlocked joints is illustrated in Fig. 37. Figure 38 shows the results of a FFT performed on this time history. The FFT shows very little sign of the expected torsion mode and instead shows a mode that occurs at approximately 800 Hz. Figure 39 is a FFT performed on a baseline torsion mode test taken in the 90° truss orientation. The torsion mode at 110 Hz is present along with bending modes at about 35 Hz. In the 90° truss orientation, the bending modes are strongly coupled to the torsion mode. Thus, one can not excite a torsion mode without exciting the two bending modes of the truss. This is cause by the truss being slightly deformed by the gravity load and the truss vibrates around this new equilibrium position. Thus, Fig. 39 shows that the bending and torsion modes have equivalent amplitudes. The response of the 800 Hz mode is small in this case. When a FFT is performed on a low-G torsion mode test, as seen in Fig. 40, the results are very similar to those seen in the baseline torsion mode test in the 0° orientation. Thus, the torsion mode disappears if joint loads are small. The torsion mode is only observed when the gravity induced preloads are large enough to prevent the joint from entering the deadband of the joint. The exact cause of this phenomena is not known but is under investigation.

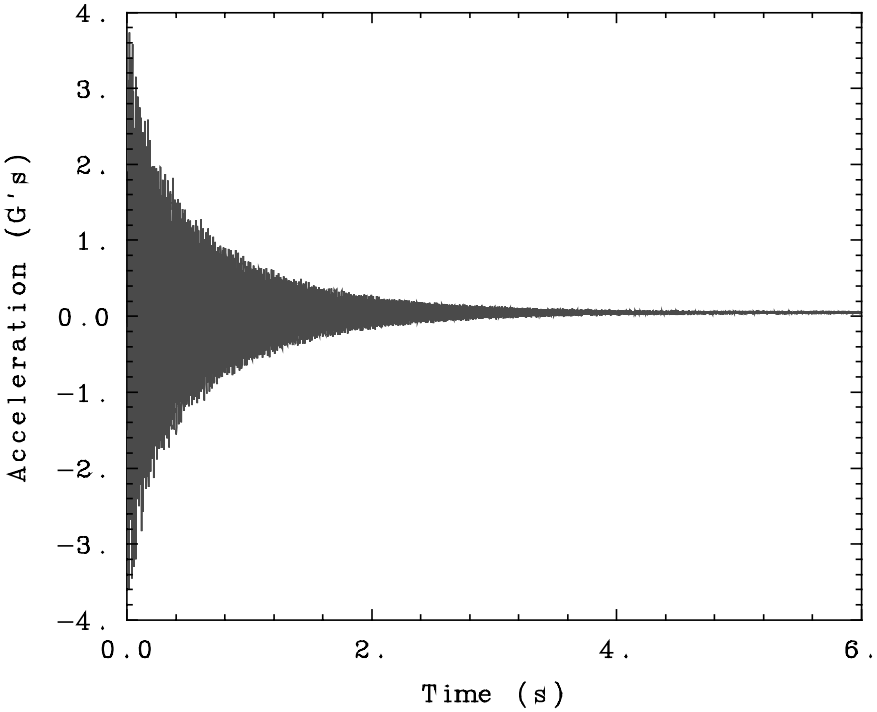

Fig. 35. Torsion mode twang test with all joints locked and a 0° truss orientation.

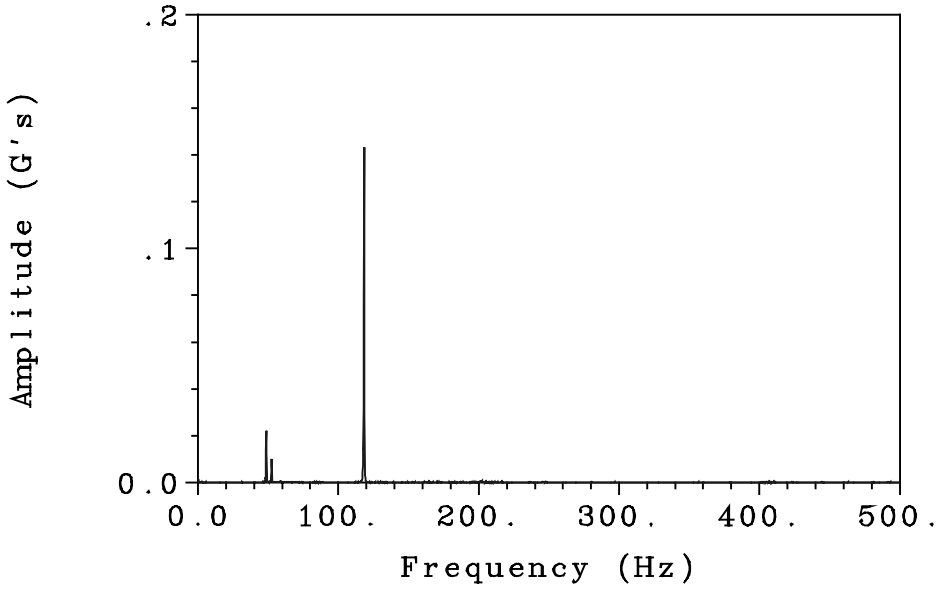

Fig. 36. FFT of a torsion mode twang test with all joints locked and a 0° truss orientation.

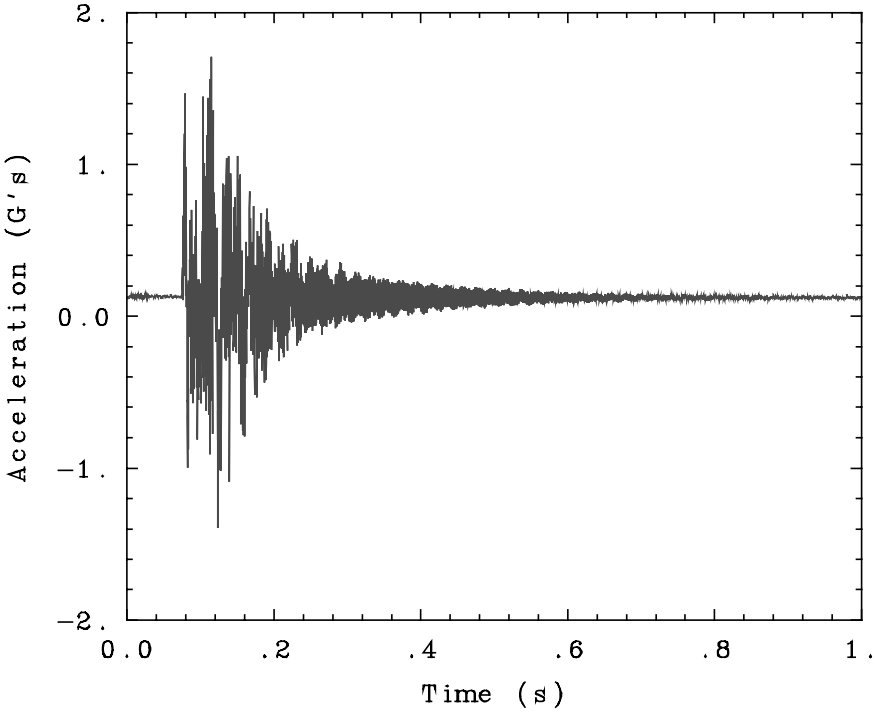

Fig. 37. Torsion mode twang test of the Flight Model truss in a 0° truss orientation.

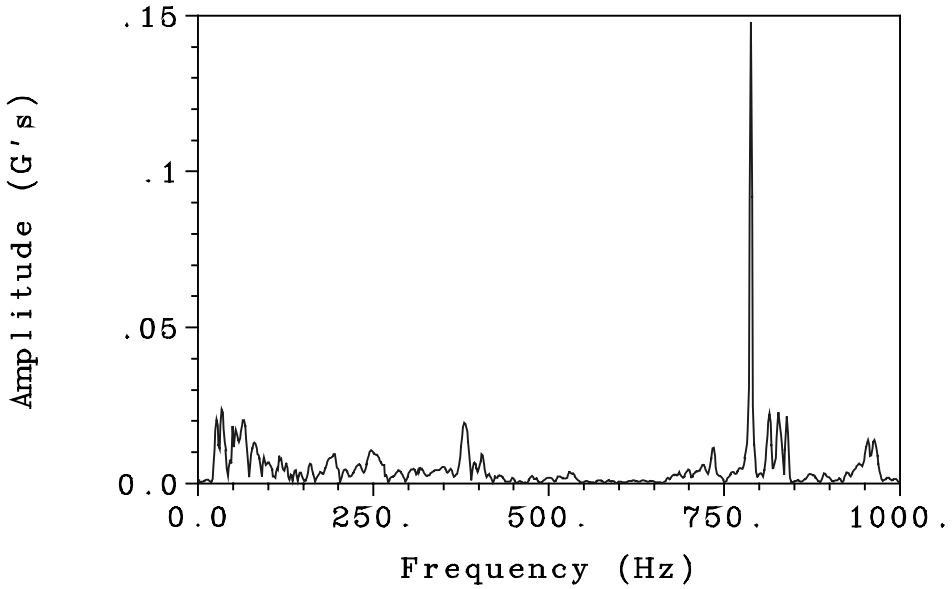

Fig. 38. FFT of a torsion mode twang test of the Flight Model truss in a 0° truss orientation.

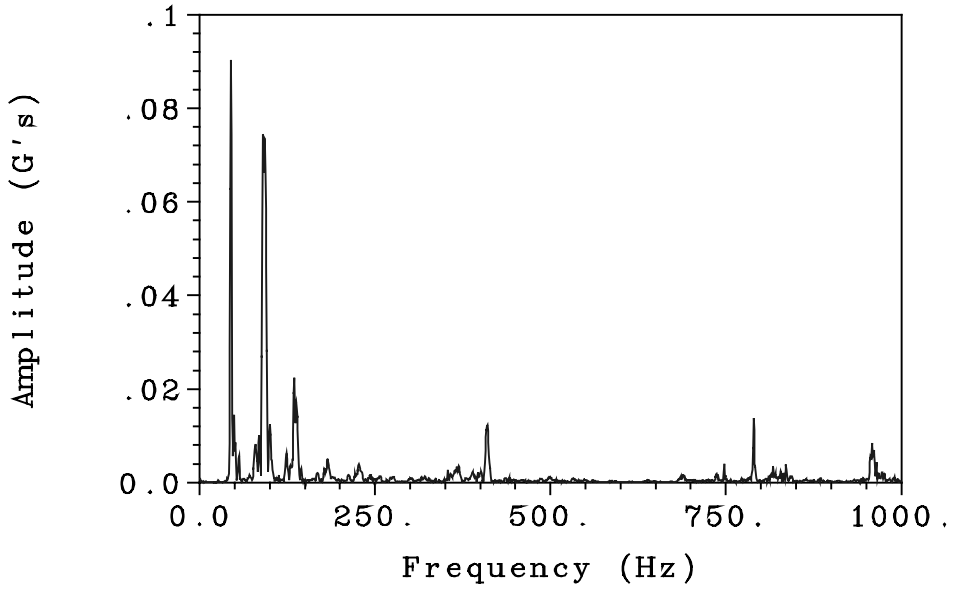

Fig. 39. FFT of a torsion mode twang test of the Flight Model truss in a 90° truss orientation.

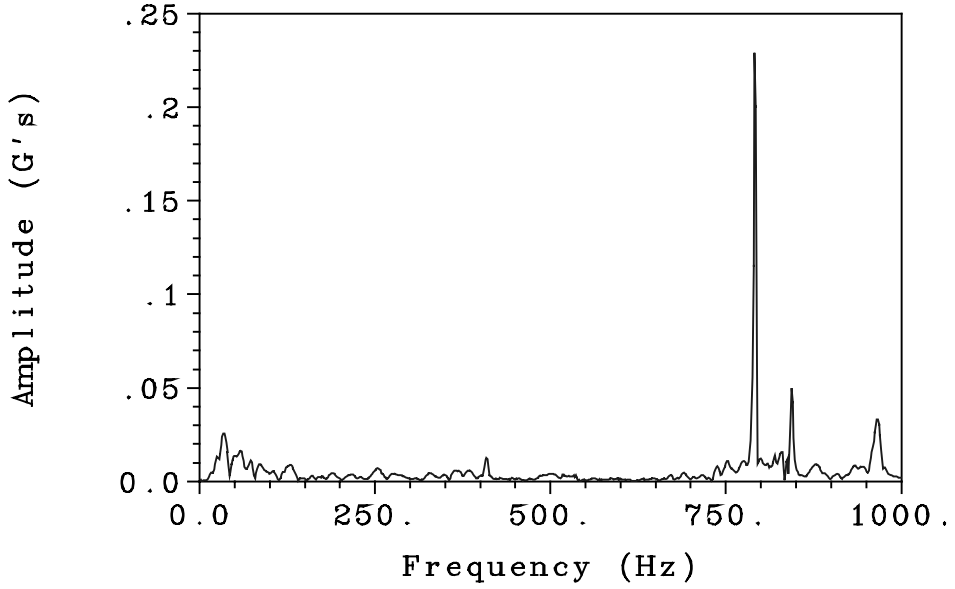

Fig. 40. FFT of a torsion mode free float twang test of the Flight Model truss conducted during a low-G aircraft flight.

7.0 SPACE FLIGHT TESTING

During the week spanning May 1 through May 5, 1995, the Joint Damping Experiment was integrated with the GAS bridge, which would later be installed into the space shuttle. Integration consists of delivering the experiment to NASA at the Kennedy Space Center (KSC) and subjecting it to numerous safety and operational checks to insure a safe and hopefully successful flight. One of the primary concerns of the safety inspectors at KSC was the containment of the batteries. For this reason the battery box was completely disassembled and inspected. After passing inspection the experiment was placed in an insulated GAS canister and prepared for mounting to the GAS bridge. The GAS bridge is a large aluminum structure that spans the space shuttle's cargo bay allowing several mounting places for numerous experiments. A picture of the GAS bridge with the JDX canister mounted to it is shown in Fig. 41. Figure 42 is a photograph of the GAS bridge.

Fig. 41. Photograph of JDX attached to the GAS bridge.

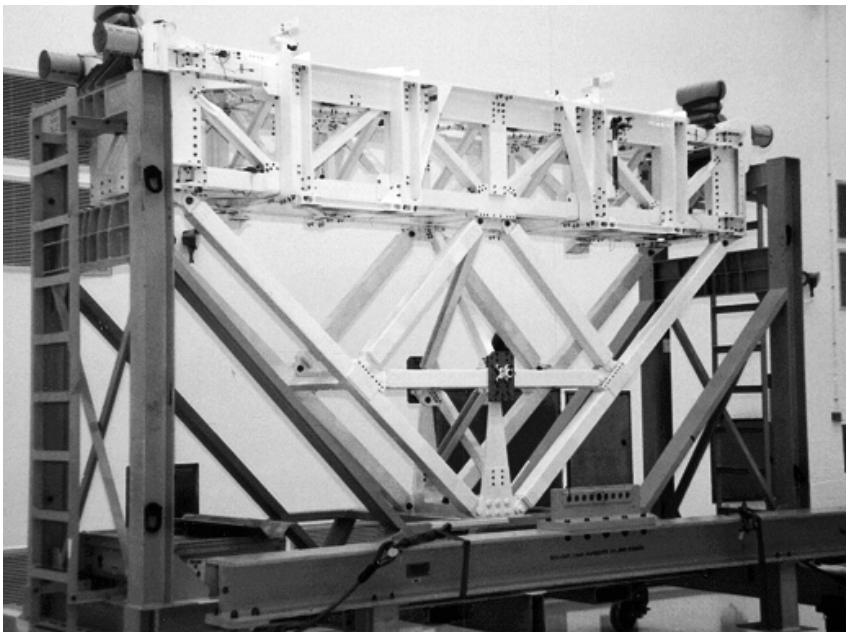

Fig. 42. Photograph of the GAS bridge.

The assembly procedures of the GAS bridge require that when the canisters are attached, they do not induce high preloads in the bridge. For this reason one of the three mounts connecting the GAS canisters to the GAS bridge is described as a "rattle mount." This connecting point has a clearance fit pin in a hinge mounting assembly. This was a cause for concern since JDX is very sensitive to how it is mounted as noted in the Flight Model truss tests. In order to investigate the behavior of the truss before launch, a series of twang tests was performed after the experiment was mounted to the bridge. This series of tests revealed that the two bending modes of the JDX truss was coupling with vibration modes in the bridge. Fig. 43 shows a bend one test taken just after JDX was mounted to the GAS bridge. The coupling with the bridge causes low amplitude vibrations that last several seconds. This is clearly seen in the lower amplitudes of this twang test. Bend two tests also revealed coupling with the bridge. This coupling is believed to be caused by one of several natural modes of the GAS bridge assembly which are excited by the twang tests. It is important to note that when these twang tests were performed, the GAS bridge was not in the cargo bay of the Space Shuttle. When the bridge is mounted in the cargo bay, it is mounted at five points, four at each of the top corners of the bridge and one at the bottom. However, when experiments are mounted to the bridge, it is supported by a large cradle on wheels, which allowed easy transport of the large assembly. Figure 42 shows the bridge mounted in the cradle. The cradle does not attach to the bridge in any of the five flight mounting points. Instead the cradle is bolted to the top beams on both sides of the bridge. This mount proved to be quite flexible and the coupling made it very difficult to interpret the results. When the testing was complete, the batteries were charged a final time.

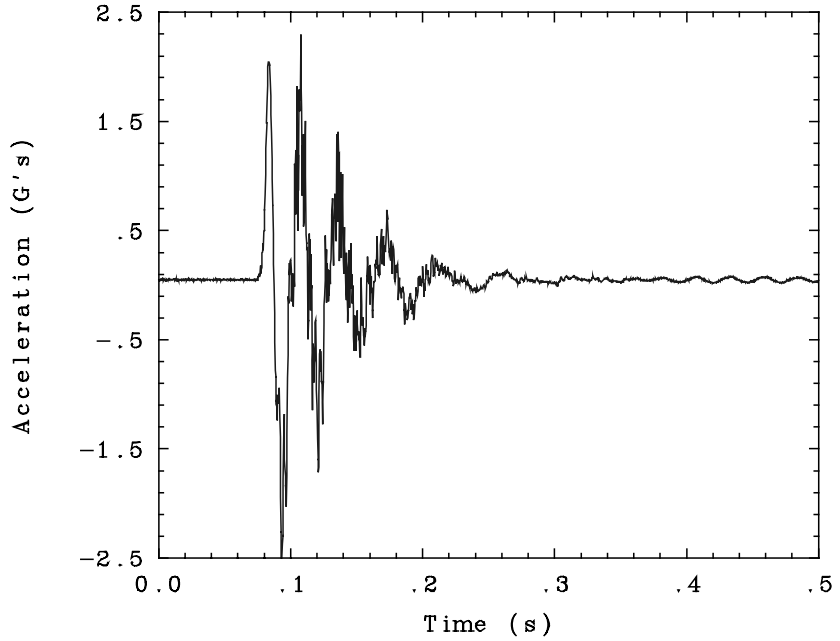

Fig. 43. Bend 1 mode twang test conducted during Space Shuttle integration.

7.1 Modeling of Bridge Coupling

From the results of the integration testing it was apparent that coupling with the GAS bridge could cause problems with analysis of the flight tests. An effort was made to analyze the bridge to determine if the coupling would be a problem during flight. A finite element model of the GAS bridge and accompanying payloads created by Swales and Associates for the CAPL project was obtained. In the finite element model, each GAS payload was represented by a concentrated mass. At the JDX payload location, a beam element was added to the model to represent the JDX truss. This beam was attached at the location of the GAS base plate and had the same mass and frequency characteristics as the truss. A twang test was simulated by displacing the beam element and releasing it. The resulting decay was noted at the same locations where accelerations were measured. Coupling was examined by looking at the output from the accelerometer mounted to the JDX base plate in the Z direction (along the long axis of the truss). During the integration tests, the Z axis accelerometer had the largest output of the three accelerometers mounted to the base plate. During normal ground tests with a "stiff" mount, all the accelerometers mounted to the base plate would not show any movement during the decay. Thus, any motion of the base plate indicates coupling with the GAS bridge.

The model was modified to simulate the twang tests performed during integration. The payloads that were not present when the payload integration testing was performed were removed. However, a problem arose when modeling the cradle that supported the bridge during this testing. As mentioned before, the cradle had hard rubber wheels supporting it and therefore was not a very stiff mount. An accurate model of this mount was very difficult to determine. The cradle model was modified such that the reasonable agreement with measured data was obtained. It was noted that the model was very sensitive to how the cradle was modeled.

The model was then modified to simulate flight conditions. The cradle elements were removed and restraints simulating the Space Shuttle attach points were added along with all the payloads attached to the GAS bridge. Again, a twang test was simulated and the resulting decay monitored.

Figure 44 illustrates the predicted displacement of the base plate in the Z direction for one second during a bend 1 mode twang test. Both the integration test case and the Shuttle flight conditions are illustrated in Figure 44. The coupling of the tip mass and the bridge is quite apparent in the growing and dying of the base plate displacements. The model predicts coupling would occur for both integration and flight conditions. However, coupling during flight was predicted to be much less than the coupling seen in the model of the integration tests. No damping was assumed in this model and the model was believed to be approximate at best.

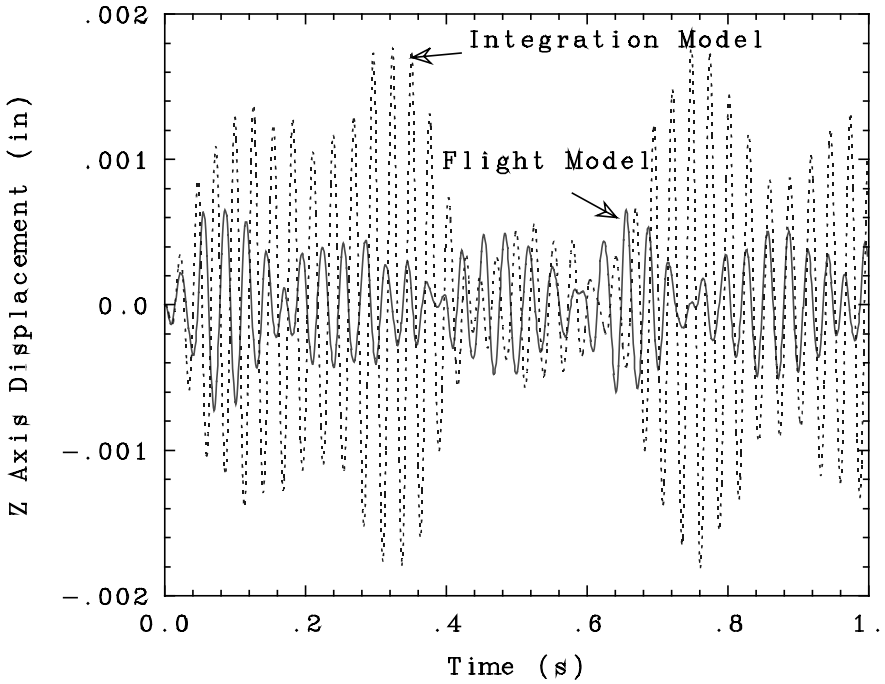

Fig. 44. Predicted Z displacements of the base plate during a bend 1 mode twang test.

A normal modes analysis was conducted on the finite element model of the flight configuration to examine which modes were responsible for the mode coupling. The results showed numerous modes were present with frequencies close 35 Hz. (the bend 1 mode frequency). Two modes at 34 and 40 Hz. have mode shapes which would appear to couple with the JDX truss. These mode shapes are illustrated in Figures 45 and 46, respectively.

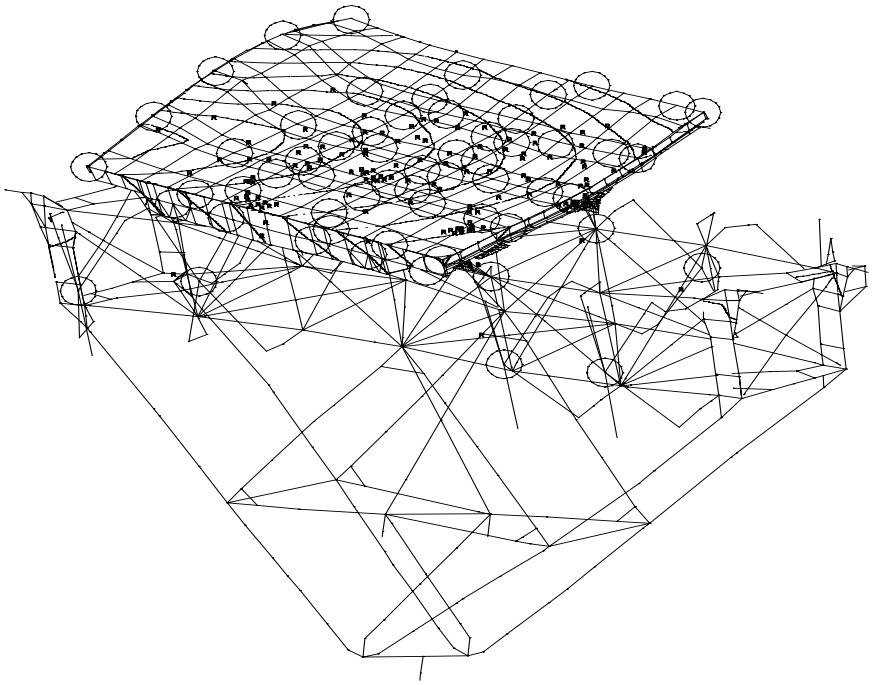

Fig. 45. Predicted 34 Hz. GAS bridge mode shape.

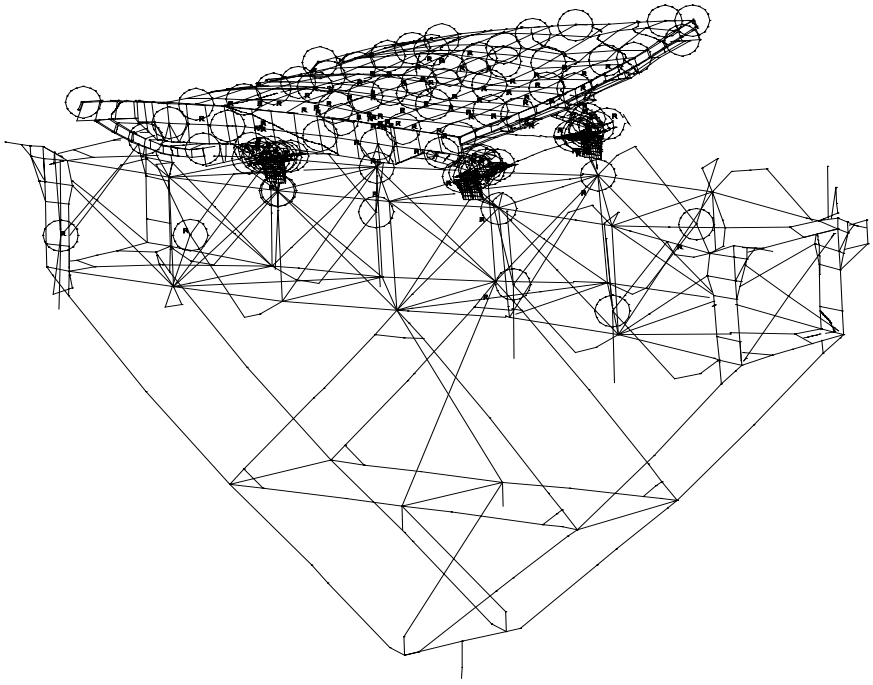

Fig. 46. Predicted 40 Hz. GAS bridge mode shape.

7.2 Flight Results

On September 7, 1995, the Space Shuttle Endeavor was launched successfully from the Kennedy Space Center carrying the Joint Damping Experiment into orbit. The testing schedule as described in Section 3.4 was followed precisely, with the baro-switch closing properly and Relay B closing just before the first astronaut sleep period. Thirty twang tests were performed and temperatures for the first week of the mission were logged. During the week of October 1, 1995, the data and experiment were retrieved from KSC.

The temperature of the experiment during the flight was a concern. These data are illustrated in Fig. 47. The twang tests were conducted between 9 and 10 hours after launch. The experiment during that time had a temperature of approximately 19.5 °C. Thus, room temperature conditions existed during the twang tests and no adjustments due to temperature are needed when comparing the results with ground tests. As is seen in Fig. 47 the lowest temperature the experiment reached during the time recorded was around 0° C. Therefore, even if the testing had been performed later in the mission, temperature would not have been a large concern.

As predicted by the finite element model of the GAS bridge, the coupling that occurred between the experiment and bridge was greatly reduced. Figure 48 is a comparison between a bend one mode test taken during the space shuttle flight and a bend one mode test taken during low-G testing. Mode coupling between the GAS bridge and the truss is only visible in the very low amplitude oscillation that persists after about 0.3 seconds. The coupling can be ignored except at these low amplitudes. The signals are so similar it is difficult to tell them apart. For the bend two mode tests the signals are again similar; however, there is a greater amount of coupling in the bend two tests (see Fig. 49). Figure 50 is a plot of the logarithmic decrement curve of the bend one flight tests versus the logarithmic decrement curve of the bend one low-G tests. These two curves are very similar, though there is some deviation. Possible reasons for this deviation will be discussed in the next section. However, it is reasonable to conclude that the low-G test results are essentially identical to the space flight tests. Thus, the space flight tests have verified the accuracy and conclusions drawn from the data collected on the low-G aircraft. For this reason the space flight tests are regarded as a success. Furthermore, the low-G test platform is believed to provide superior results since no coupling with other structural elements occurs.

The torsion mode twang tests results were essentially identical to those from ground tests at a 0° truss orientation as seen in Figures 37 and 38.

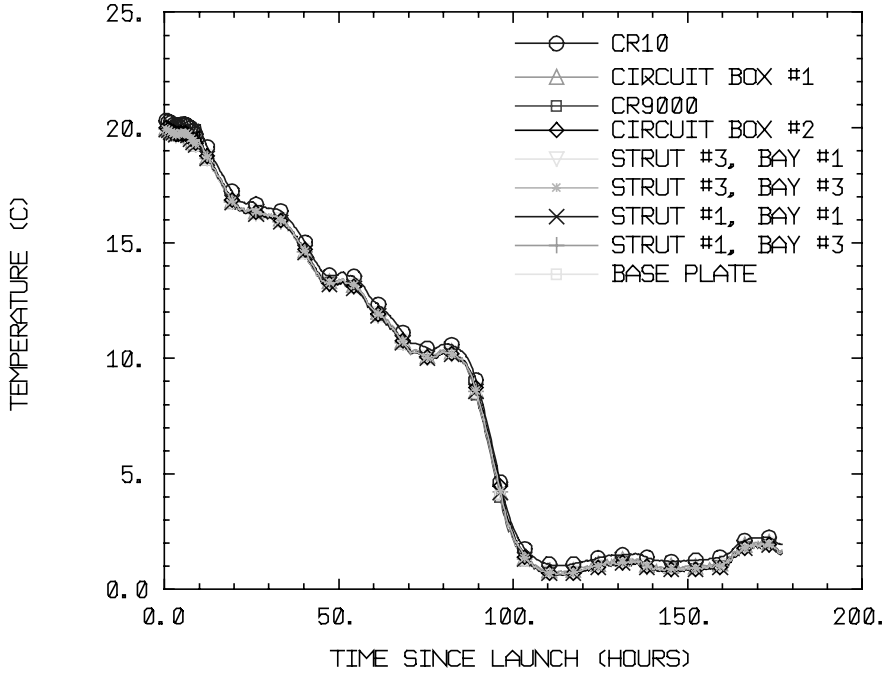

Fig. 47. Illustration of the temperatures recorded during flight.

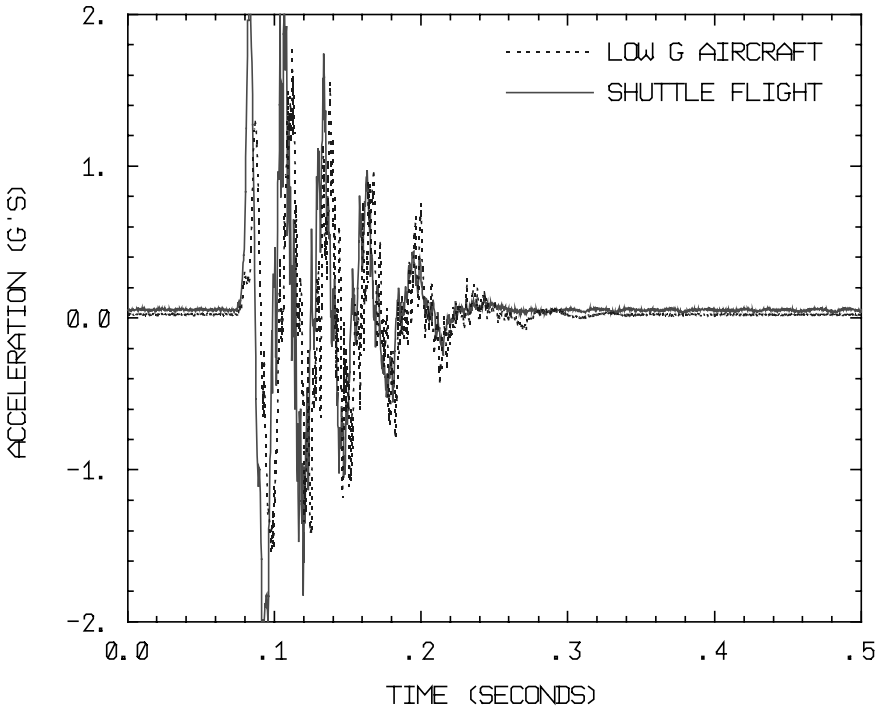

Fig. 48. Comparison of bend 1 mode twang tests from Shuttle flight and low-G tests.

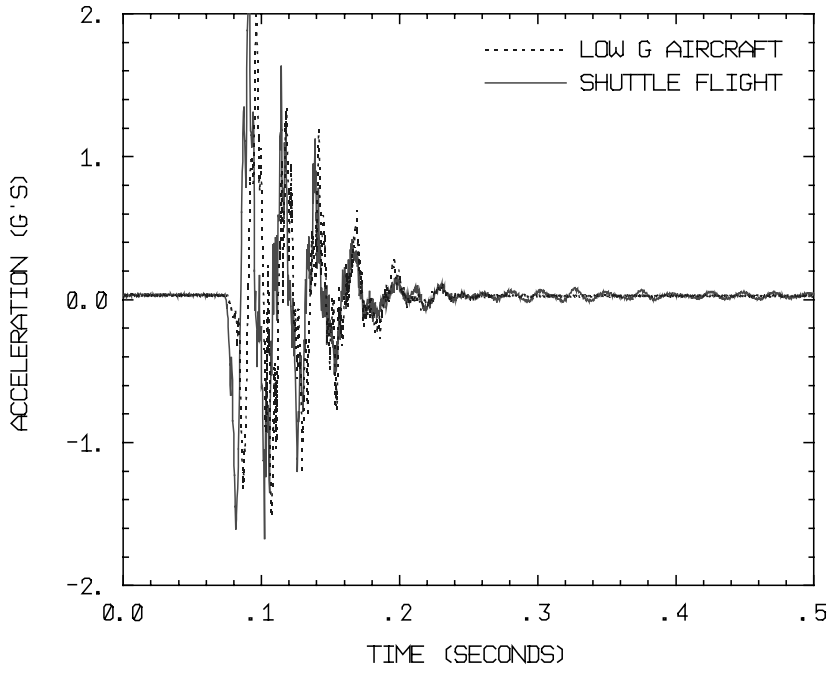

Fig. 49. Comparison of bend 2 mode twang tests from Shuttle flight and low-G tests.

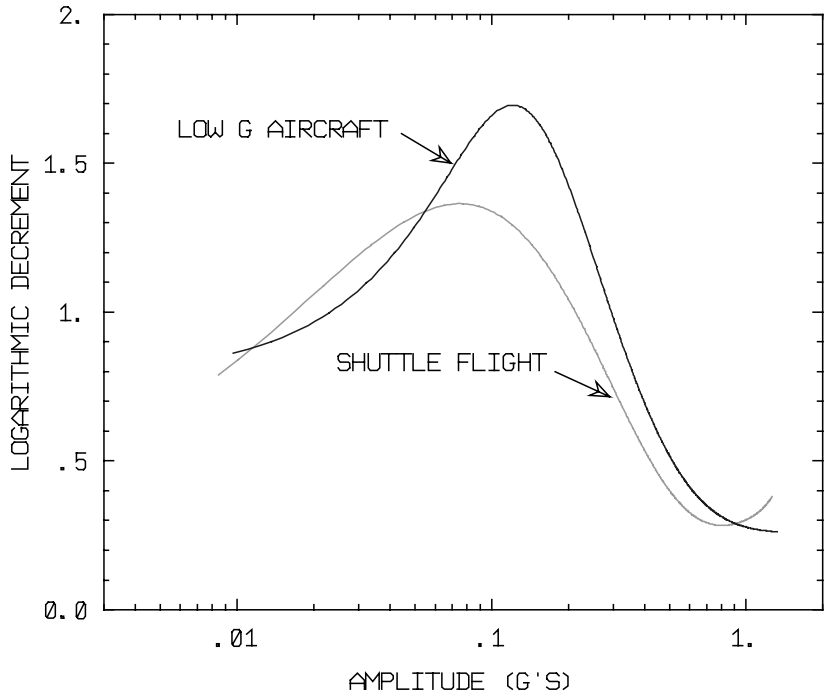

Fig. 50. Comparison of the damping for the bend 1 mode from Shuttle flight and low-G tests.

7.3 Postflight Ground Testing

After the Joint Damping Experiment was returned to Utah State University, a series of ground tests in the 0° truss orientation was conducted in the basement of the Peterson Engineering building. The purpose of these ground tests was to see if the dynamics of the truss had changed since the baseline tests were taken. Since the baseline tests were taken just prior to payload integration, any change in the truss would have occurred between delivery to KSC and retrieval.

Figure 51 is a plot of the decays from a bend one mode baseline test and a bend one mode post-flight test. Clearly the two signals are very similar until lower amplitudes when the post- flight test shows a significant change. This change is illustrated best by Fig. 52. The logarithmic decrement curves for the bend one mode baseline and post flight tests show a striking similarity until the amplitude of accelerations decreases to about 0.2 G. Obviously the dynamics of the truss have changed at low amplitudes. This change was not entirely unexpected. When the truss was shipped to Houston, Texas and back for low-G testing, a similar change occurred. It is suspected that the truss and more importantly the joints are subjected to constant vibrations during the long trip. These vibrations may cause changes in the alignment of the joints allowing for some preloads to be worked out or also produce wear on the joints, which would increase joint deadband. Each time the truss was shipped, the pin diameters were checked but no measurable change was detected in the pins. The clevis and pin-hole diameters could not be checked since the entire truss would have to be disassembled in order to do this. Although no measurable change was found in the pin diameters, obvious wear marks could be seen easily on the pins. These marks formed bands around the circumference of the pin corresponding to the clevis-tang interfaces. The presence of these marks indicates a change of diameter could have occurred in these localized areas even though it is undetectable with our micrometer. Similarly it is logical to assume this same change of diameter would have also occurred in the clevis and pin-hole diameters since the inserts in these holes are made from the same material as the pins. Since the scale with which these measurements are being made is so small, it is possible that the clevis and tang inserts had ridges on their edges. These ridges would cause the pins to wear in the manner observed.

The change in the truss dynamics does make it more difficult to draw conclusions about the influence of gravity on damping. However, it is significant to note that the dynamic behavior of a truss using pinned joints can change over time. Fortunately, going from a 1-G to a microgravity environment has more influence on truss dynamics than the observed “drift” caused by wear or realignment in the joints.

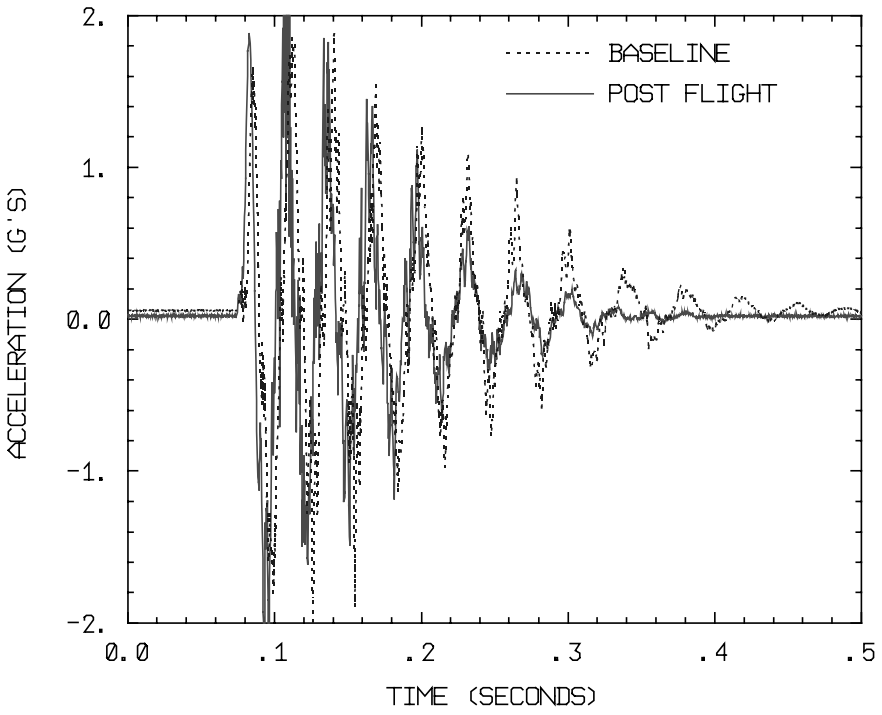

Fig. 51. Comparison of bend 1 mode twang tests from baseline (before flight) and post flight ground tests.

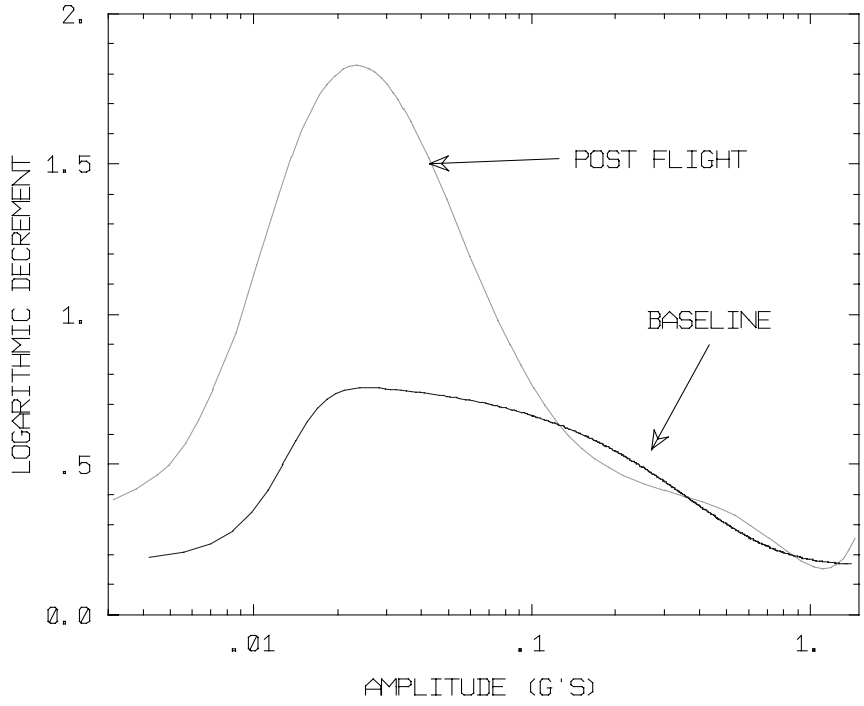

Fig. 52. Comparison of bend 1 mode damping from baseline and post flight tests.

8.0 STRUT CHARACTERIZATION TESTS

Concurrent with the truss twang testing effort was another effort to characterize the dynamic behavior of a single strut with a single pinned joint. The strut used was identical to those in the truss. Experimental data was collected using a force-state mapping (FSM) technique. The strut was subjected to axial dynamic loads and the response of the strut was measured.

8.1 Experimental Setup

Figure 53 illustrates the test setup. The test bed was designed to accommodate struts of various lengths and to test in either a horizontal or vertical orientation although the horizontal orientation was used. It is a two inch thick steel plate mounted to a one inch thick steel plate which is secured to the floor. A cast steel backstop is used as a semi-rigid reference to which a test piece is mounted. A 50 lb. electrodynamic vibrator applies a force to one end of the strut. A force transducer and an accelerometer are mounted axially at the point of load application. Three fiber optic displacement sensors are placed at 120° intervals around the strut. The high output range of these sensors is approximately ±0.002 inch. Averaging the output of the three produces the axial displacement without bending effects. The velocity is obtained by differentiation of the displacement. Figure 54 is a photograph of the test setup.

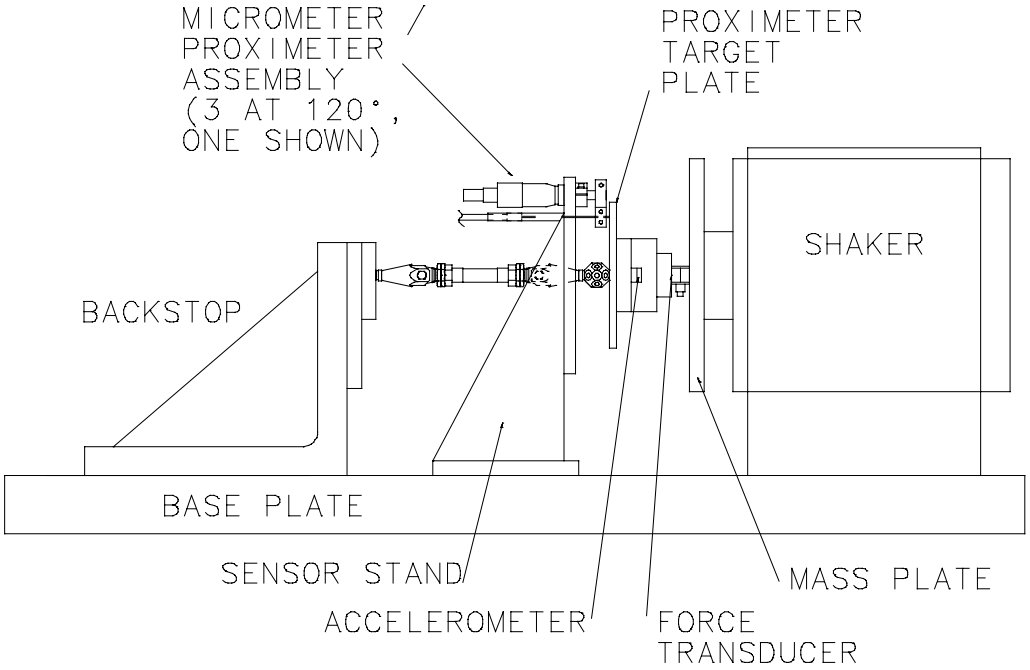

Fig. 53. Illustration of the Force State Map test setup.

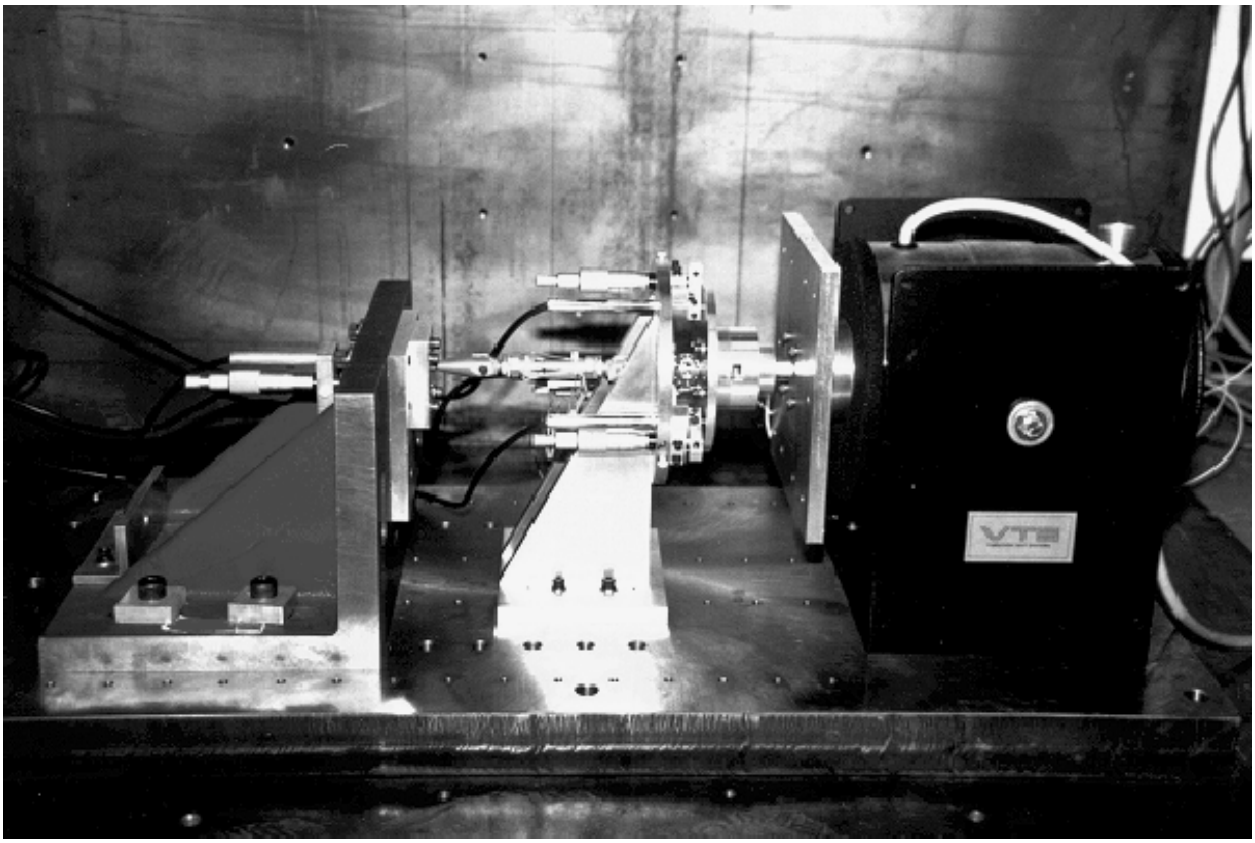

Fig. 54. Photograph of the Force State Map test setup.

The accuracy of the test bed was verified by testing aluminum tubing with known stiffness and low damping characteristics. Initial tests demonstrated that small displacements could occur in the backstop. To compensate for this movement, a fourth displacement sensor was added to measure the motion of the fixed end. One displacement sensor is adequate as it can be mounted axially with the strut. The axial elongation of the strut is found as the average of the front end displacements minus the back end displacement. This elongation is then differentiated to find the velocity. Measured and predicted stiffness data for the test specimens indicated reasonable agreement when the specimen stiffness was in the range of the strut stiffness.

The strut has two types of joints. On one end the joint has a press fit pin and behaves linearly. The other end has a clearance fit pin as illustrated in Fig. 6. Tang and clevis holes are press fit with hardened steel inserts. The pin is a shoulder bolt. The hardness of the pin and the sleeves is intended to reduce wear and therefore reduce dimensional changes affecting performance. This "hard" interface encourages impacting and rebounding as they come into contact. As previously mentioned, the deadband in the pinned joint is adjusted by using different diameter pins.

Testing was done with two tube lengths, three pin diameters, and three forcing frequencies. The three pin diameters were 0.1862 in., 0.1864 in., and 0.1866 in. The hole diameter was 0.1871 in.

Forcing frequencies were 1 Hz, 35 Hz, and 100 Hz corresponding to quasi-static conditions and the bend 1 and torsion vibration modes of the JDX truss.

In order to fill in the restoring force surface, a range of testing amplitudes was recorded. This was done using an amplitude modulated forcing function. One period of the modulating signal was recorded. Thus, the state space was traversed twice. Data rates up to 8000 samples per second where tested to ensure that all of the dynamic characteristics where recorded. Due to memory limitations the tests were recorded at 200 samples per second for the 1 Hertz tests, 2000 samples per second for the 35 Hertz tests, and 4000 samples per second for the 100 Hertz tests.

8.2 Force State Map Results

Initially it seemed that the results in the time domain included too many high frequency vibrations and rebounds to form a single surface. Upon close examination of the results in the displacement-velocity-net force domain, it can be seen that the restoring force is a single surface even when "hard" impacts occur.

Figure 55 shows the surface formed by the tests on the short tubing with a 0.1862 in. pin and 1 Hz forcing frequency. Visually it is possible to identify several nonlinear effects. The deadband is evident in the displacement direction. Due to the deadband, the stiffness is very cubic in nature. In the deadband region, the velocity data makes a step at the origin. This indicates Coulombic friction damping. Outside of the deadband region, the velocity appears to behave linearly, much like linear viscous damping.

To use this surface as an aid in model development, a form of the restoring function must be assumed and fit to the surface. A higher order function could be fit to the surface. However, our objective is to fit relatively simple functions to the surface which could be used in a finite element model of the strut. The stiffness in the simple model could be determined using two different sets of terms. The first would be a linear and a cubic stiffness term. This would fit the data best since it appears very cubic. However, it would require a higher order model. The second is a piece-wise linear fit. This fit would include linear terms representing the stiffness in the tension, compression, and deadband zones. These linear terms are easiest to include in a finite element model. The damping terms could be linear viscous damping and/or Coulomb friction damping.

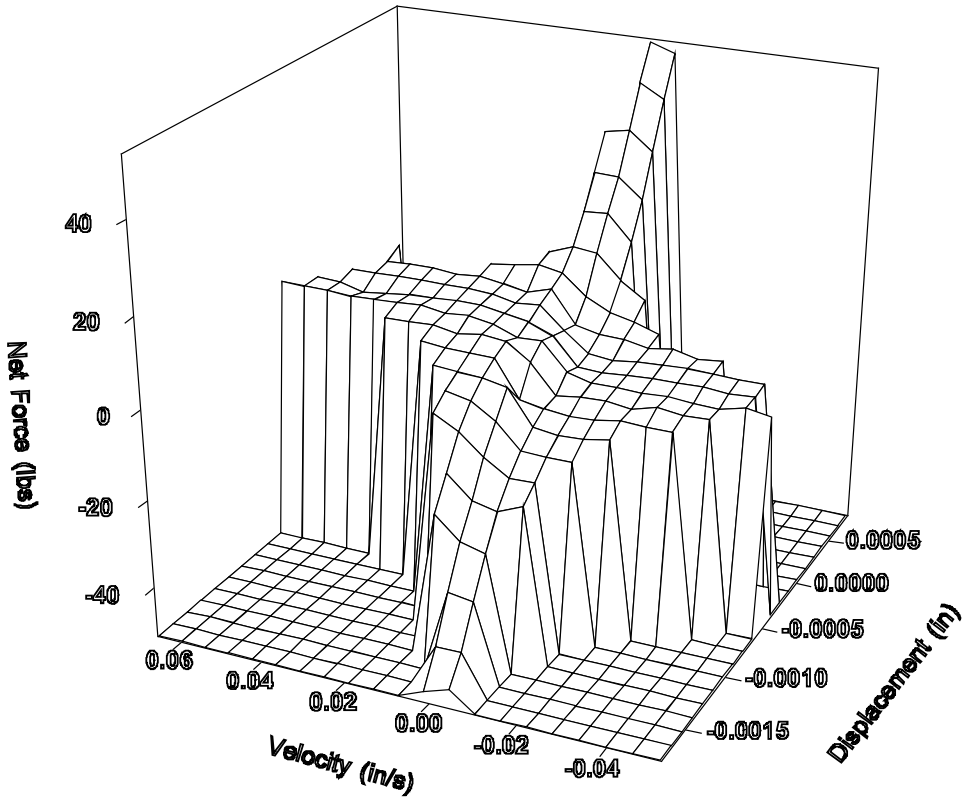

Fig. 55. Force State Map surface for a quasi-static test.

Figures 56, 57, and 58 show the force-displacement curves for the data plus least squares curve fits with the cubic stiffness and combinations of damping terms as given in Eqs. 2, 3, and 4.

$$f(x,\dot{x}) = Kx + K_3 x^3 + B\dot{x} \qquad \textbf{Eq. 2}$$

$$f(x,\dot{x}) = Kx + K_3 x^3 + N\,\mathrm{sign}(\dot{x}) \qquad \textbf{Eq. 3}$$

$$f(x,\dot{x}) = Kx + K_3 x^3 + B\dot{x} + N\,\mathrm{sign}(\dot{x}) \qquad \textbf{Eq. 4}$$

These curves show the data for the short strut with a 0.1862 inch pin and a 1 Hz forcing frequency. Figure 56 (Eq. 2) shows the results with a linear viscous damping term. The fit is good on the tension and compression slopes but very poor in the deadband zone. The Coulomb friction damping term is applied in Fig. 57 (Eq. 3). This term does provide a step function. However, this step does not fit the tension and compression regions well. These regions appear lightly damped. Since the fit is applied based on the error over the entire data set, the step size gets averaged down and the Coulomb term becomes too small to fit the deadband region well. Figure 58 (Eq. 4) shows that the combined linear viscous term and Coulomb friction term still do not fit the deadband region properly when applied over the entire range simultaneously. The worst parts of each are accentuated.

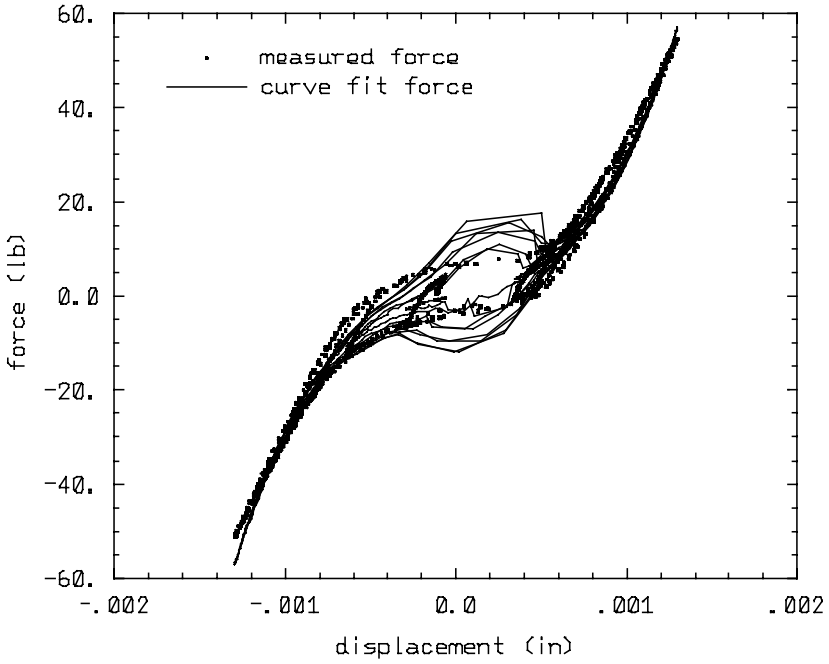

Fig. 56 Plot showing the data for the short strut with a 0.1862 in. pin and 1 Hz forcing frequency compared to the curve fit given by Eq. 2.

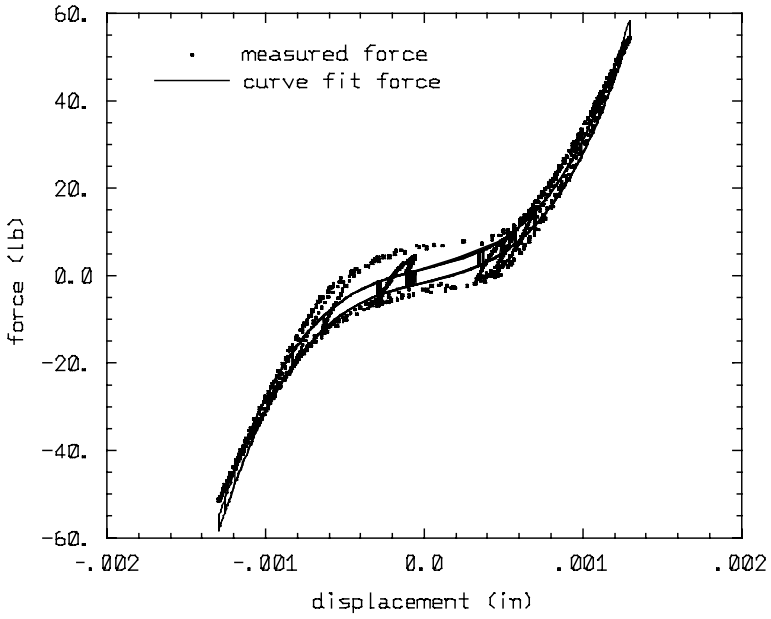

Fig. 57. Plot showing the data for a short strut with a 0.1862 inch pin and 1 Hz. forcing frequency compared to the curve fit given by Eq. 3.

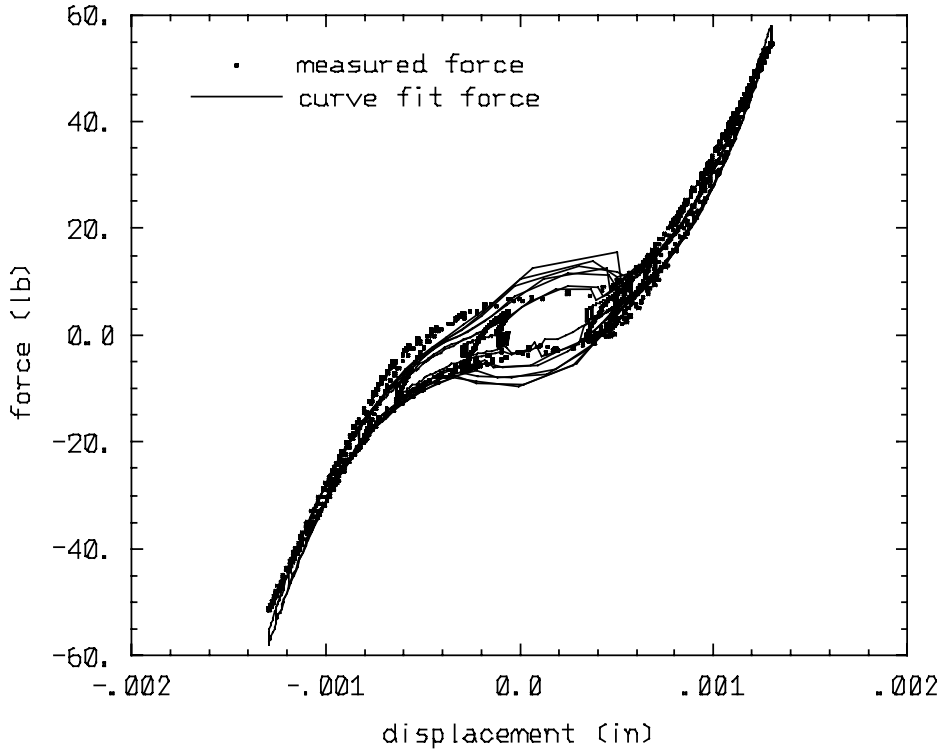

Fig. 58. Plot showing the data for the short strut with a 0.1862 inch pin and 1 Hz. forcing frequency compared to the curve fit given by Eq. 4.

None of these fits seem to work well enough without applying different damping terms in different regions. The viscous term should be applied to the tension and compression zones and the Coulomb friction term should be applied to the deadband zone. Another approach could be used which obtains approximate information from various plots. This approach is best presented by an example.

8.3 Finite Element Modeling Development

As an example of how to use FSM data in the development of a finite element model, a model will be developed for a short strut with a 0.1862 inch pin and 35 Hz forcing frequency. Figure 59 shows the measured map. Based upon this map and the possible nonlinearities in the strut dynamics which were presented earlier, a simple finite element model of the strut in the test bed was constructed as shown in Fig. 60. This figure includes an illustration of the corresponding strut in the test bed. The elements shown in Fig. 60 are available in MSC/NASTRAN. Elements numbered 1 through 6 are beam elements modeling the strut and shaker. Elements 7 and 8 are gap elements which allow deadband during the load cycles. Element 9 is another gap element which is always closed and simulates Coulomb friction during deadband motion. Element 10 is a viscous damping element. The measured masses were lumped to their respective nodes. The finite element model requires the input of several parameters which can be approximated from the measured data.

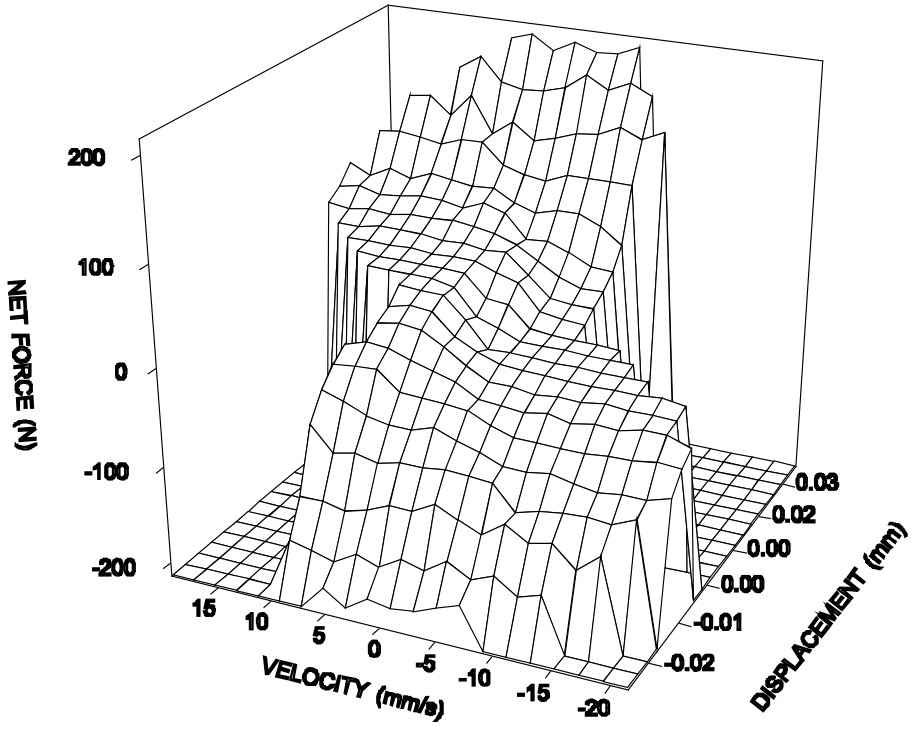

Fig. 59. Force state map of measured data for the short strut with a 0.1862 inch pin and a 35 Hz. forcing frequency.

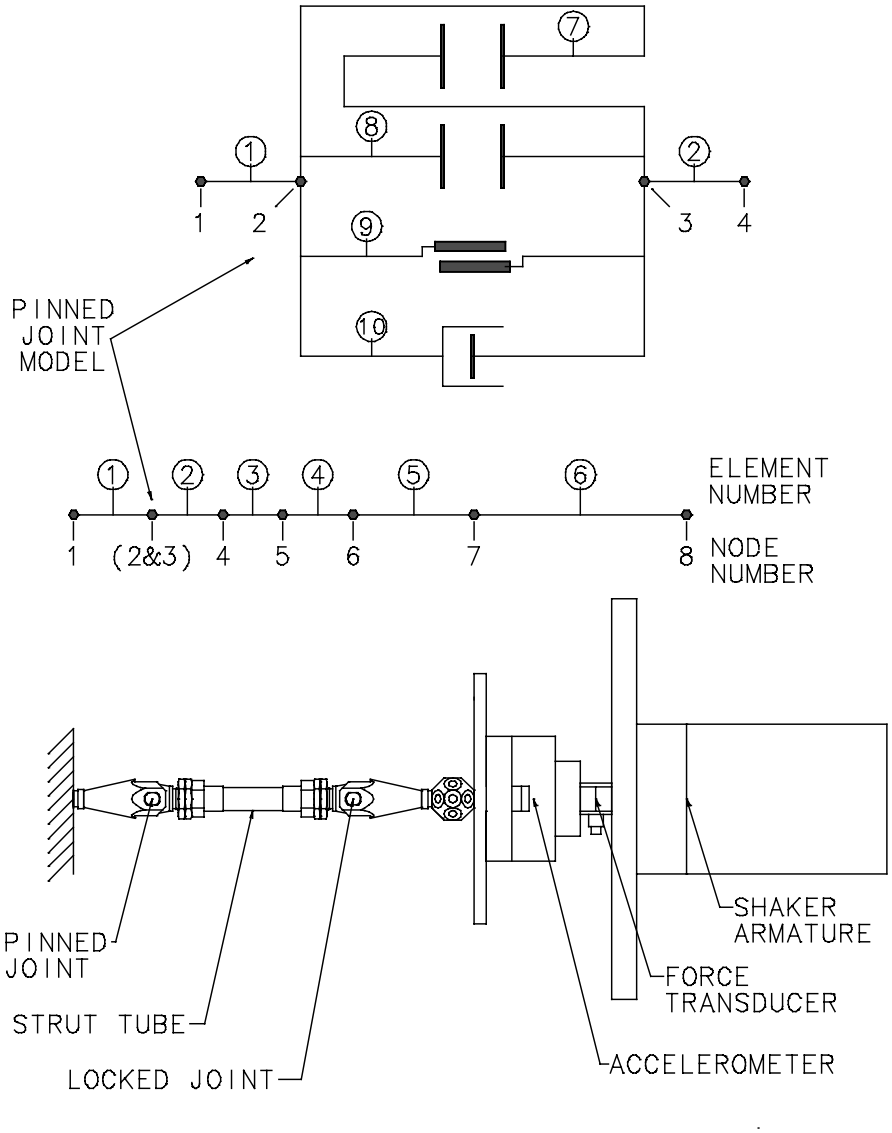

Fig. 60. Illustration of the strut in the test bed and the corresponding finite element model.

First, each beam element must be assigned a stiffness which is a static characteristic. Figure 10 shows the quasi-static data and the average of the tension and compression stiffness, 72,200 lb/in., which is the overall strut stiffness. The stiffness of element 3 (see Fig. 60) is known from physical dimensions. The remaining elements were adjusted in stiffness such that the combined stiffness equaled the measured overall stiffness. The joint model must be assigned a stiffness for when the gap is open (6,200 lb./in. from Fig. 61) and a very large stiffness when the gap is closed.

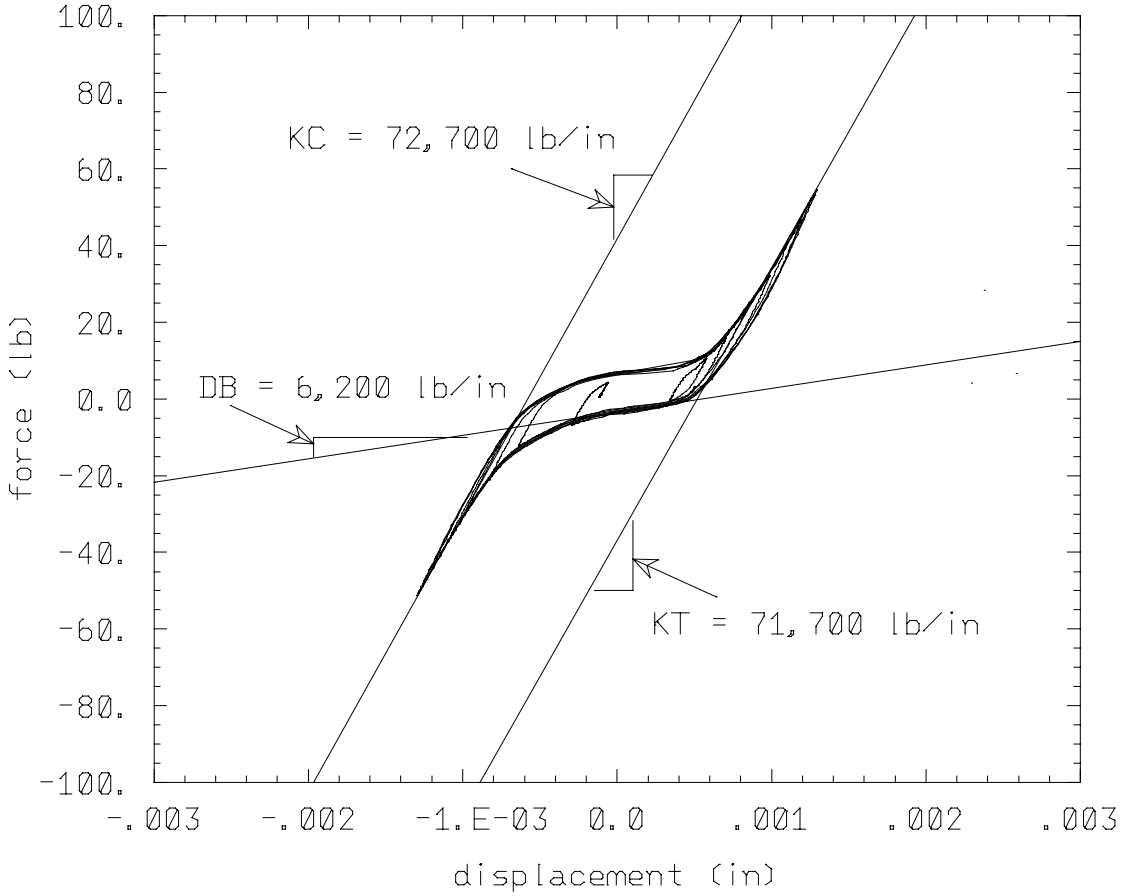

Fig. 61. Illustration of the determination of stiffness from quasi-static test data for the finite element model.

Next, from the dynamic data from tests with a 35 Hz forcing frequency, the characteristics of the gap are determined. The width of the deadband is determined from Fig. 62 to be 0.0014 inch and is used to set elements 7 and 8 in Fig. 60. Three damping type parameters exist in the model. The friction surface (element 9 in Fig. 60) produces a constant Coulomb type force. The value for this force, 5.5 lb., is found as half of the loop width in Fig. 62. The damping coefficient for element 10 in Fig. 60 was set at 40 lb.-sec/in. after running the model and refining it to fit better. Each beam element also has material damping. This loss factor was set to 0.008 which is typical for aluminum at low strains.

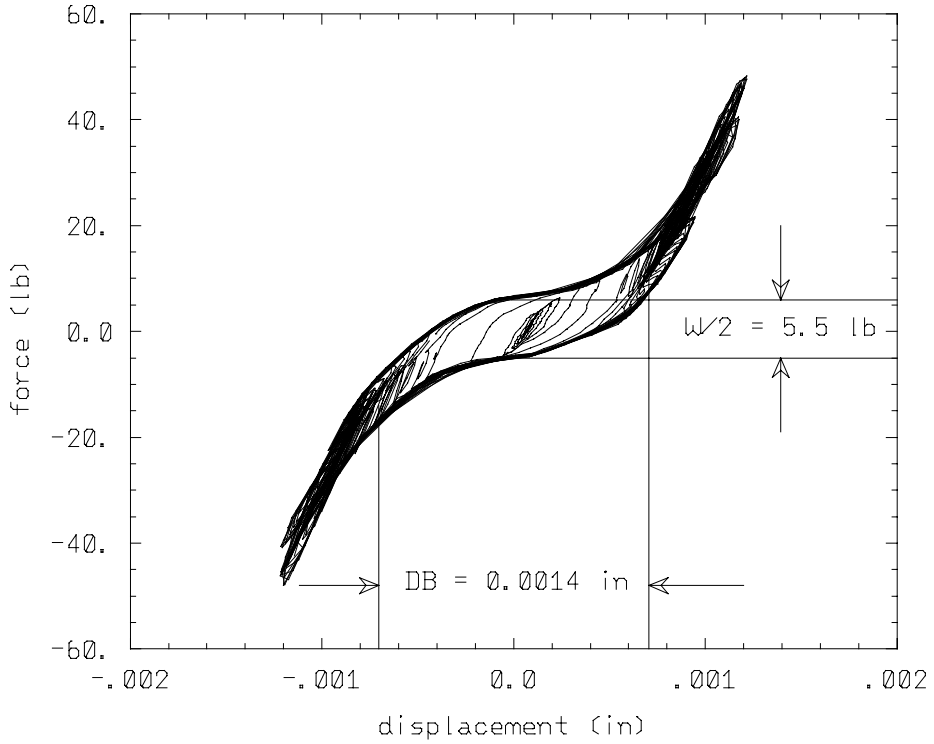

Fig. 62. Illustration of the determination of deadband parameters from dynamic test data for the finite element model.

These parameters were implemented in a MSC/NASTRAN model excited at 35 Hz with an amplitude of 156 N (35 lb.). The result is best evaluated by graphical comparison of the displacement-time history for both the model and the experimental data. Figure 12 shows this comparison. The results compare very well and indicate that this simple strut model adequately accounts for the nonlinearities. The next step in model development would be to adjust the parameters from their nominal values until an even better correlation exists. This would result in a very accurate characterization of the behavior of a strut with a pinned joint in a test bed.

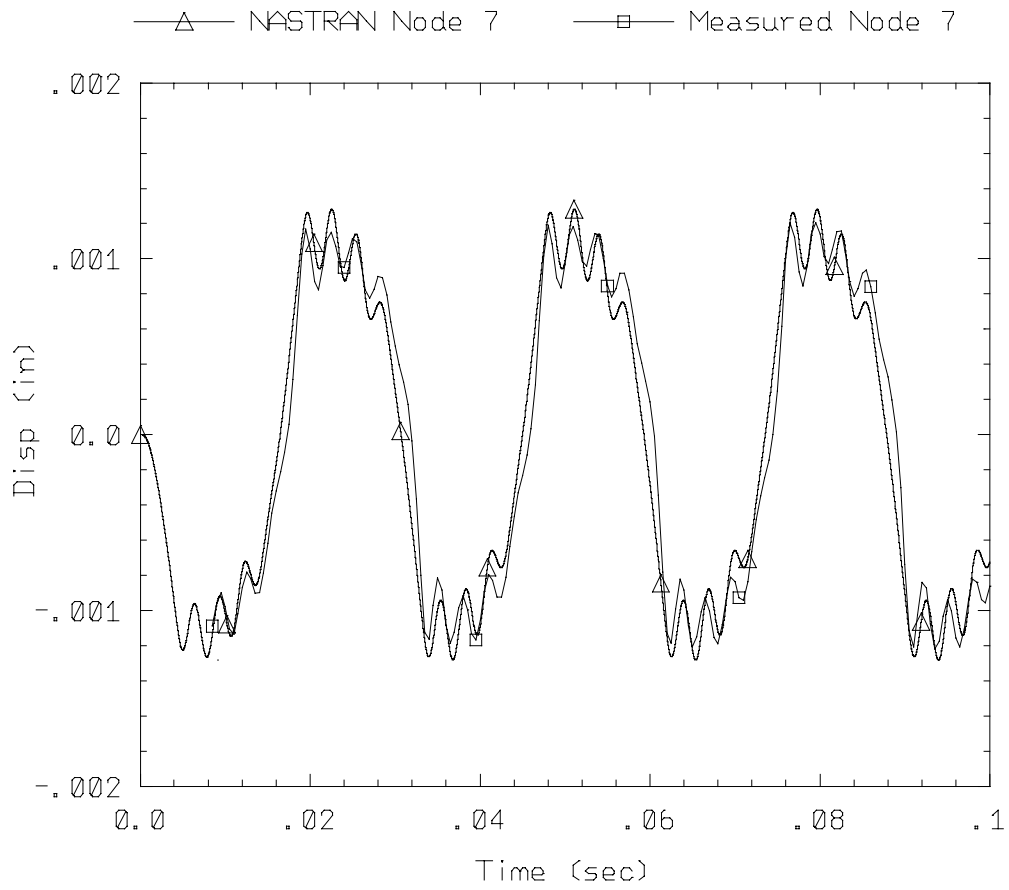

Fig. 63. Comparison of the finite element model to measured data for a short strut with a 0.1862 inch pin and a 35 Hz. forcing frequency.

9.0 NONLINEAR FINITE ELEMENT MODEL OF THE JDX TRUSS

The MSC/NASTRAN finite element model of a strut presented in the previous section was used to develop a finite element model of the truss. However, very significant difficulties were encountered in trying to obtain a solution. MSC/NASTRAN uses an implicit solution scheme and has difficulties when there are numerous gap elements present and more than one gap element can close in a single time step. Although it is possible to obtain solutions, it is a very tenuous process. It was decided to abandon MSC/NASTRAN as a solver and shift to LS-DYNA3D[10] which uses and explicit solution scheme and is well suited to solving problems involving surface contact.

A single strut model similar to Fig. 60 was constructed using elements available in the program LS-DYNA3D. Again, it was desired to construct a finite element model of a strut with an unlocked joint which would be reasonably simple while capturing the most important features of the strut's behavior. A model was made that would account for the deadband, impacting, extensional friction, rotational friction, and equivalent viscous damping in the joint. Impacting and friction can be modeled in LS-DYNA3D by a point contacting or sliding along a surface. The point and surface used to model impacting and friction form a sliding interface. No stiffness is assigned to a sliding interface until contact is made, at which time a very high stiffness is assigned in the direction perpendicular to the surface. After contact, stiffness between the node and surface in the lateral direction is based on the Coulomb friction force.

Figure 64 illustrates a strut and the beam elements used to model the strut in LS-DYNA3D. An unlocked joint is located between nodes 2 and 3. The upper half of Fig. 64 shows the elements used to model the unlocked joint. The coordinate system was defined such that the x axis is aligned with the strut and the y and z axes are orthogonal to the x axis. Nodes 1, 2, 3, 4, 8, and 9 all lie on the x axis but are offset in the upper part of Fig. 64 for clarity. Elements 1 and 2 are beam elements used to model the clevis and tang, respectively. Element 10 is the large square in Fig. 64. Element 10 is a rigid element which is actually formed from several solid elements to define contact surfaces in the joint. The width of element 10 is the pin diameter used in the joint. Nodes 3, 8, and 9 were rigidly connected by elements 8 and 9 which penetrate element 10. Under a tensile strut load, node 9 impacts the surface of rigid element 10, while node 3 impacts element 10 when the load is compressive. Nodes 3 and 9 are initially located a distance equal to half the joint deadband away from the surface of element 10. Node 8 is located inside a narrow slot in element 10 and has two functions. First, it is the hinge point for joint rotations. The slot that contains node 8, although only shown in two dimensions, is three dimensional and prevents relative displacement between node 8 and element 10 in the y and z directions. The slot is very narrow (2×10^{-6} inch) and is a sliding interface for node 8. Second, it provides extensional friction as the joint traverses the deadband. A force F_N, applied to both element 10 and node 8, maintains a constant compressive force at the friction interface (assuming lateral shearing forces are not present). Element 7 is a viscous damper which damps oscillations that occur at the friction interface when normal force F_N is initially applied. Element 6 provides equivalent viscous damping as the joint traverses the deadband. Nodes 2 and 10 are rigidly connected to element 10

to form a single rigid part. Rotational friction may be present when either node 3 or node 9 is in contact with element 10 and there is relative rotation between element 10 and the rigid line of nodes 3, 8, and 9.

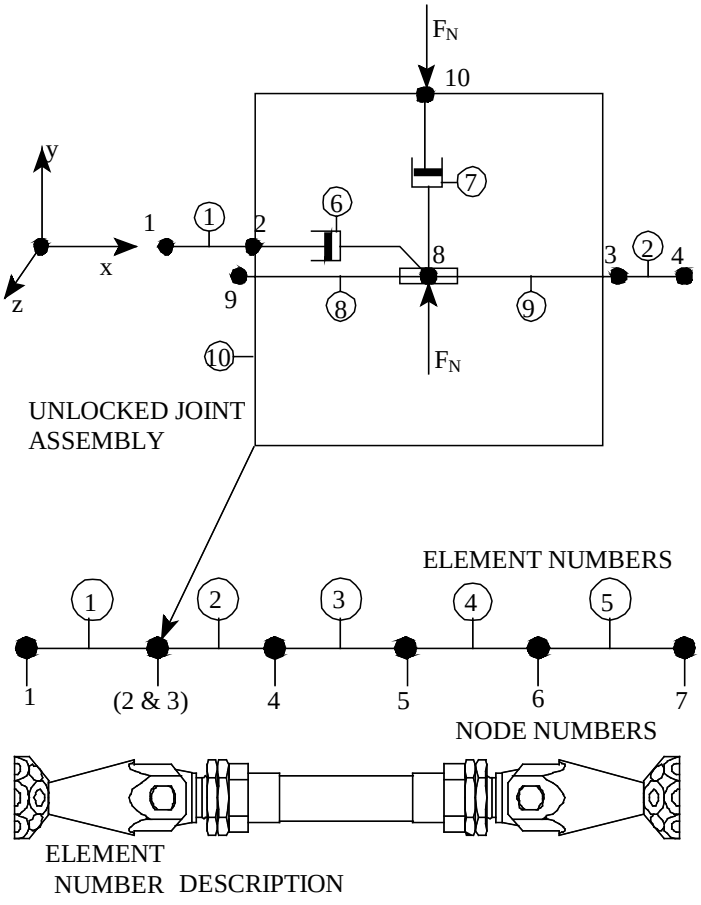

Fig. 64. Finite element model of a strut with an unlocked joint.

Element 10 is actually a composite of several elements formed by combining six solid elements into a single part. These six solid elements are combined in such a way that a slot is left in the center of the part. Figure 65 is a three-dimensional cutaway view of the unlocked joint model which shows five of the blocks used to construct element 10. Care must be taken when constructing element 10 so that node 8 cannot slip out of the slot. Note that node 8 can penetrate slightly into the sliding interface of the slot. If the solid blocks used to construct element 10 do not overlap each other, this penetration of node 8 could allow the node to slip out

of the slot at the interface between two blocks. Thus in Fig. 6, block B is shaded to show how it overlaps A, C, D, and E.

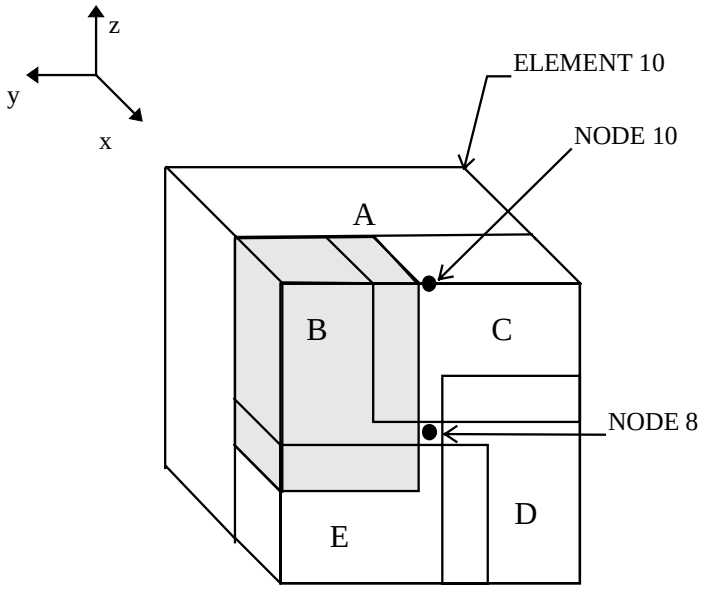

PART	DESCRIPTION
A	END BLOCK
B, C, D, E	OVERLAPPING BLOCKS USED TO FORM FRICTION SLOT

Fig. 65. Three-dimensional view of the unlocked joint model.

9.1 Determination of Model Parameters from Force-State Map Test Results

Although the model shown in Fig. 64 is simplistic, it captures many of the desired features of an unlocked joint. Extensional and rotational friction, equivalent viscous damping, deadband, and impacting are all included in the LS-DYNA3D joint model. Figure 66 shows the expected quasi static force-displacement relationship for the unlocked joint. KC represents the strut stiffness when the gap is closed in compression while KT represents the stiffness in tension. DB is the width of the deadband. For a perfectly aligned strut with identical hole diameters, the deadband width is equal to twice the difference of the hole diameter and the pin diameter. Finally, W represents the width of the hysteresis loop and is twice the friction force for the quasi static case.

At higher velocities the hysteresis loop is wider than the quasi static loop shown in Fig. 55 due to the viscous damping losses.

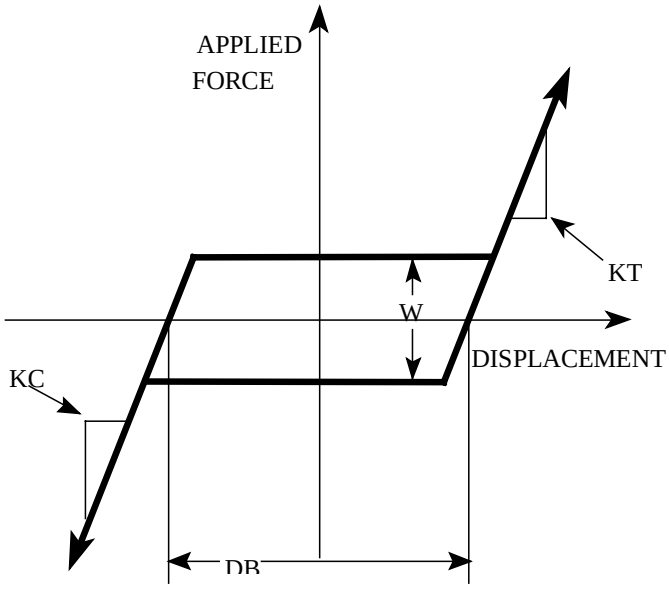

SYMBOL	DEFINITION
KT	STRUT STIFFNESS IN TENSION
KC	STRUT STIFFNESS IN COMPRESSION
DB	LENGTH OF THE DEADBAND
W	WIDTH OF THE DEADBAND (1/2 FRICTION FORCE)

Fig. 66. Expected quasi static force-displacement curve for unlocked joint.

Force-state mapping (FSM) tests reported in the previous section were used to set as many of the strut properties as possible. The data illustrated in Figures 62 and 63 were used to for values of KT, KC, DB, and W. Again, KC and KT represent the strut stiffness in compression and tension, respectively. DB is the width of the deadband. Due to strut misalignment the observed deadband is less than the expected value. The FSM tests showed that the deadband predicted from the force-displacement curve was generally 0.0004 to 0.0007 inches less than the expected deadband. The joint deadband in the model was set equal to the measured deadband rather than the deadband predicted by measuring the hole and pin diameters. W, the width of the quasi static hysteresis loop, represents two times the extensional friction force as the joint moves through the deadband.

Stiffness values were chosen for the five beam elements shown in Fig. 5 such that the overall strut stiffness would be equal to the average of KC and KT. The stiffness of the tubing was easily calculated because it has a constant, known cross section. The tang and clevis stiffness values could not be estimated by hand calculations. Therefore, stiffness values were selected such that the overall model strut stiffness would be approximately the same as the measured strut

stiffness values for long and short struts as well as for struts with both joints locked and struts with one joint unlocked.

The width of the force-displacement hysteresis loop is related to the energy dissipated per cycle in the strut. This width can be modeled by either friction or viscous damping. The equivalent viscous damping in the unlocked joints was chosen such that the width of the model hysteresis curve was approximately equal to the width of the measured hysteresis curve from a FSM test with dynamic loading.

Figure 67 illustrates force-displacement curves which compare results from a single strut finite element model with measured data. The comparison in Fig. 67 is for a 35 Hz sinusoidal load applied to a short locked-unlocked strut. The force shown is the force applied to node 7 (see Fig. 5) while the displacement is the axial displacement of node 7. Although there are differences between the two curves, the areas (and the energy dissipated per cycle of the strut) are nearly the same. Figure 68 shows a comparison between the measured and predicted displacement of node 7 as a function of time. The lowest frequency oscillations are a result of the 35 Hz applied force. The natural frequency of the strut causes the higher frequency oscillations. This higher frequency strut mode causes the irregular hysteresis loops in Fig. 67. Figure 68 shows that the model predicts higher amplitude high frequency oscillations. It is noted that the MSC/NASTRAN model results in Fig. 63 fit the measured strut behavior better. It has recently been determined that the default contact surface is too soft for this application.

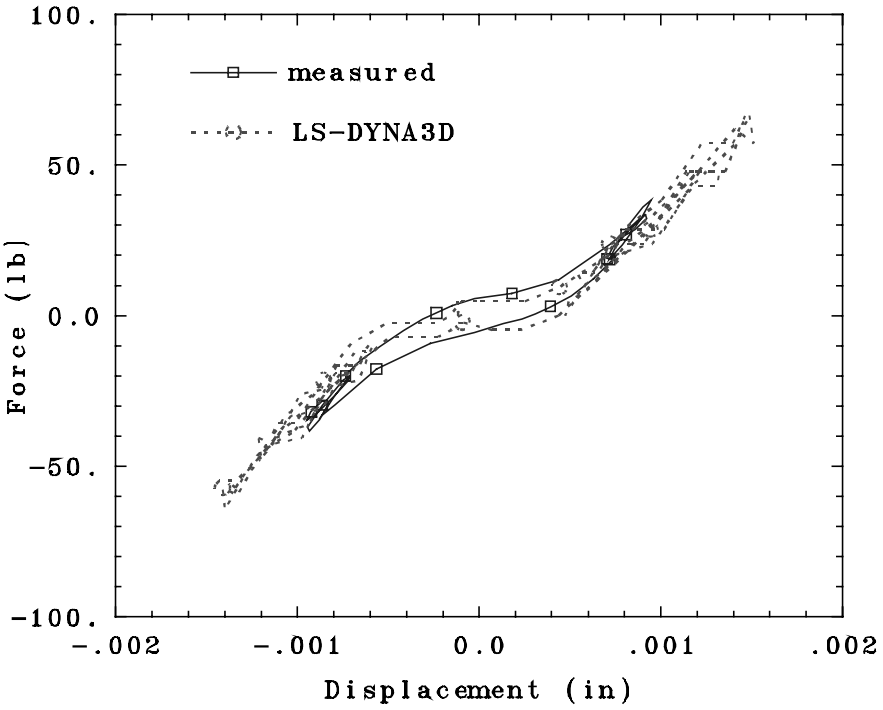

Fig. 67. Measured and predicted hysteresis curves.

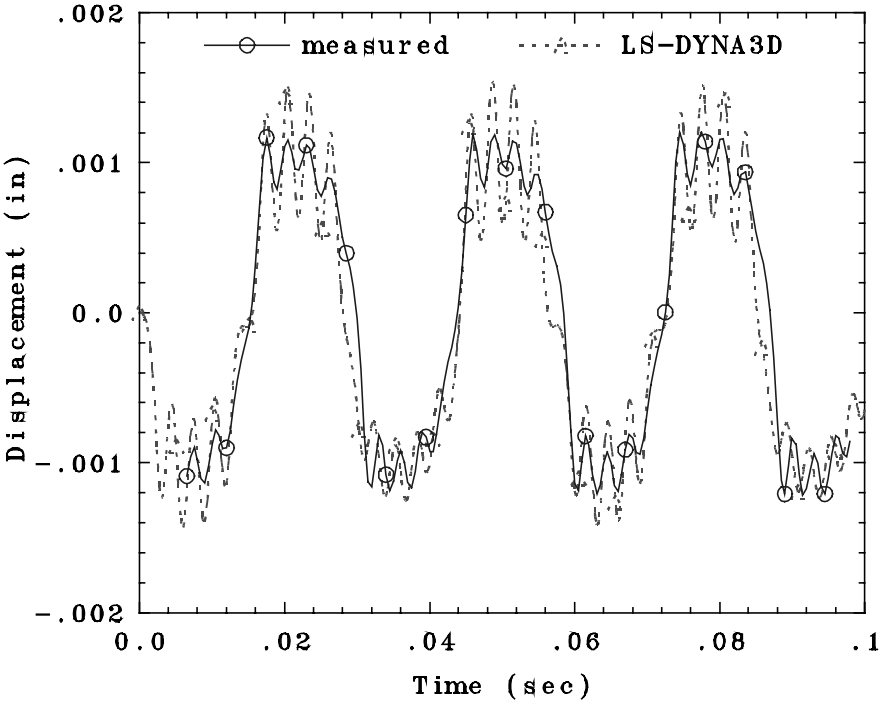

Fig. 68. Measured and predicted time-displacement curves.

9.2 Finite Element Model of the Truss

The single strut finite element models were extended to model the entire JDX truss. Figure 69 illustrates the finite element model. Other than the sliding interfaces at the unlocked joints, the truss was modeled using beam and plate elements. The expected deadband in a joint can be computed as twice the average clevis and tang hole diameters minus the pin diameters. The actual deadband at each unlocked joint is influenced by strut misalignment. It was not possible to measure the "effective" deadband of each unlocked joint after the truss was assembled. An estimate of "effective" deadband for each joint was obtained by using two times the smallest of the two clevis hole diameters and the tang hole diameter minus two times the diameter of the pin.

A parameter called global damping is used in LS-DYNA3D to provide a small amount of damping for each node in a deformable structure. Global damping was used to represent low level material damping. In essence, global damping defines a viscous damper between each node of the structure and ground. The equivalent viscous damping for each node is proportional to the mass assigned to the node.

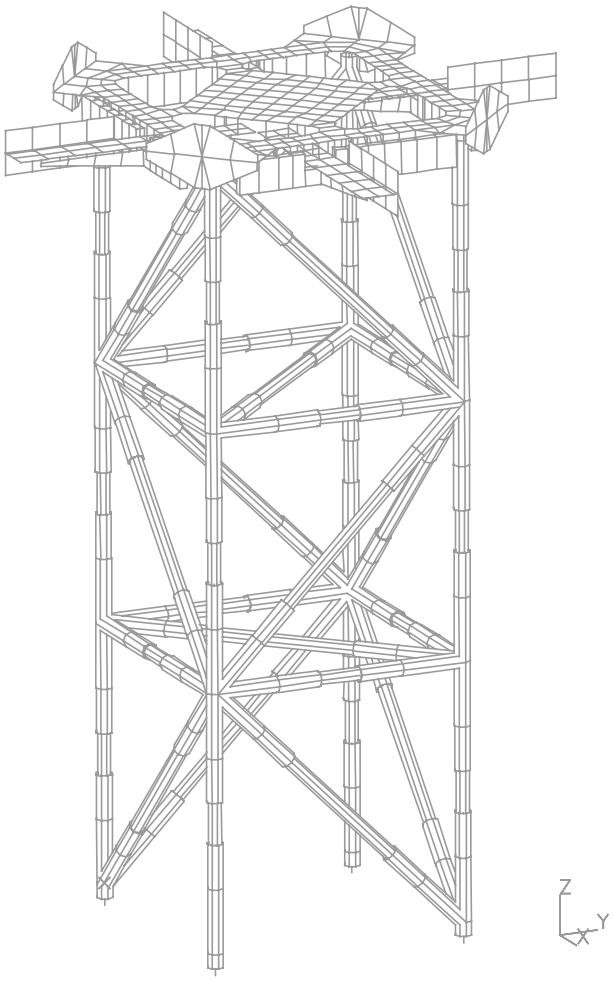

Fig. 69. Illustration of the finite element model of the JDX truss.

In order to find the initial deflected position of the truss in either the bend 1 or bend 2 directions, a 40 lb ramped force was applied to the tip mass for 0.2 seconds, then the force was held constant for 0.3 seconds to allow the structure to come to rest. A large value of global damping was used while the truss was being deflected so that all truss vibrations would damp out quickly. At 0.5 seconds the global damping was decreased and the force was removed from the tip mass to allow the truss to vibrate freely. The displacements, velocities, and accelerations for each node were stored at 3000 samples per second which was the same sampling rate used in measured data.

A truss model with all of the joints locked was used to determine an appropriate value for global damping. The global damping was adjusted in the truss model until the results matched the measured data for the truss with all joints locked. When the truss was excited in the bend 1 direction, a global damping parameter of 3.0 lb.-sec/in modeled the measured data well. The global damping was set to 20.0 lb.-sec/in during the 0.5 second truss deflection period. Figure 70 illustrates the deflection of the center of the tip mass in the bend 1 direction. Figure 71 shows the acceleration of the center of the tip mass for both the measured data and the LS-DYNA3D model. The release of the tip mass for the model was shifted to 0 seconds in Fig. 71 to match the measured data. It can also be seen from Fig. 71 that the locked truss natural frequency predicted by the model matches the measured results for the bend 1 direction.

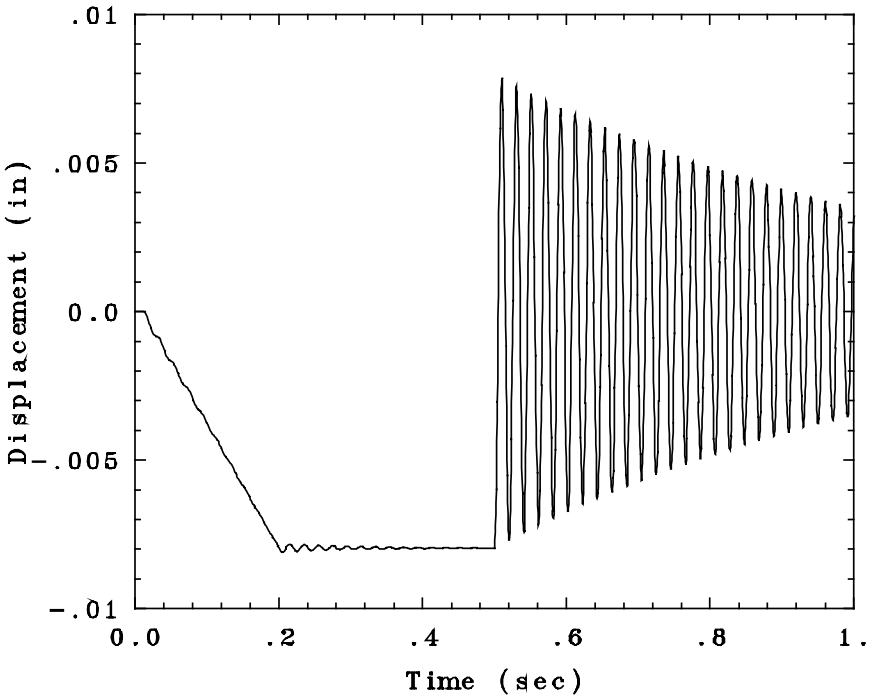

Fig. 70. Bend 1 displacement of tip mass in locked truss model.

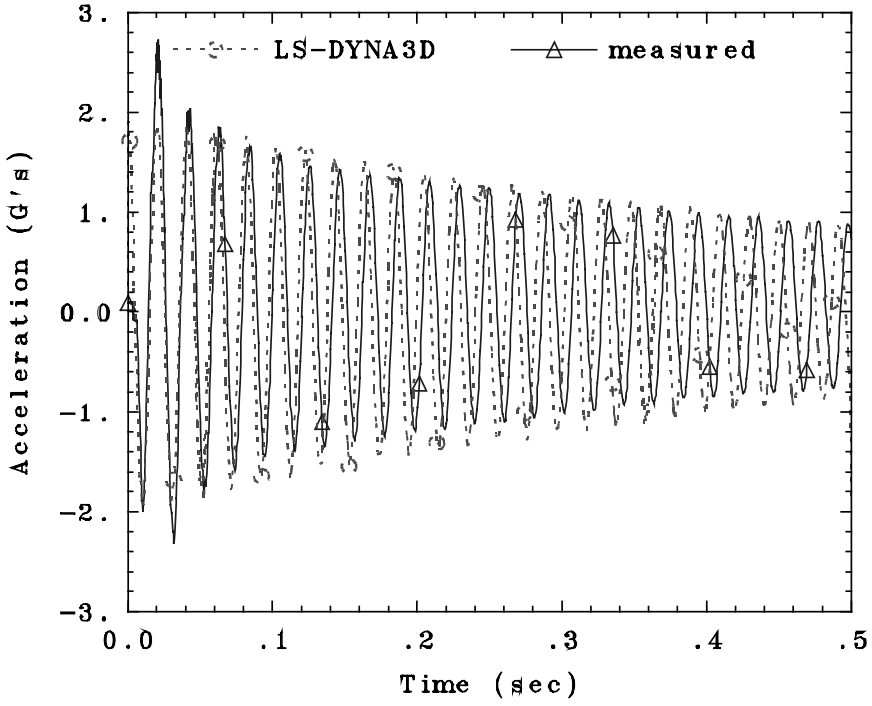

Fig. 71. Bend 1 acceleration for a locked truss in 0-deg orientation.

The truss model was modified to include eight joints unlocked. Figure 72 compares the model and measured results for a test in the bend 1 direction in a micro gravity environment. When power to the magnets in the flight model truss is turned off, the magnetic force decays in an exponential fashion. The time constant for the decay is not known, but it is approximately 0.01 seconds. This decay occurs during the first, short peak in the acceleration data. The analytical model uses an instantaneous release of the tip mass. The release of the truss in the LS-DYNA3D model was shifted to occur at about 0.1 seconds so as to coincide with the second acceleration peak in the measured data. The model predicts well the natural frequency in the bend 1 direction (which is a function of amplitude), the high frequency "hash" in the acceleration data, and the structural damping of the truss. The results for the bend 2 direction are similar to the bend 1 results and thus are not included in this paper.

Figure 73 shows the measured and predicted results for the bend 1 direction in the 0° truss orientation in a 1 G environment. The measured data shows a significant decrease in damping while the predicted decay is very similar to the micro gravity environment. Figure 74 compares the bend 1 results in the 90° truss orientation when gravity induced strut preloads are maximized. In this case the model does a good job of simulating most of the effects of high gravity preloads. However, structural damping in the model is too low. The cause of the discrepancies in the 1 G environment tests is currently unknown.

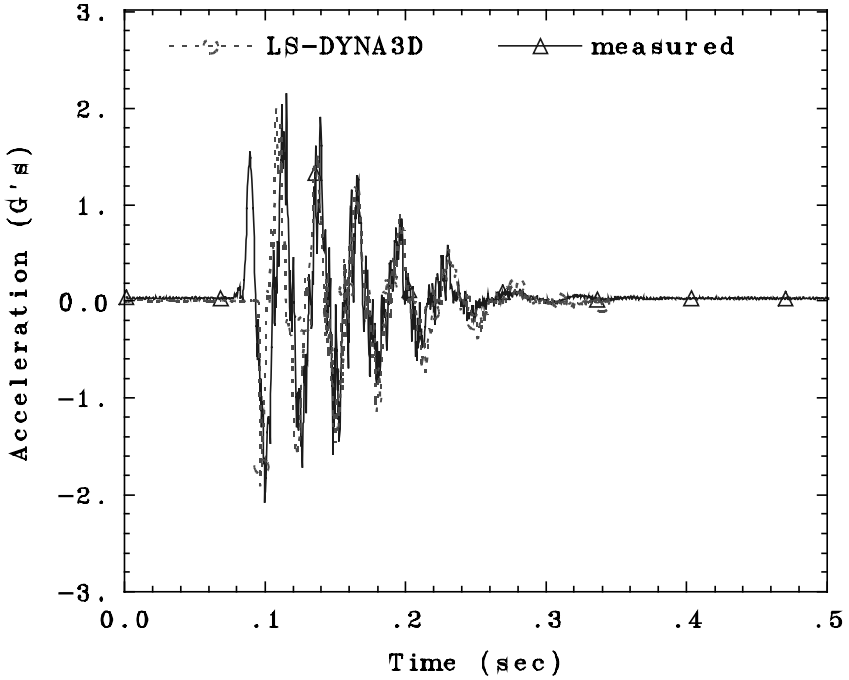

Fig. 72. Bend 1 acceleration for an unlocked truss in micro gravity.

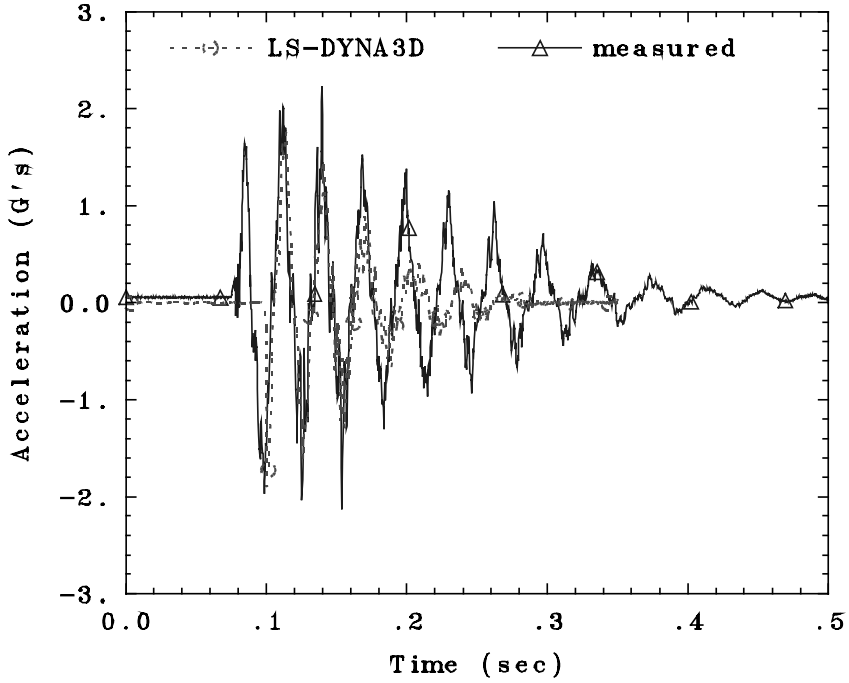

Fig. 73. Bend 1 acceleration for an unlocked truss in 0° truss orientation.

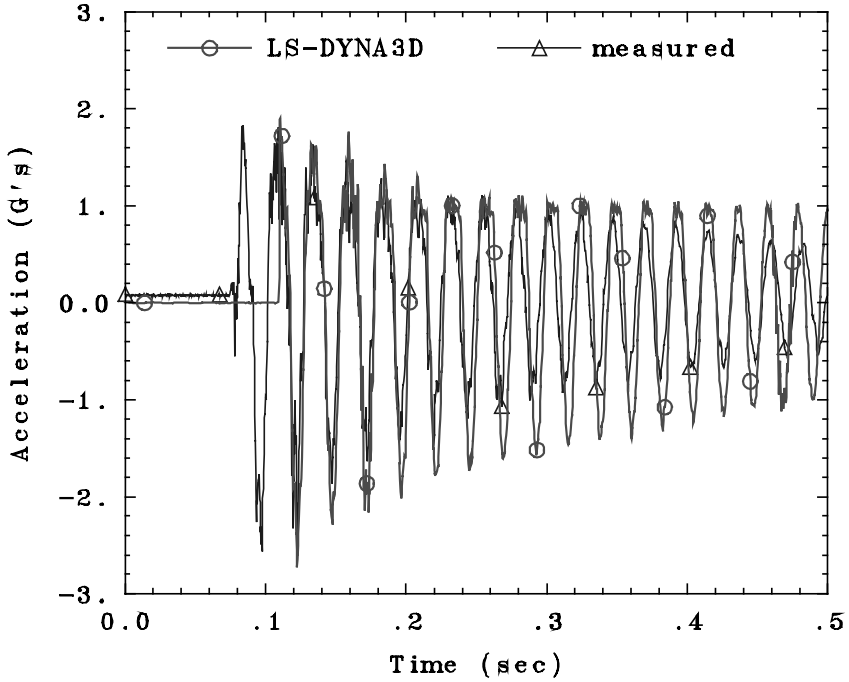

Fig. 74. Bend 1 acceleration for an unlocked truss in 90° truss orientation.

The truss model torsion mode was excited and compared with the measured data. Two 20 lb forces were applied to the arms of the tip mass in order to twist the truss. Figures 75 and 76 compare the measured and predicted torsion tests for a locked truss and an unlocked truss, respectively. The results were shifted in time in order to have a similar amplitude peak in the predicted output occur at the same time as a measured peak. It is seen from Fig. 75 that the global damping chosen for the bend 1 mode is too large for the torsion mode. An accurate model of the torsion mode requires a new global damping parameter.

It is informative to look at the frequencies being excited in the truss during the torsion tests. Figures 77 and 78 show the locked truss frequencies for measured and predicted torsion tests, respectively. Both figures were generated with about 0.2 seconds of data after the release of the tip mass. The torsion mode is seen at approximately 110 Hz. Although not at the same frequencies, both figures show that higher frequency modes are being excited in the locked truss torsion test. A variety of modes in the tip mass and torsion arms could produce the observed response. Figures 79 and 80 illustrate the frequencies excited in the measured and predicted torsion tests for a truss with eight unlocked joints and a truss orientation of 0°. In both cases the 110 Hz torsion mode disappears and only the higher frequency modes can be seen. It is significant that a mode that would be predicted by a linear model of the truss can disappear when a few clearance fit pinned joints are included in the structure. The cause of this response is unknown. It is, however, interesting that the model and measured data agree in the disappearance of the torsion mode when the truss uses a few unlocked joints.

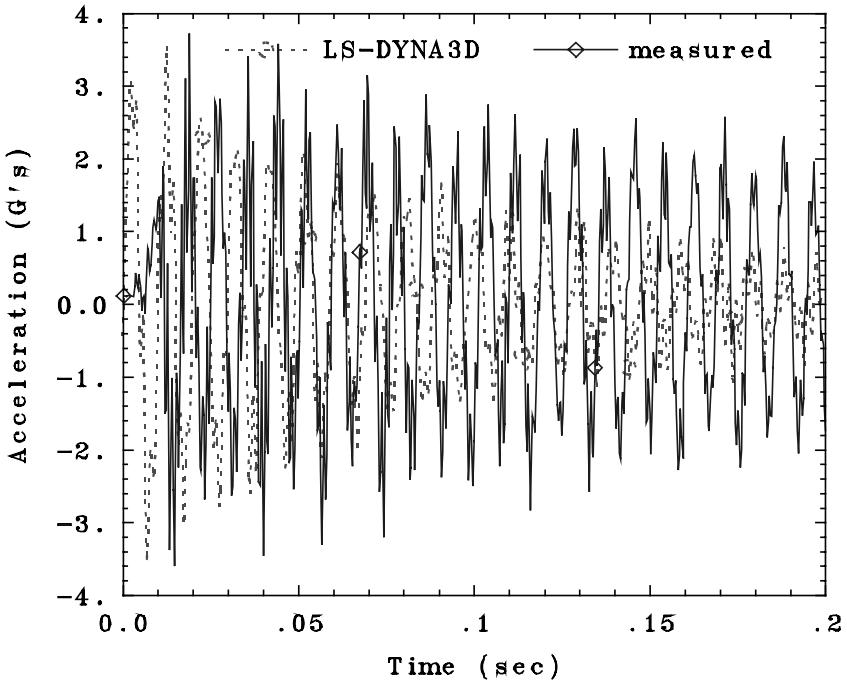

Fig. 75. Torsion test acceleration for a locked truss.

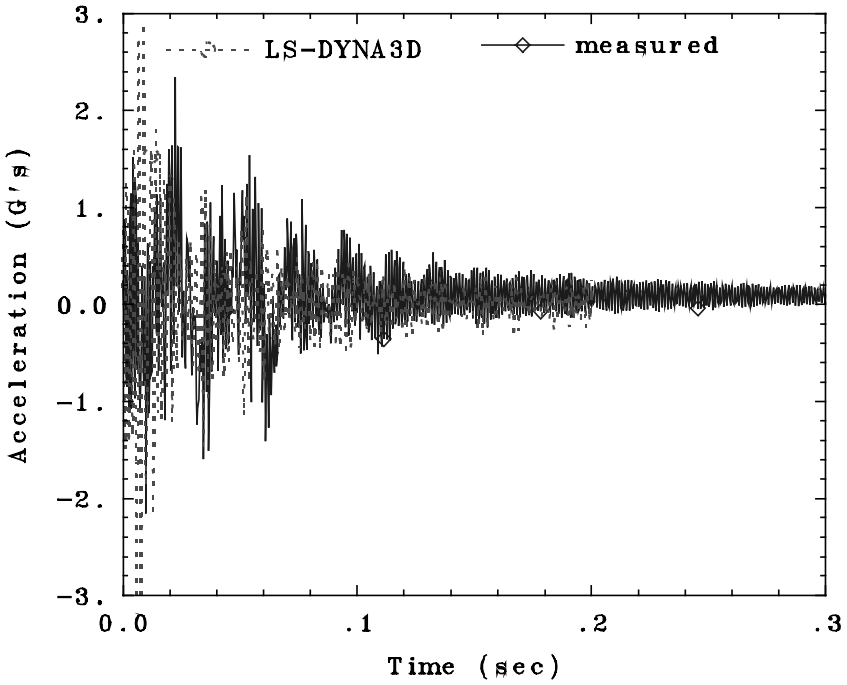

Fig. 76. Torsion test acceleration for an unlocked truss in micro gravity.

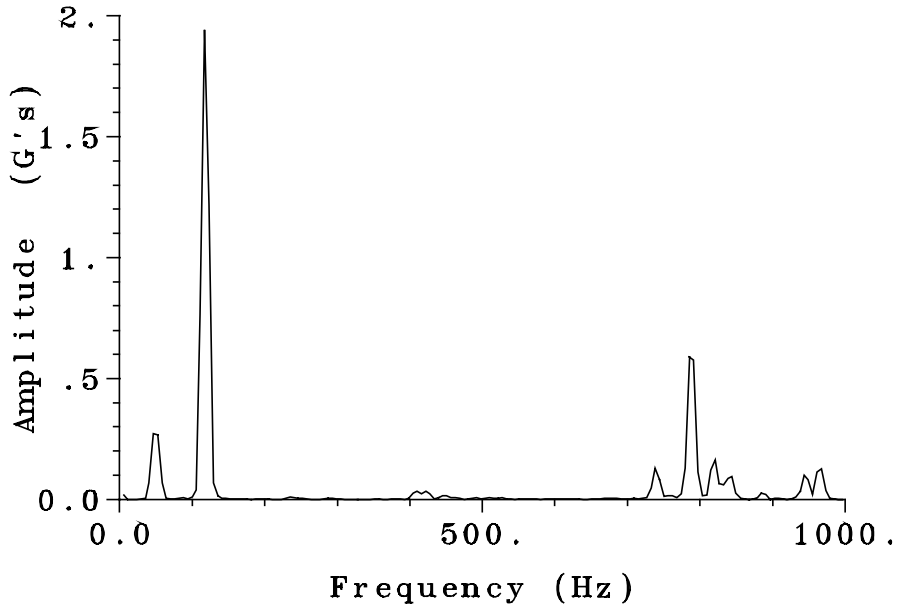

Fig. 77. Measured torsion test frequencies for locked truss in 0° truss orientation.

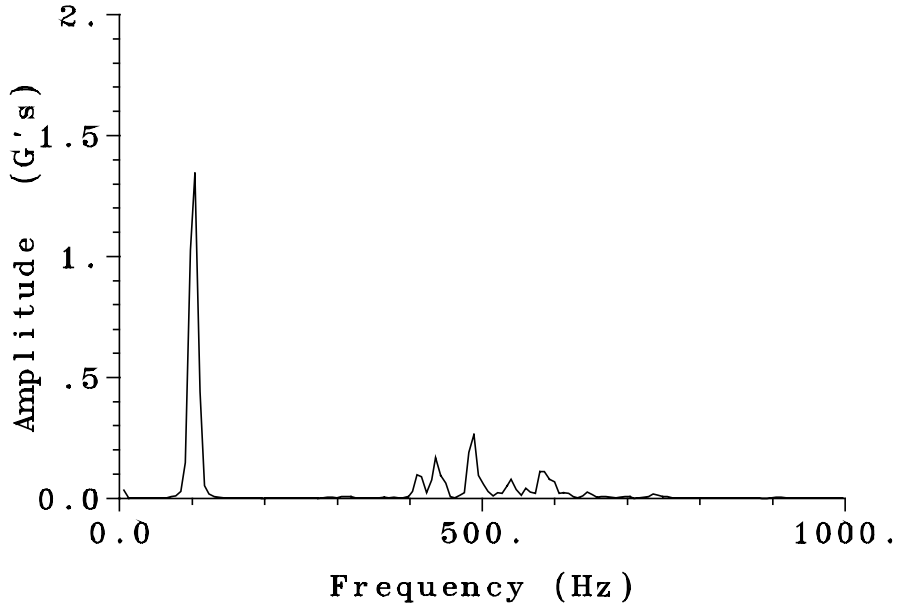

Fig. 78. Predicted torsion test frequencies for locked truss in 0° truss orientation.

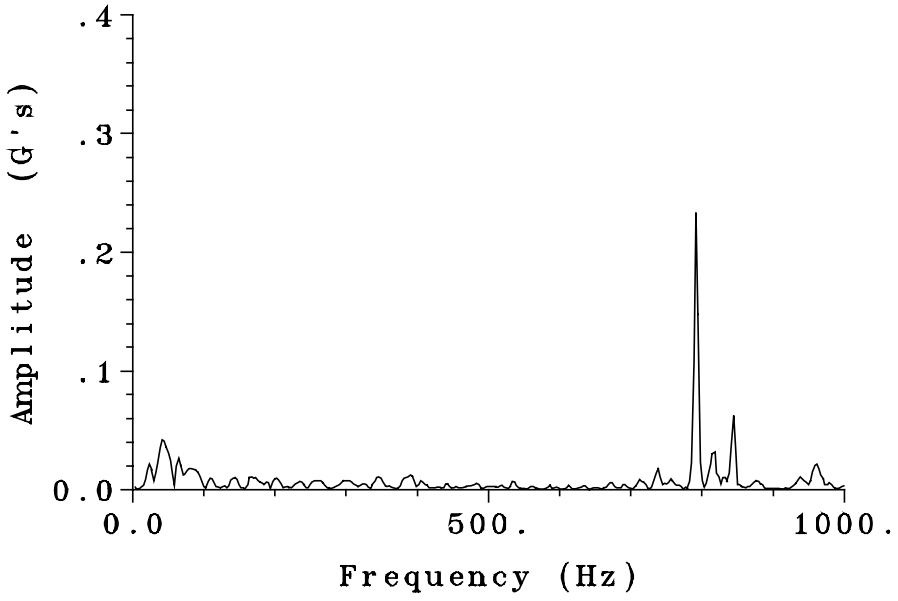

Fig. 79. Measured torsion test frequencies for unlocked truss in micro gravity.

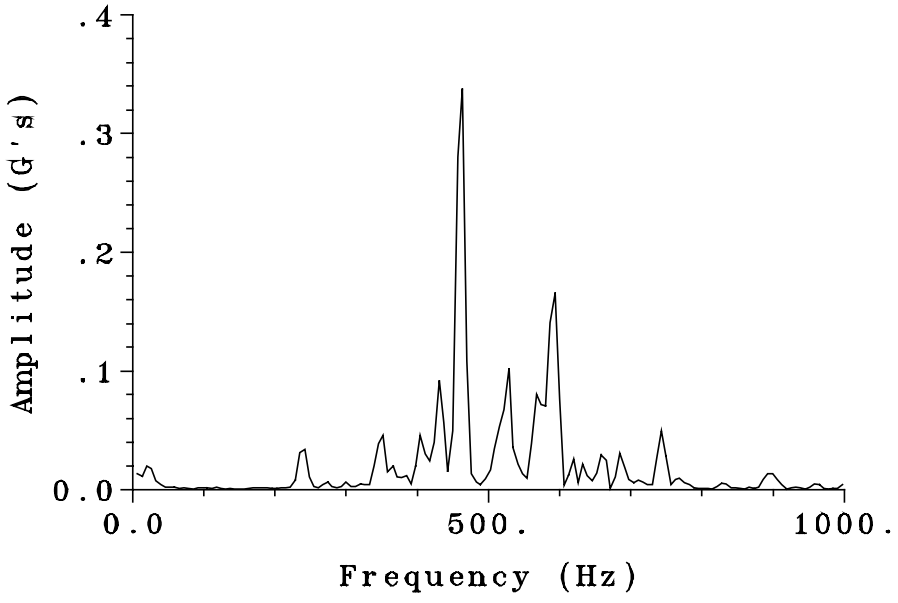

Fig. 80. Predicted torsion test frequencies for unlocked truss in micro gravity.

10.0 CONCLUSIONS

The Joint Damping Experiment successfully developed, characterized, and extended modeling capabilities of a truss which exhibits gravity dependent damping. The construction and important dimensional parameters of the JDX truss have been covered in detail. Joints in the truss are described as either "locked" or "unlocked" joints. Locked joints were assembled with interference fit pins and possess a linear force-displacement relationship. Unlocked joints use clearance fit pins in the clevis/tang assembly and have a small amount of deadband or slop in the force displacement relationship. The sizes of the final pin set selected for use in the unlocked joints in the truss were determined by a series of twang tests using different-sized pins. A series of tests was also conducted with all the truss joints locked. It was noted that the introduction of only eight unlocked joints into a truss has a significant effect on truss dynamic behavior. The final pins selected provided a diametrical gap ranging from 0.00045 to 0.0008 inches. The joint gaps selected are sufficiently small to produce a truss that feels tight. The truss was carefully assembled such that assembly-induced preloads were minimized, and unlocked joints would be able to traverse their deadband regions.

When the final pin set was selected, another series of ground baseline twang tests was conducted. These twang tests were performed in three orientations with respect to the gravity vector: 0°, 90°, and 180°. Furthermore, twang tests were also performed on NASA's low-G aircraft. The data from the low-G aircraft tests was compared with the ground tests to measure the influence of gravity on the dynamic characteristics of the truss. Damping in the truss was inferred from the logarithmic decrement of the decay. To show how the damping varies with oscillation amplitude, the logarithmic decrement was computed for each cycle and plotted as a function of the average amplitude. By comparing logarithmic decrement plots from the different test conditions, it was shown that gravity has a profound effect on the dynamic characteristics of the truss. A very consistent trend showed that as gravity loads decrease, damping increases. The 0° tests take longer to experience total vibrational decay than the low-G twang tests. Furthermore, the tests taken in the 90° orientation take longer to decay than the 0° tests.

Whenever the unlocked joints could traverse the deadband region, the decay showed significant content of high frequency hash or high frequency modes in the truss. These high frequency modes appear to be caused by impacting in the joints. Impacting in the joints as it moves through the deadband is thought to be a major contributor to the damping in the truss. Therefore, it is concluded that gravity preloads in the 0° and 90° truss orientations tend to prohibit the movement of the joint through the deadband. In the case of the 0° truss orientation, the gravity-induced preloads are small and therefore the joint is only inhibited at small amplitudes. The 90° truss orientation produces the largest gravity-induced preloads in the truss, and the movement of the joint through the deadband is inhibited at an acceleration amplitude of less than approximately one G. When the joints are prevented from traversing the deadband region by high gravity-induced preloads, the decay resembles that from a truss with all joints locked. The twang

tests recorded in the 180° orientation are very similar to the 0° twang tests. This is expected since the direction of the gravity vector with respect to the truss is simply reversed, and gravity-induced preloads are similar.

Twang tests taken in a cold cell showed that temperature has no significant effects on the truss until it falls to -20° C. Therefore, even if the experiment did experience greater than predicted temperature decreases, the data collected should still be valid.

Torsion mode twang tests were significantly influenced by joint preloads. The torsion mode would disappear when joint preloads became small. When all the joints in the truss were locked, the 110 Hz. torsion mode predicted by a linear finite element model of the truss was observed. However, when eight unlocked joints are present in the truss and gravity preloads are small, the 110 Hz. torsion mode disappears and an 800 Hz. mode was present instead. In the 90° truss orientation tests, the joints have high preloads and the 110 Hz. torsion mode is easily observed. Tests in the low-G aircraft and in different orientations with respect to the gravity vector indicated that as joint preloads are reduced, the expected torsion mode disappears. Exact causes for this phenomenon are still under investigation. However, it is very significant that a fundamental mode predicted by a linear finite element model of the truss would disappear.

The experiment was launched into low earth orbit aboard the Space Shuttle Endeavor on September 7, 1995. The experiment successfully executed thirty twang tests, ten in each of the three modes. During integration it was found that the experiment was exciting modes in the GAS bridge assembly it was mounted on. An effort was made to determine the extent of the coupling the experiment would experience in the Space Shuttle cargo bay using a linear finite element model of the GAS bridge. This model correctly predicted that the flight tests would have less coupling than the integration tests. Fortunately, the data from the space flight showed very little coupling between the experiment and the GAS bridge in the bend one mode and light coupling with the bend two mode. Furthermore, the data from the space flight were very similar to the low-G tests, thus confirming the validity of the low-G tests.

Post flight tests showed that the dynamic properties of the truss can change. The observed increase in damping is consistent with an increase in joint gap. Although the pins used in the joints had marks that were indicative of wear, micrometer readings did not indicate any measurable wear. Thus, one should expect some drift in the dynamic properties of a truss using pinned joints over time.

A force-state mapping technique has been used to successfully obtain a base of experimental information regarding the axial behavior of struts with pinned joints. This data is useful for the development of finite element models of struts in a test bed. At this time it is assumed that the boundary conditions in the test bed are similar to those in the truss. For surface fits with simple terms, the fit is deemed not useful unless is can apply different terms in different zones. A better approach has been shown to be the determination of nominal parameters from the data with

subsequent adjustment until the finite element model and data match on displacement-time history plots.

A finite element model of a single strut with a pinned joint was constructed in LS-DYNA3D. The model included extensional and rotational friction, equivalent viscous damping, and impacting in the joint. The results of force-state mapping tests were used to determine appropriate parameters for the finite element model. The single strut model was extended to model the pin-jointed truss structure. The truss model results correlated well with measured data from tests conducted in a micro gravity environment; however, the model did not predict as well the truss behavior when gravity caused strut preloads. The finite element model predicts that impacting in the pinned-joints excites higher frequency modes in the truss, thereby increasing structural damping. Much work remains to be done to determine the effect of each joint parameter on the overall structural damping of pin-jointed structures. Nevertheless, the ability to predict many of the observed behaviors has been demonstrated. Additionally, a procedure for estimating model parameters such as joint deadband, friction, and equivalent viscous damping from tests characterizing individual joints has been demonstrated.

10.1 Recommendations for Future Work

It is recommended that additional work be completed in this area. The following are recommended as areas which should be investigated:

1. Additional testing with JDX would provided needed data to further critique models of a pin jointed truss. Additional data from ground tests and the low-G aircraft tests are needed to examine the effects of:

- A range of pin sizes in the unlocked joints.
- Dry friction in the joint obtained by removing the lubricant around the pins and testing them dry.

2. The LS-DYNA3D model shows great promise for being able to model the dynamic behavior of structures with loose connections. However, a customized element(s) should be developed which specifically models loose connections. This could make modeling much easier and could improve the accuracy of the model.

11.0 REFERENCES

1. Nurre, G. S., "Dynamics and Control of Large Space Structures," *Journal of Guidance, Control, and Dynamics*, Vol. 7, No. 5, 1984, p. 514.

2. Den Hartog, J. P., *Mechanical Vibrations*, 4th ed., McGraw-Hill, New York, 1956.

3. Plunkett, R., "Friction Damping," *Damping Applications for Vibration Control*, edited by P. J. Torvik, American Society of Mechanical Engineers, New York, 1980, pp. 65-74.

4. Crawley, E. F., Sigler, J. L., and van Schoor, M. C., "Prediction and Measurement of Damping in Hybrid Scaled Space Structure Models," Space Systems Laboratory, Dept. of Aeronautics and Astronautics, MIT, Report SSL 7-88, Cambridge, MA, July 1988.

5. Folkman, S. L., and Redd, F. J., "Gravity Effects on Damping of a Space Structure with Pinned Joints." AIAA Journal of Guidance, Control, and Dynamics, Vol. 13, No. 2, 1990, pp. 228-233.

6. Ferri, A. A., "Modeling and Analysis of Nonlinear Sleeve Joints of Large Space Structures," *AIAA Journal of Spacecraft and Rockets*, Vol. 25, No. 5, 1988, pp. 354-365.

7. Lankarani, H. M., and Nikravesh P. E., "A Contact Force Model With Hysteresis Damping for Impact Analysis of Multibody Systems," *Journal of Mechanical Design*, Vol. 112, Sept. 1990, pp. 369-376.

8. Tzou, H. S. and Rong, Y., "Contact Dynamics of a Spherical Joint and a Jointed Truss-Cell System," *AIAA Journal*, Vol. 29, No. 1, Jan. 1991, pp. 81-88.

9. Onoda, J., Sano, T., and Minesugi, K., "Passive Vibration Suppression of Truss by Using Backlash," Proceedings of the 34th AIAA/ASME/ASCE/AHS/ASC Structures, Structural Dynamics, and Materials Conference (LaJolla, CA); also AIAA Paper 93-1549.

10. Folkman, S. L., "Measurement and Modeling of Joint Damping in Large Space Structures," Ph.D. Dissertation, Utah State Univ., Logan, UT, 1990.

11. Crawley, E. F., and Aubert, A. C., "Identification of Nonlinear Structural Elements by Force-State Mapping," AIAA Journal, Vol. 24, 1986, pp. 155-162.

12. Crawley, E. F., and O'Donnell, K. J., "Force-State Mapping Identification of Nonlinear Joints," AIAA Journal, Vol. 25, 1987, pp. 1003-1010.

13. Masters, B. P., Crawley, E. F., and van Schoor, M. C., "Global Structure Modeling Using Force-State Component Identification," Proceedings of the 35th AIAA/ASME/ASCE/AHS/ASC Structures, Structural Dynamics and Materials Conference (Hilton Head, SC); also AIAA Paper 94-1519.

14. MSC/NASTRAN Handbook for Nonlinear Analysis, MacNeal Schwendler Corporation, Los Angeles, CA, 1992.

15. *MSC/NASTRAN Release Notes for Version 68*, MacNeal Schwendler Corporation, Los Angeles, CA, 1994.

16. *LS-DYNA3D User's Manual*, Livermore Software Technology Corporation, Livermore, CA, 1995.

17. *LS-DYNA3D Theoretical Manual*, Livermore Software Technology Corporation, Livermore, CA, 1995.

18. The GAS Team, "Get Away Special (GAS) Small Self-Contained Payloads Experimenter Handbook," Goddard Space Flight Center, 1995.

Masters Thesis Completed under JDX

1. Strong, S. D., "A Prototype Experiment to Measure Gravity Effects on Joint Damping in a Space Structure Model," M.S. Thesis, Utah State Univ., Logan, UT, 1990.
2. Wheelwright, P. D., "Preferential Excitation of a Torsion Vibration Mode in a Prototype Space Structure," M.S. Thesis, Utah State Univ., Logan, UT, 1992.
3. Ferney, G. D., "Development of a Method for Characterizing Joint Stiffness and Hysteresis," M.S. Thesis, Utah State Univ., Logan, UT, 1993.
4. Rowsell, E. A., "Development of the Engineering Model Truss for the Joint Damping Experiment," M.S. Thesis, Utah State Univ., Logan, UT, 1994.
5. Ferney, B. D., "Development of a Technique for Joint Characterization Using Force-State Mapping," M.S. Thesis, Utah State Univ., Logan, UT, 1995.
6. Dutson, J. D., "Analytical Computer Model of the JDX Truss," M.S. Thesis, Utah State Univ., Logan, UT, 1996.
7. Bingham, J. G., "Design and Test Results form the Joint Damping Experiment Flight Model Truss," M.S. Thesis, Utah State Univ., Logan, UT, 1996.
8. Crookston, J. R., "A Nonlinear Finite Element Computer Model of the JDX Truss," M.S. Thesis, Utah State Univ., Logan, UT, 1996 (anticipated date).

APPENDICES

APPENDIX A - DRAWINGS OF THE JDX FLIGHT MODEL TRUSS

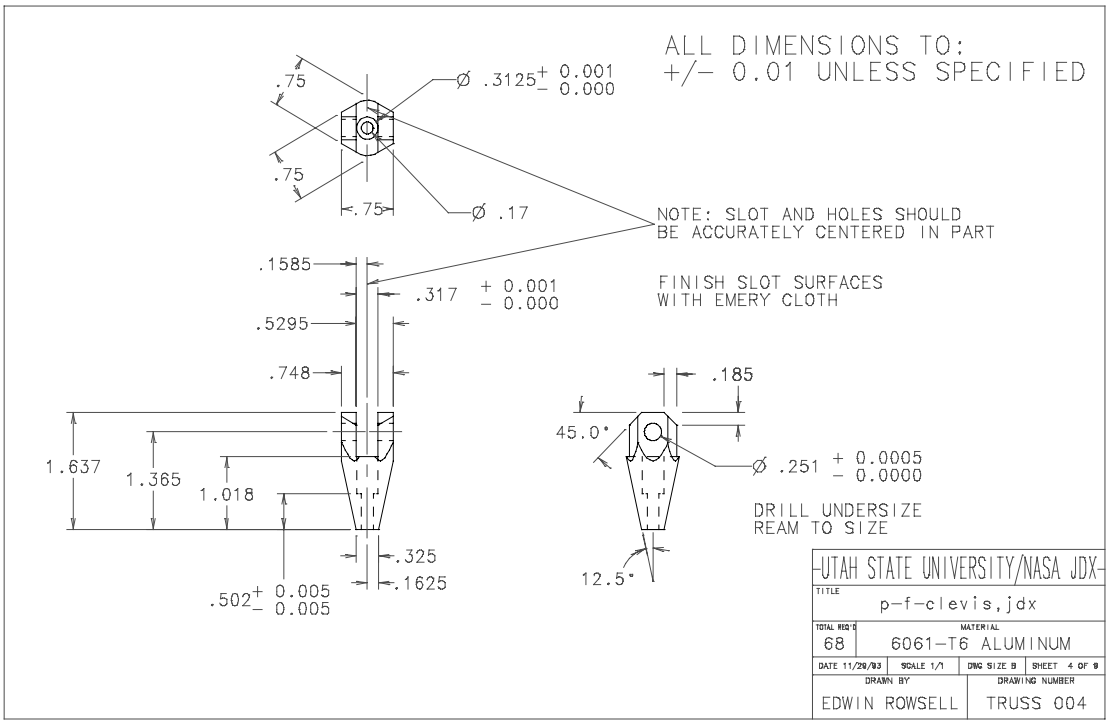

Fig. 81. JDX clevis design.

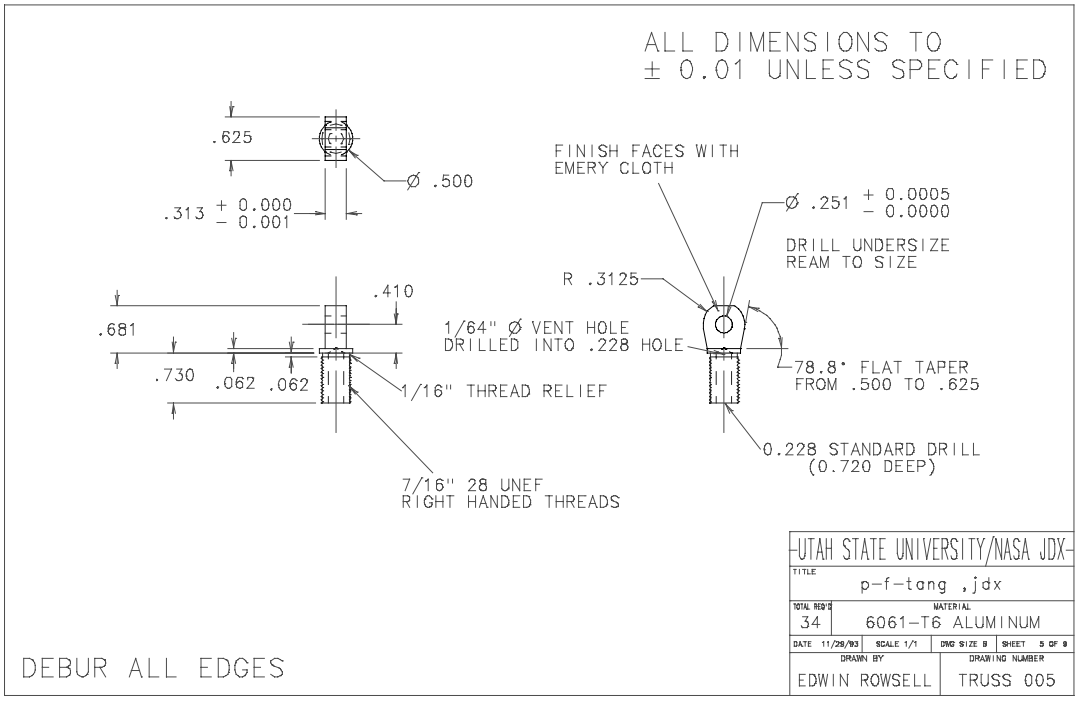

Fig. 82. JDX tang design.

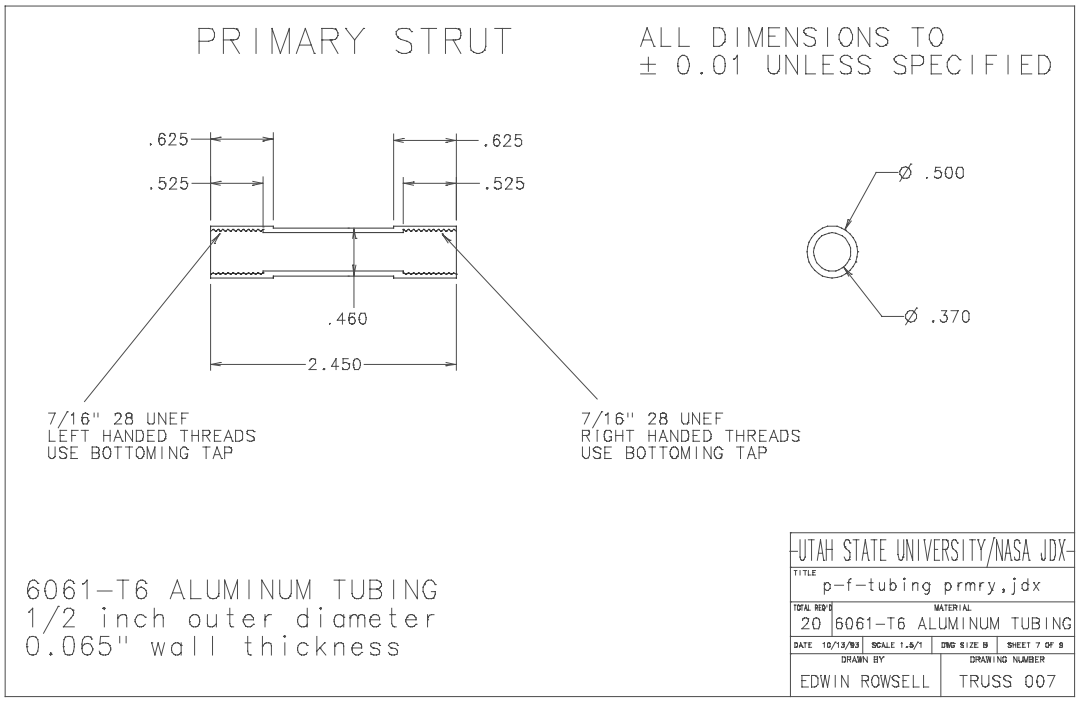

Fig. 83. JDX short tube design.

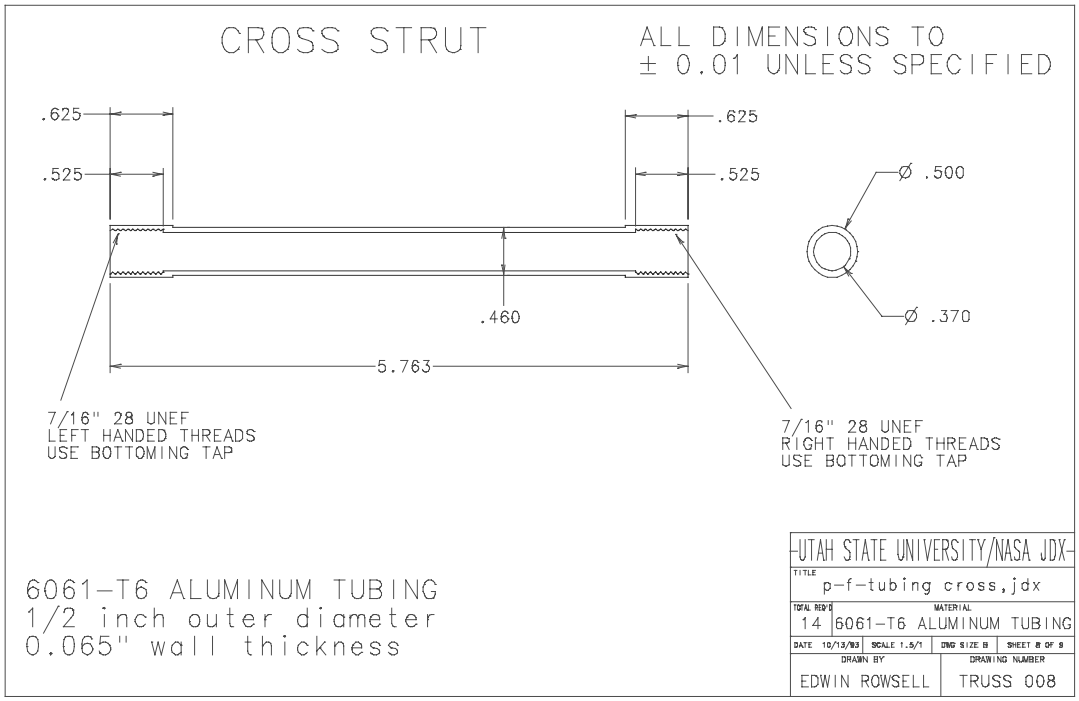

Fig. 84. JDX long tube design

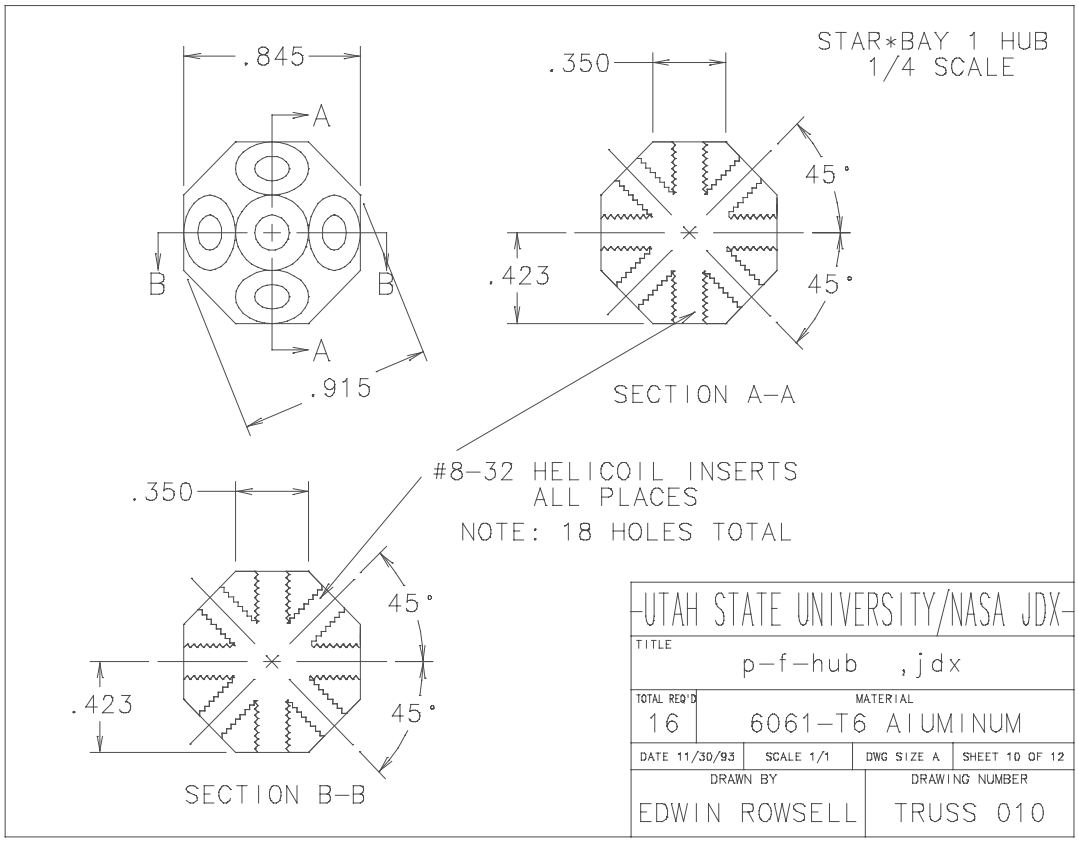

Fig. 85. JDX hub design.

APPENDIX B - ELECTRICAL DIAGRAM FOR JDX

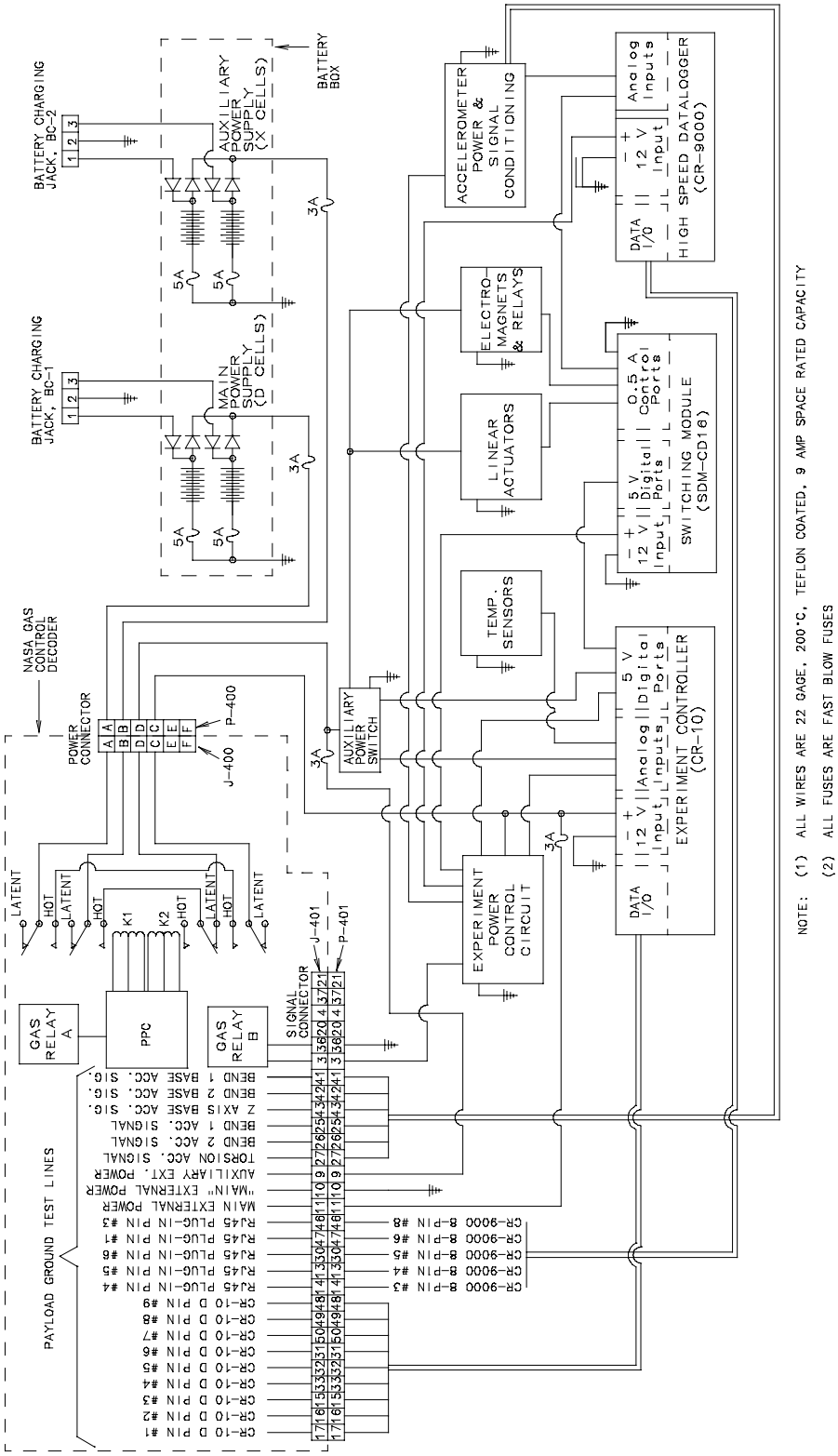

Fig. 86. Summary of the electrical circuits for JDX.

APPENDIX C - JDX FLIGHT MODEL TRUSS TWANG TESTS

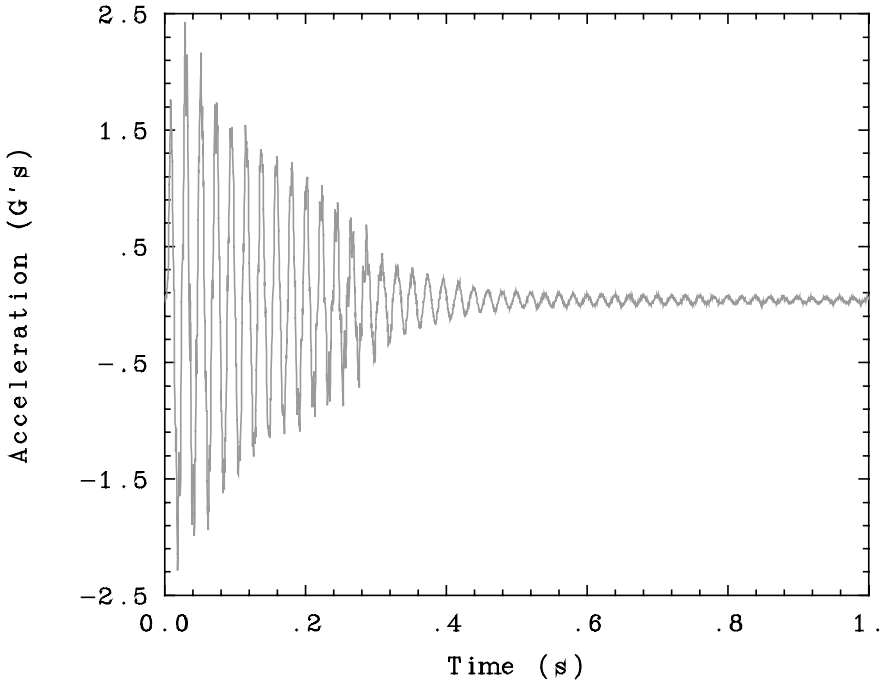

Fig. 87. Bend 2 twang test using pin set one in the 0° truss orientation.

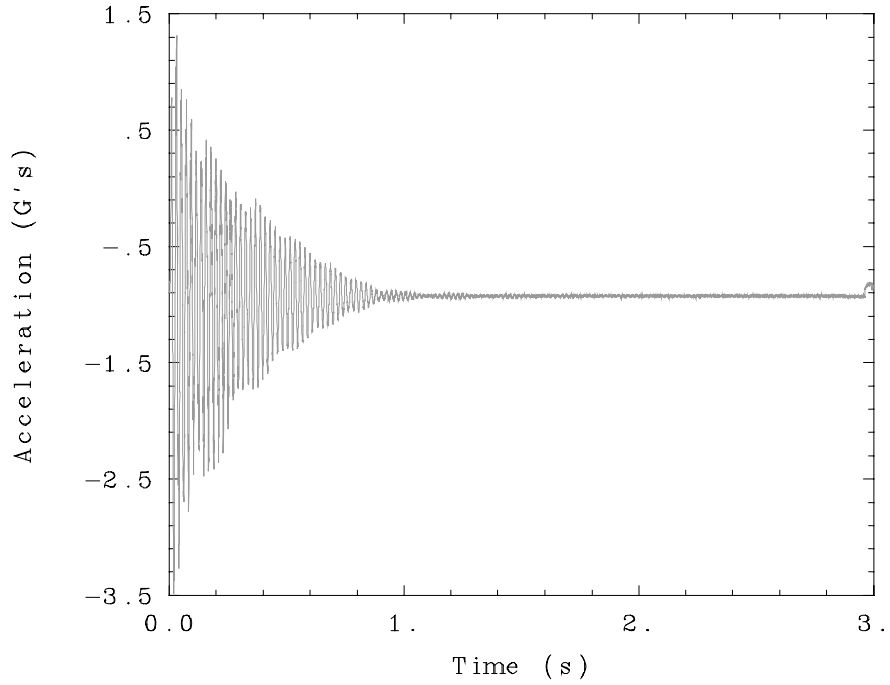

Fig. 88. Bend 2 twang test using pin set one in the 90° truss orientation.

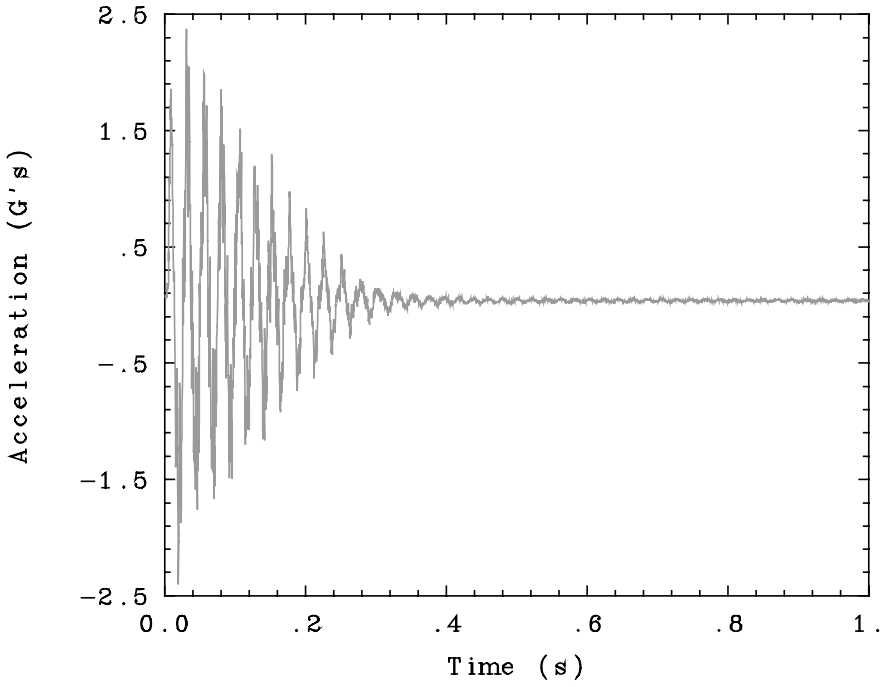

Fig. 89. Bend 2 twang test using pin set two in the 0° truss orientation.

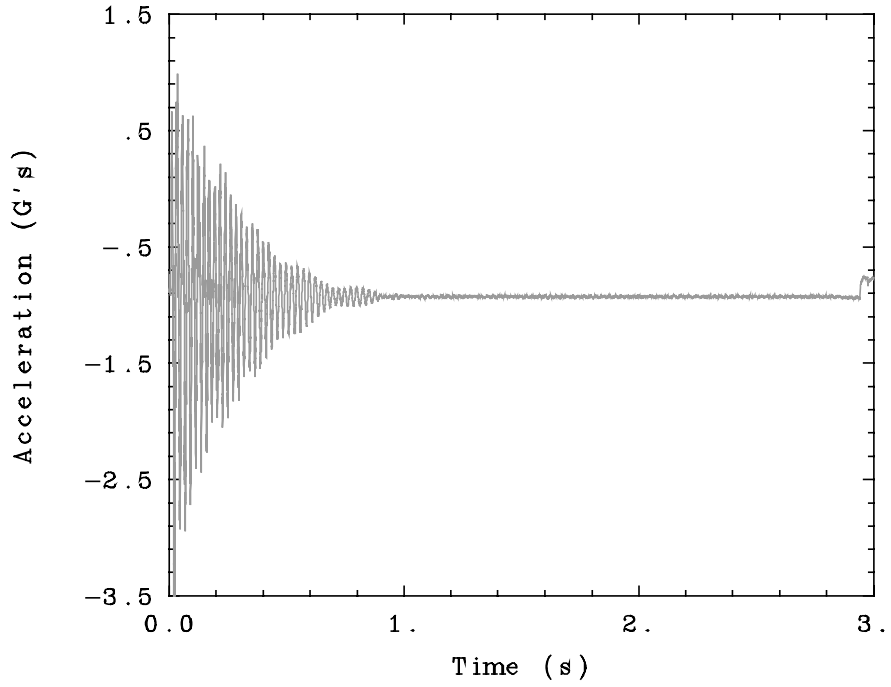

Fig. 90. Bend 2 twang test using pin set two in the 90° truss orientation.

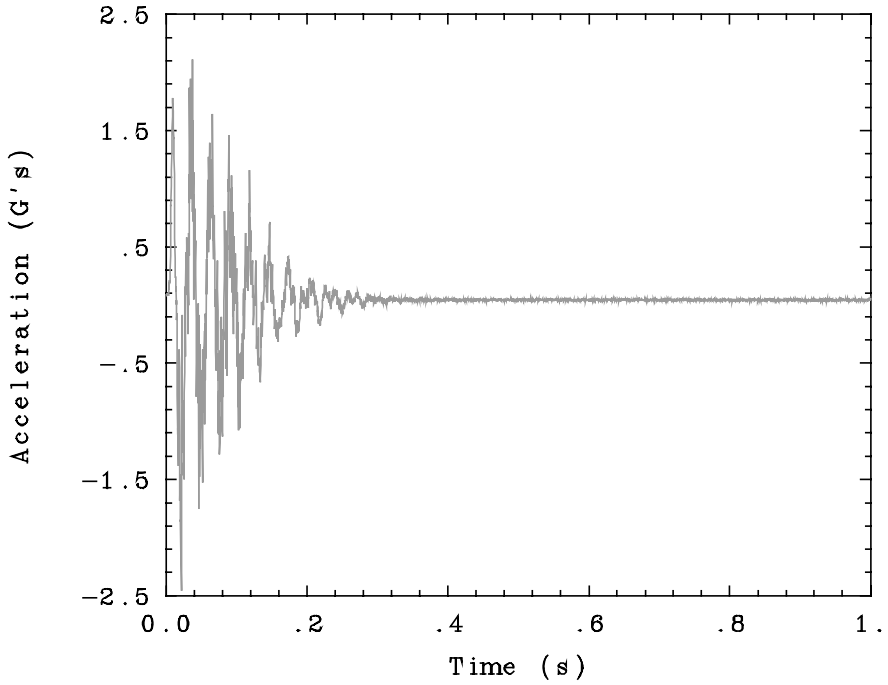

Fig. 91. Bend 2 twang test using pin set three in the 0° truss orientation.

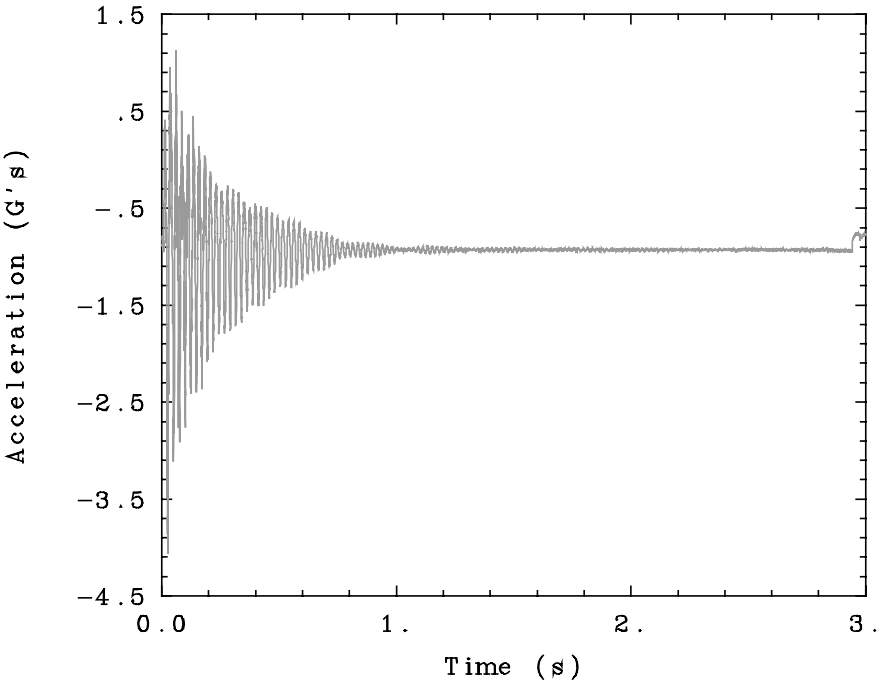

Fig. 92. Bend two twang test using pin set three in the 90° truss orientation.

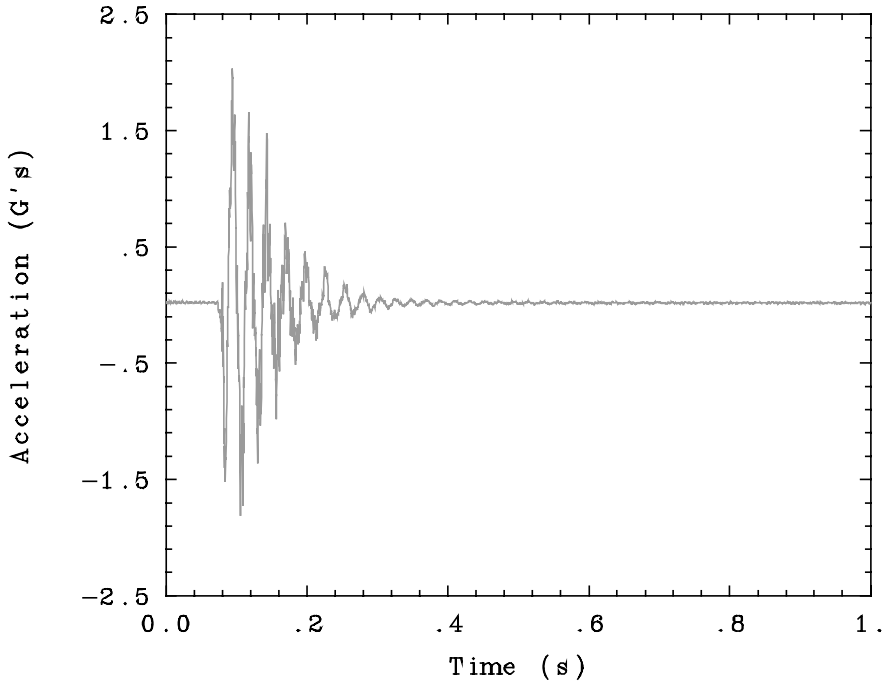

Fig. 93. Baseline bend 2 twang test in the 0° truss orientation.

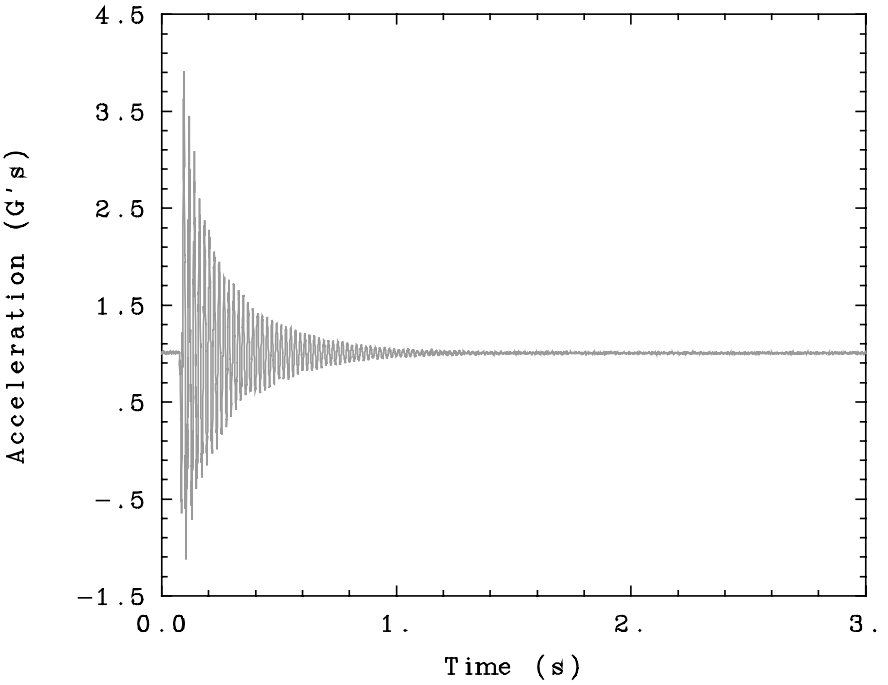

Fig. 94. Baseline bend 2 twang test in the 90° truss orientation.

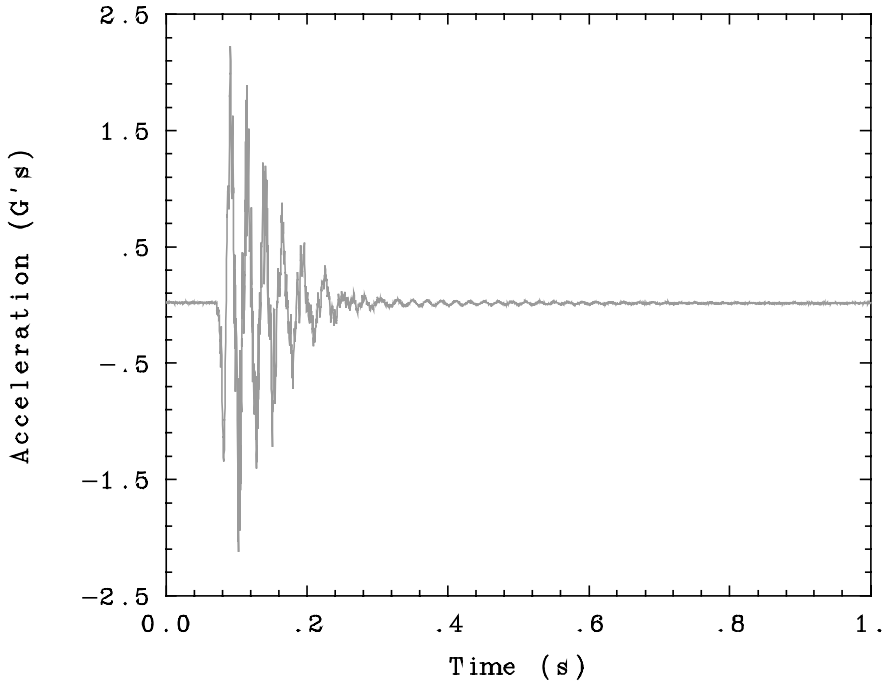

Fig. 95. Baseline bend 2 twang test in the 180° truss orientation.

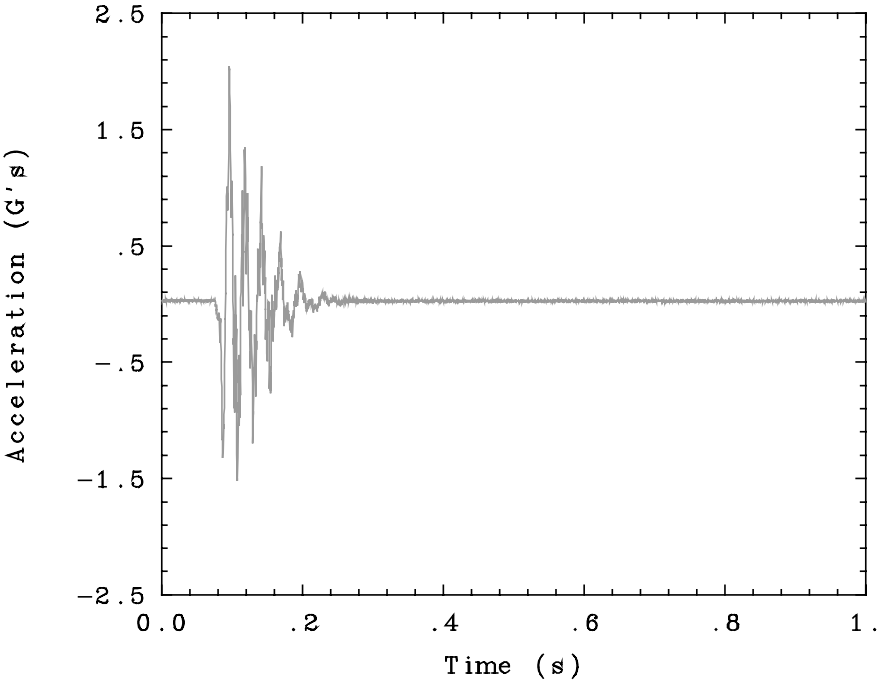

Fig. 96. Bend 2 twang test recorded during low-G flight.

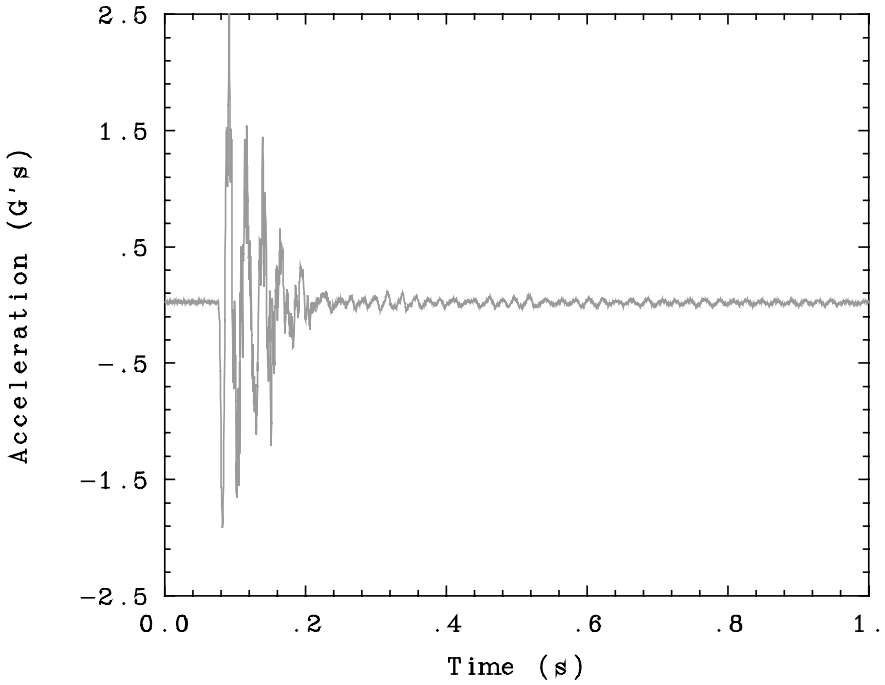

Fig. 97. Bend 2 twang test recorded on the GAS bridge during space shuttle integration.

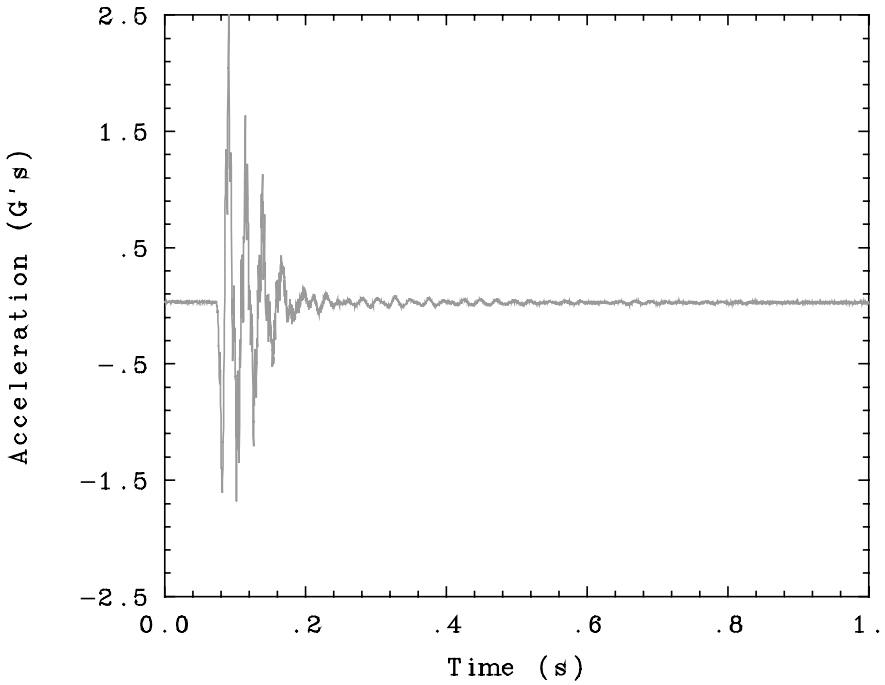

Fig. 98. Bend 2 twang test recorded during Space Shuttle flight.

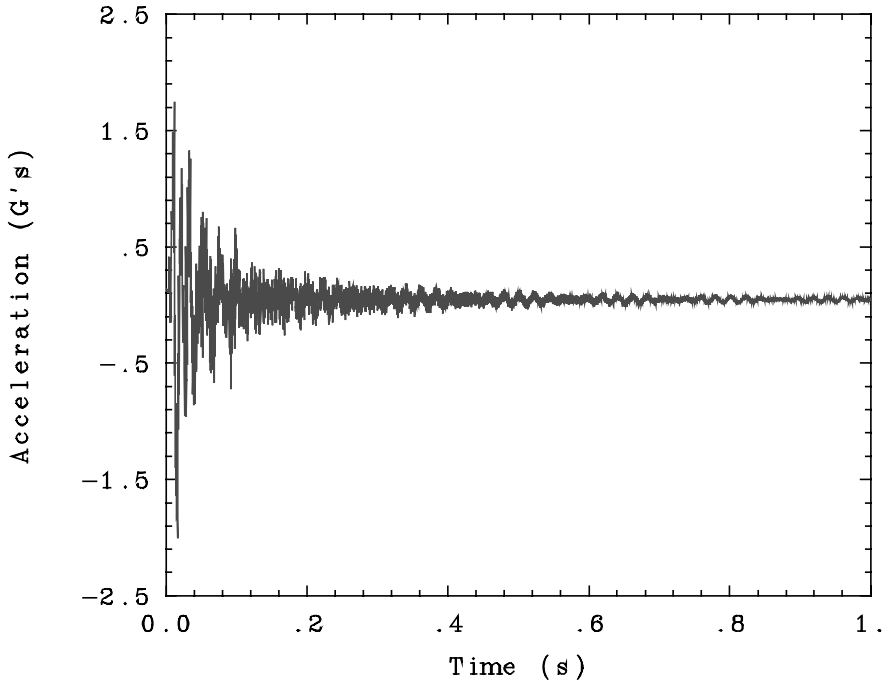

Fig. 99. Torsion test using pin set one in the 0° truss orientation.

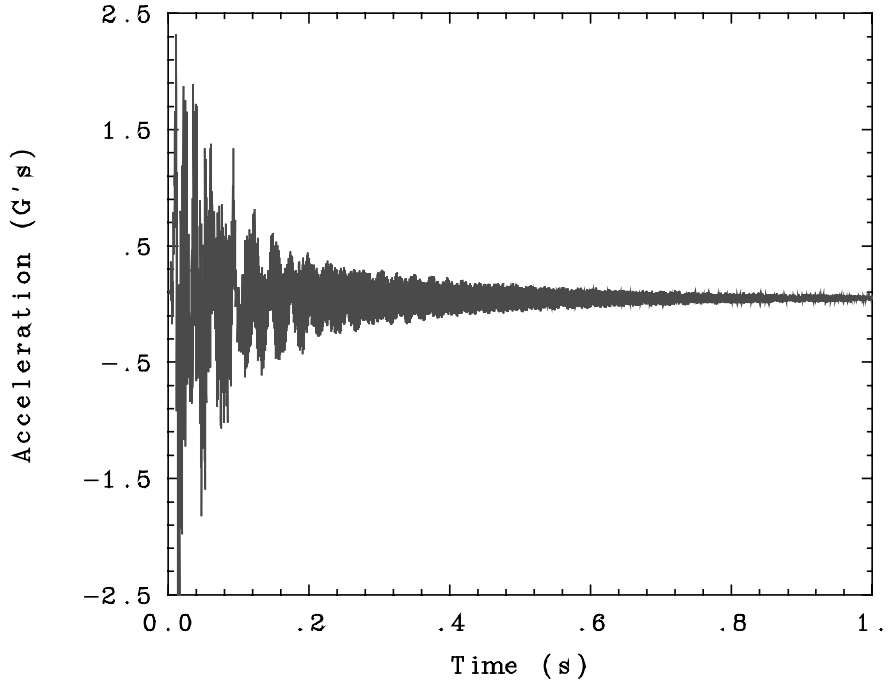

Fig. 100. Torsion twang test using pin set two in the 0° truss orientation.

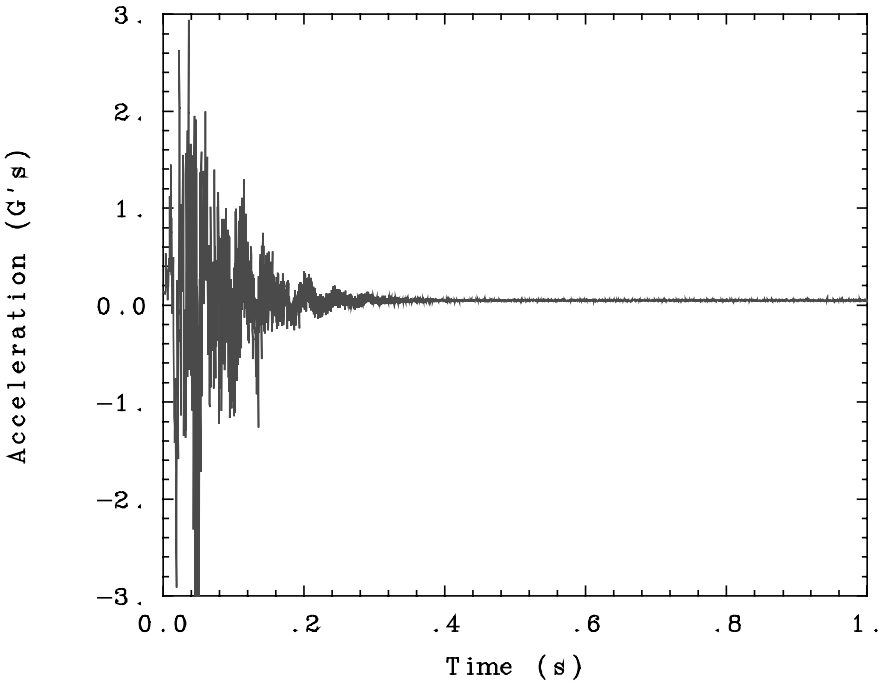

Fig. 101. Torsion twang test using pin set three in the 0° truss orientation.

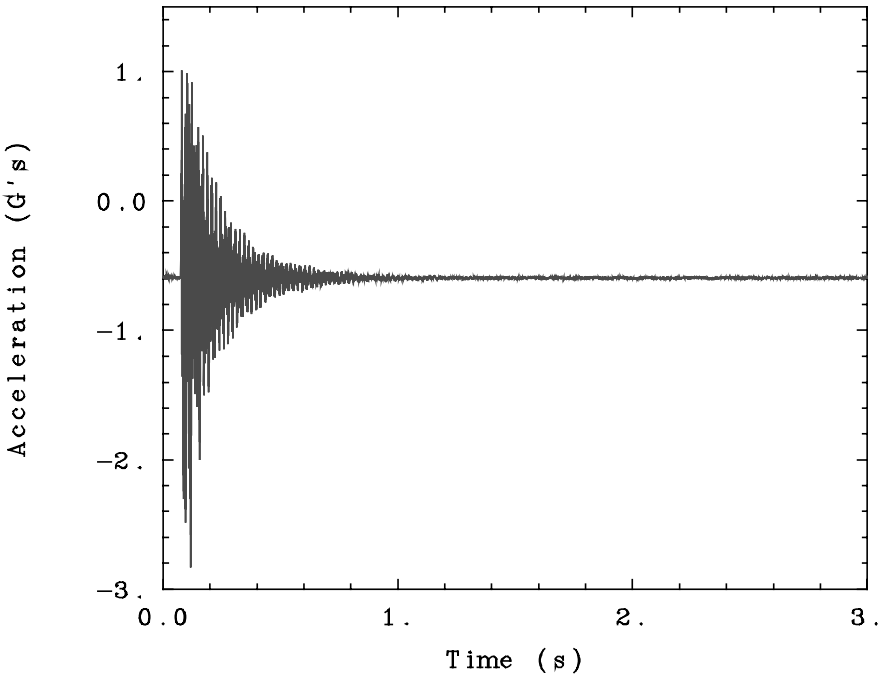

Fig. 102. Baseline torsion twang test in the 90° truss orientation.

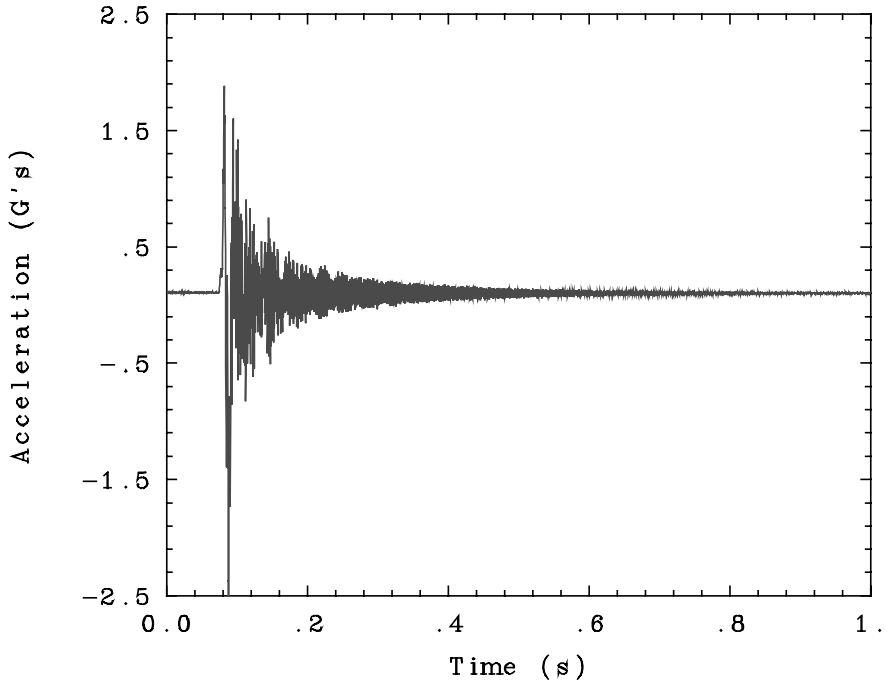

Fig. 103. Baseline torsion twang test in the 180° truss orientation.

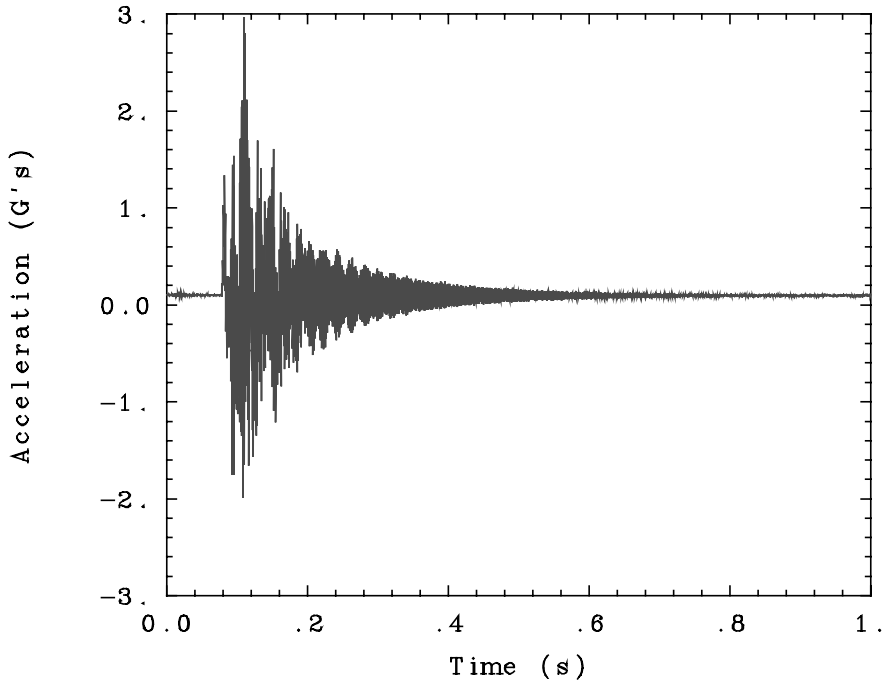

Fig. 104. Torsion twang test recorded during low-G testing.

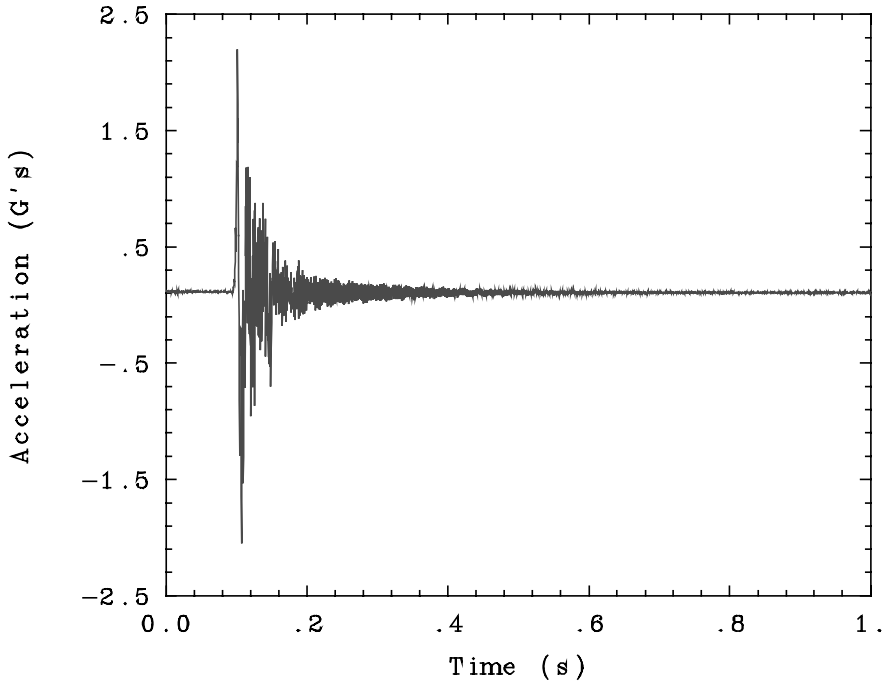

Fig. 105. Torsion twang test recorded on the GAS bridge during Space Shuttle integration.

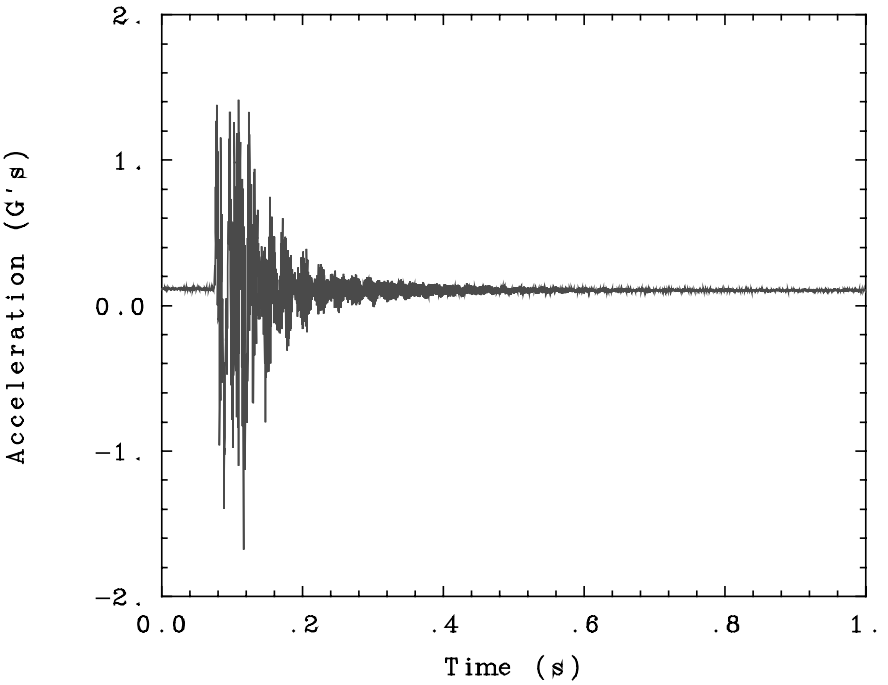

Fig. 106. Torsion twang test recorded during Space Shuttle flight.

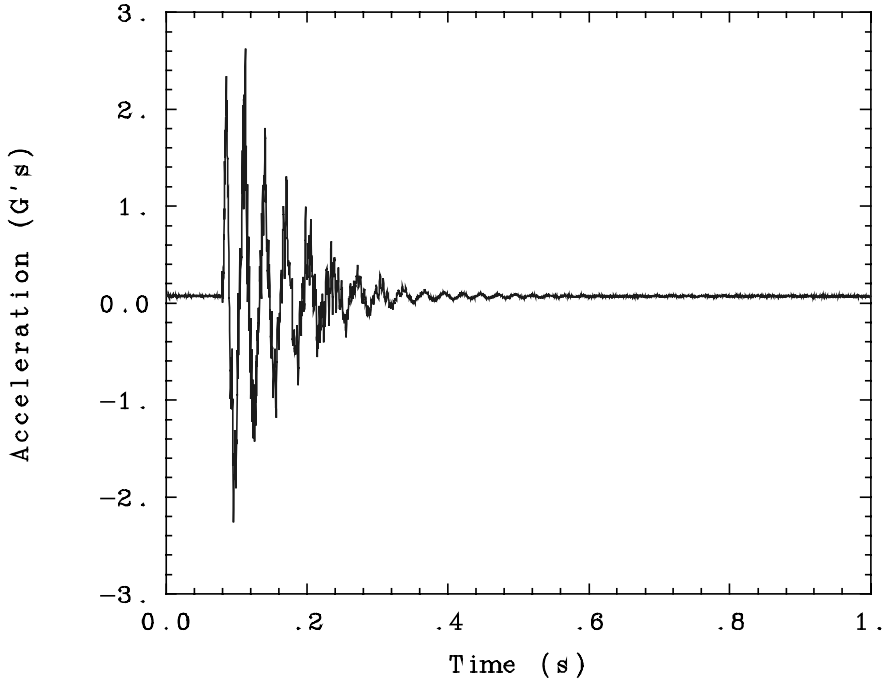

Fig. 107. Bend 1 twang test recorded during cold cell tests at 20° C.

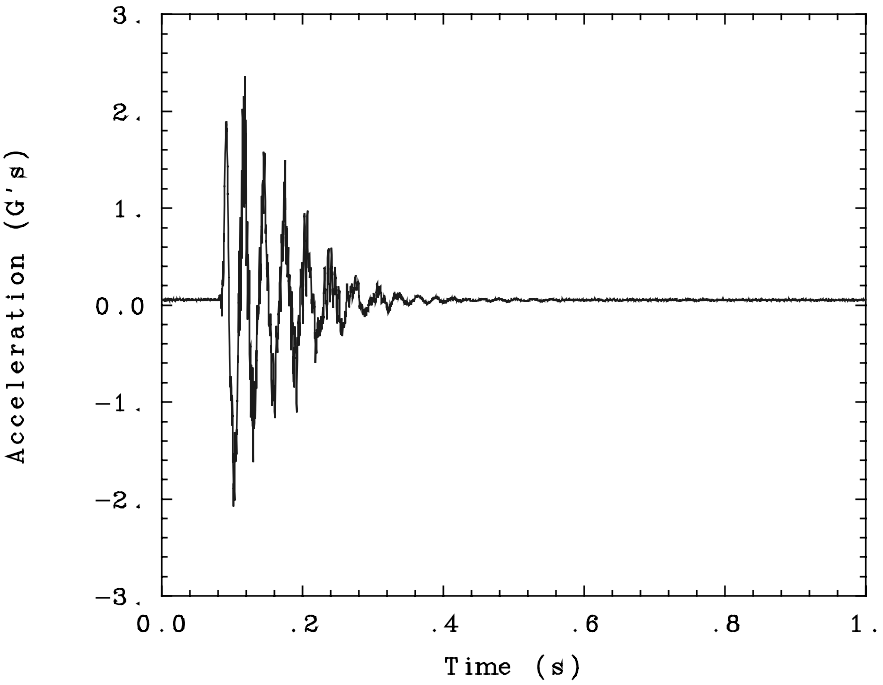

Fig. 108. Bend 1 twang test recorded during cold cell tests at 10° C.

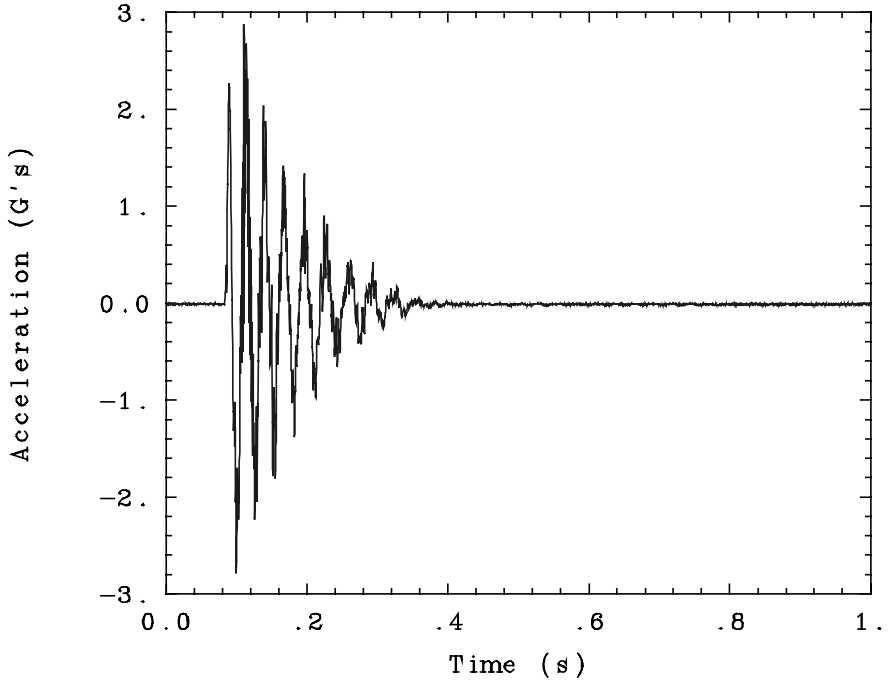

Fig. 109. Bend 1 twang test recorded during cold cell tests at 0° C.

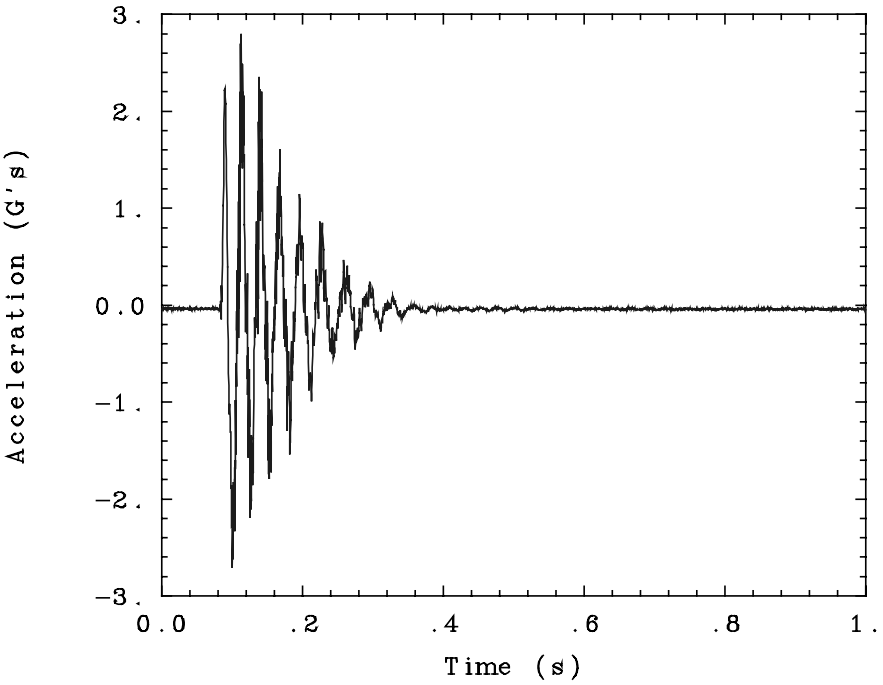

Fig. 110. Bend 1 twang test recorded during cold cell tests at -10° C.

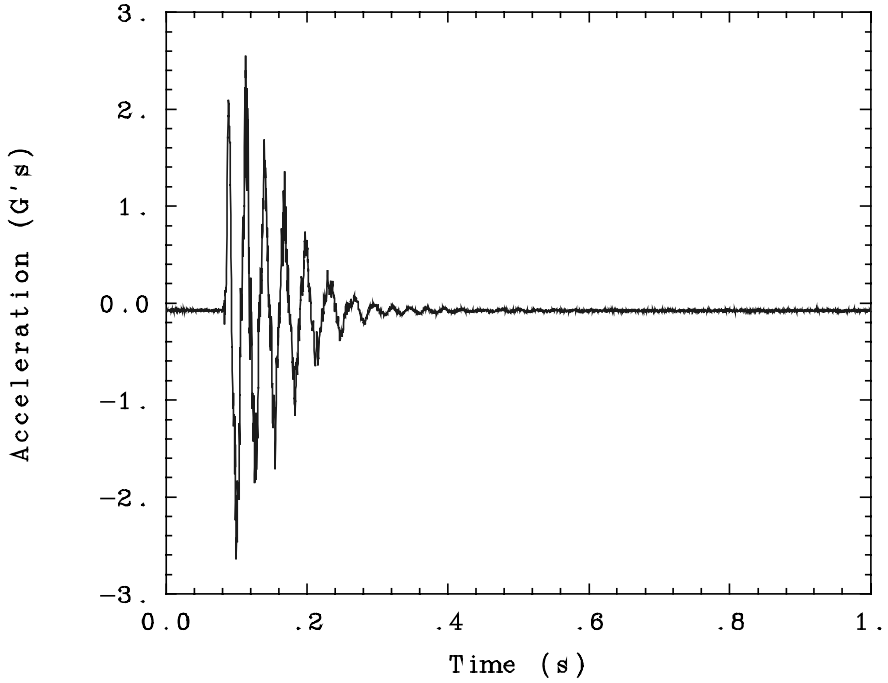

Fig. 111. Bend 1 twang test recorded during cold cell tests at -20° C.

APPENDIX D - LOGARITHMIC DECREMENT CURVES

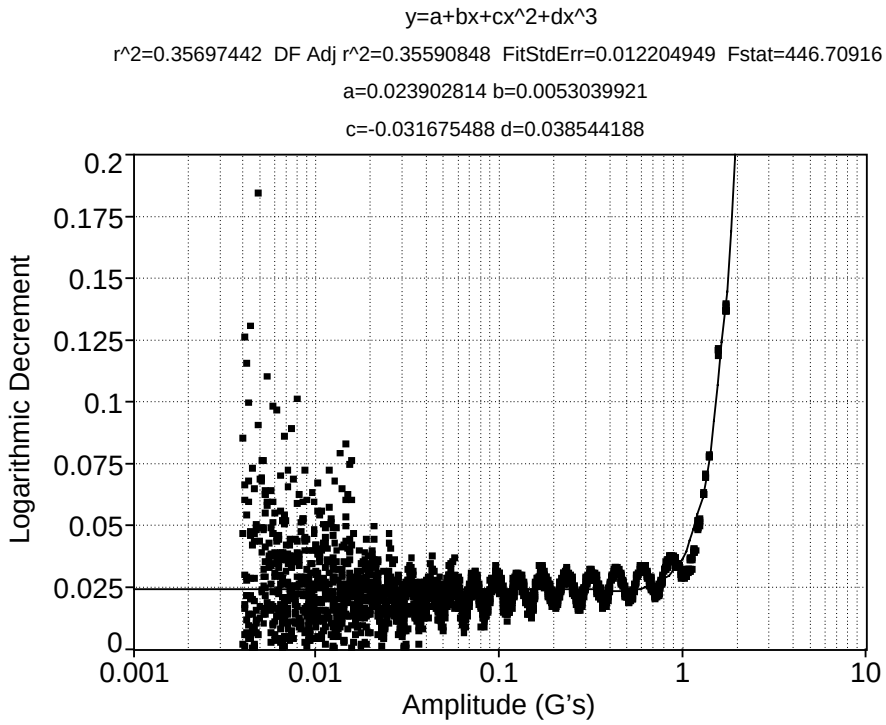

Fig. 112. Bend 1 test in the 0° truss orientation with all joints locked.

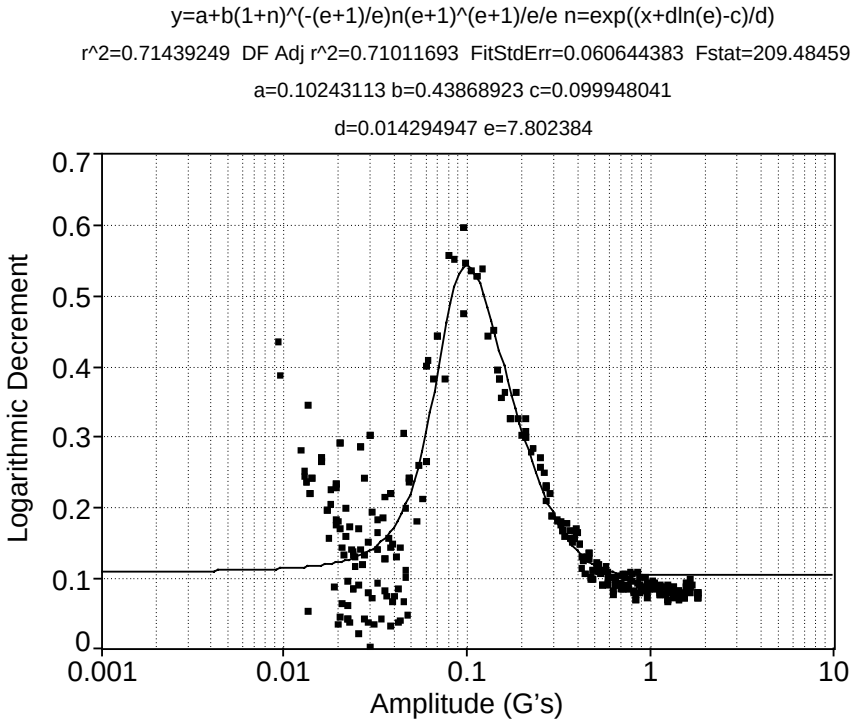

Fig. 113. Bend 1 test using pin set one in the 0° truss orientation.

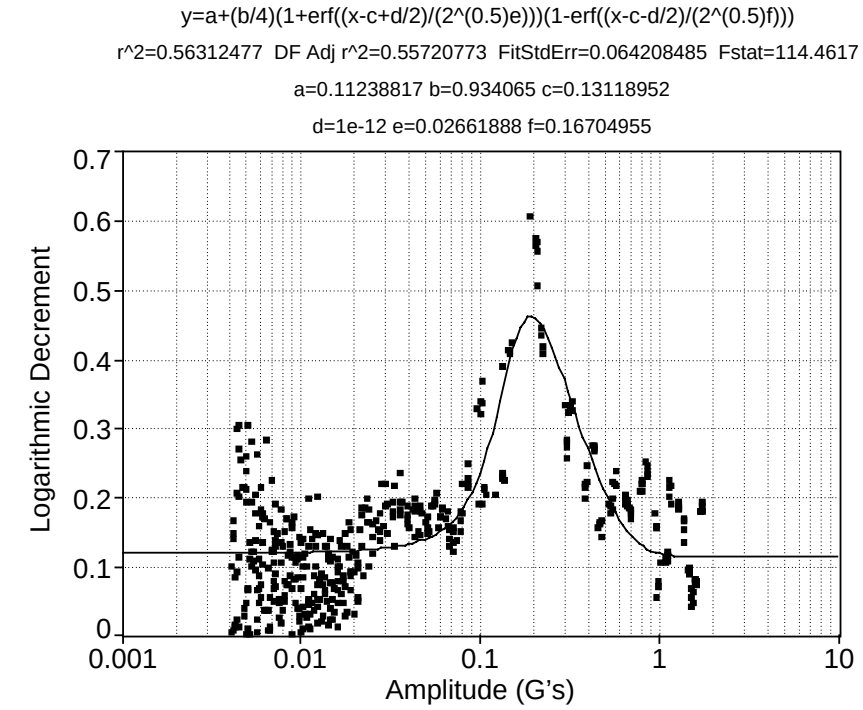

Fig. 114. Bend 1 test using pin set two in the 0° truss orientation.

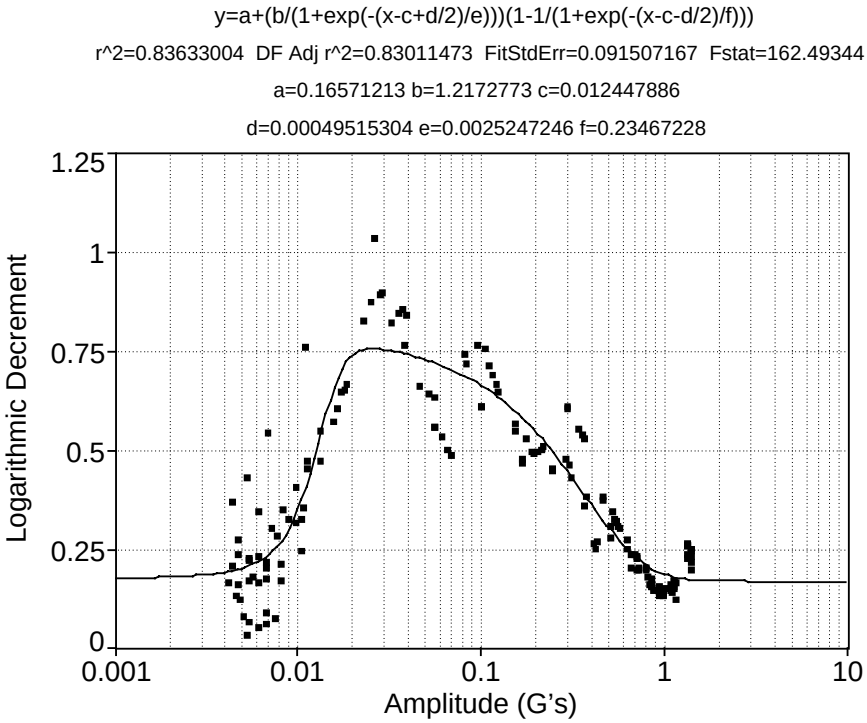

Fig. 115. Baseline bend 1 test in the 0° truss orientation.

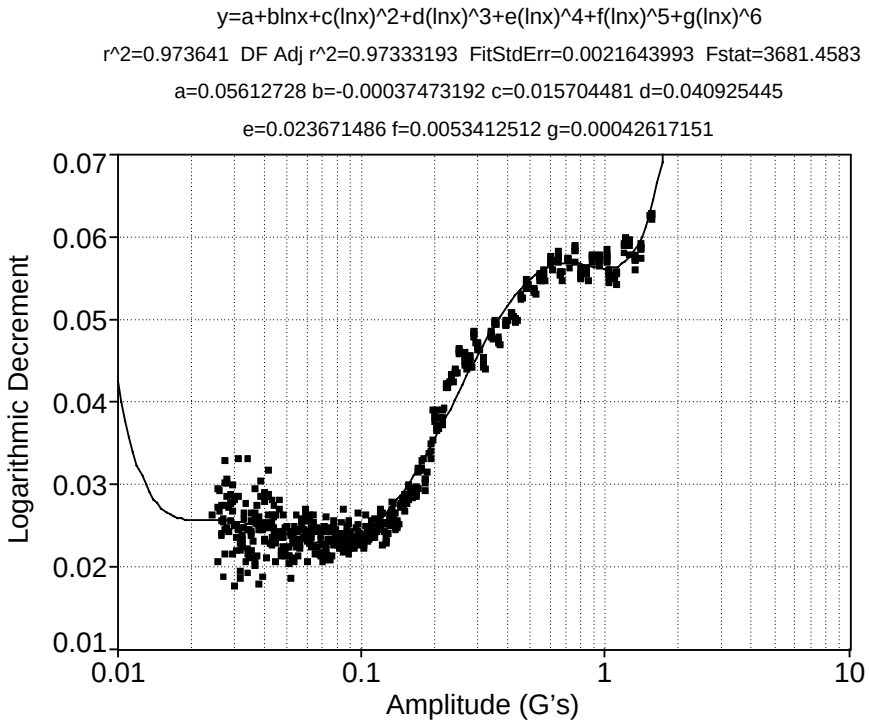

Fig. 116. Bend 1 test, upper peaks, in the 90° orientation using pin set one.

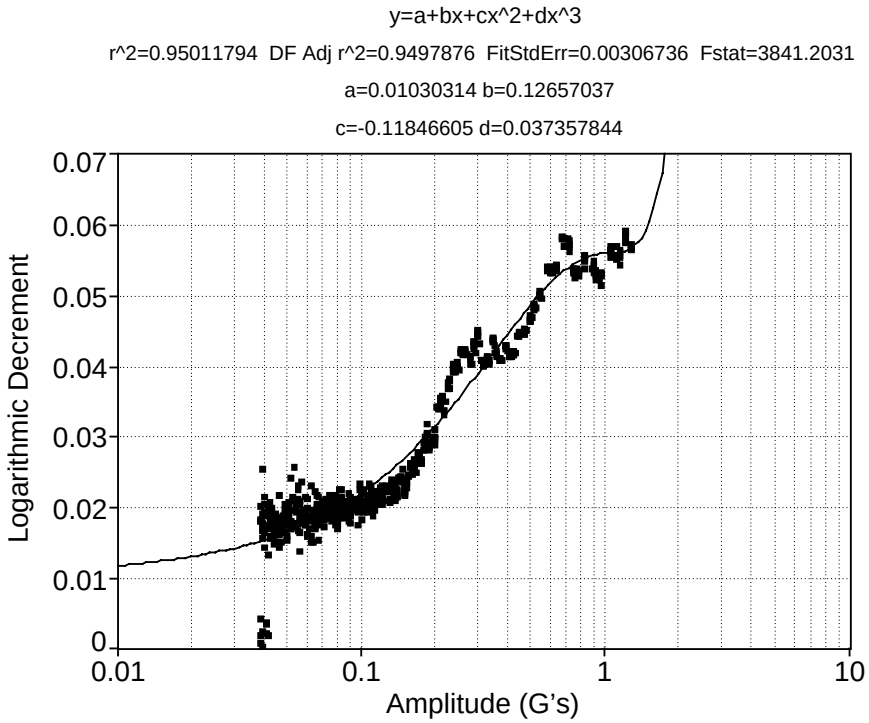

Fig. 117. Bend 1 test, lower peaks, in the 90° truss orientation using pin set one.

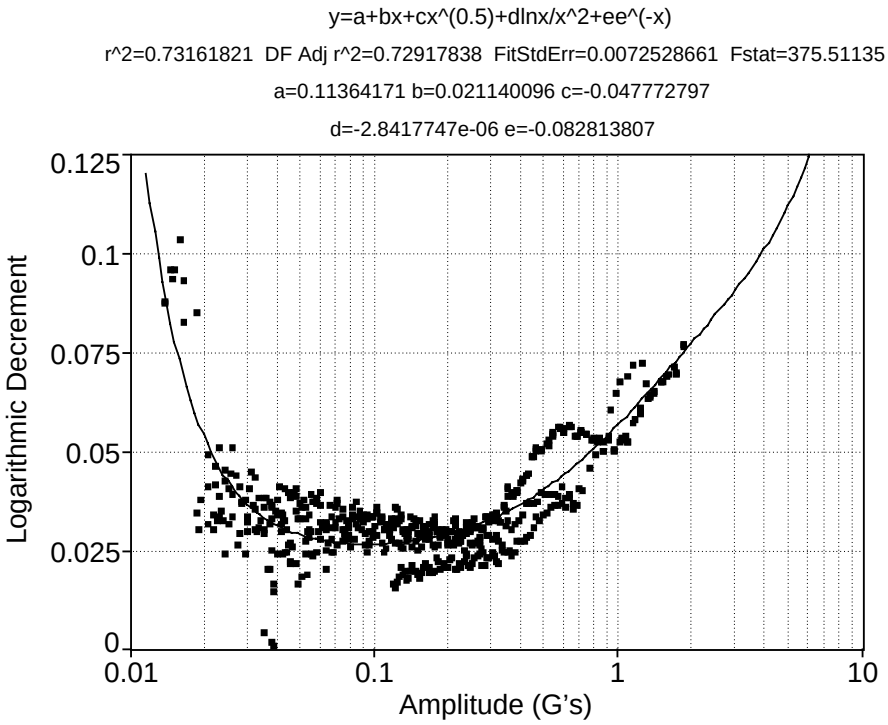

Fig. 118. Bend 1 test, upper peaks, in the 90° truss orientation using pin set two.

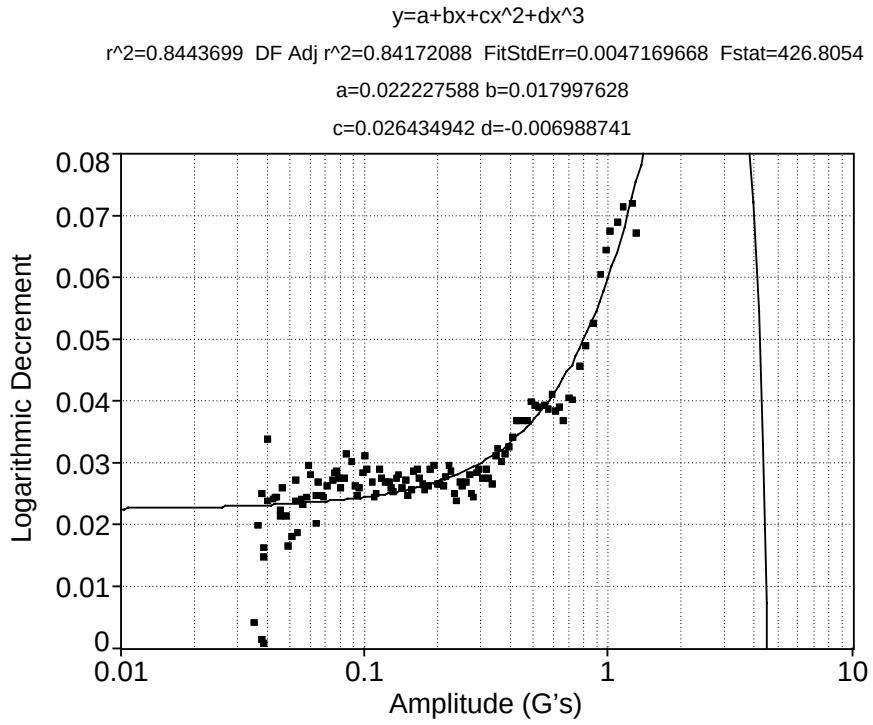

Fig. 119. Bend 1 test, lower peaks, in the 90° truss orientation using pin set two.

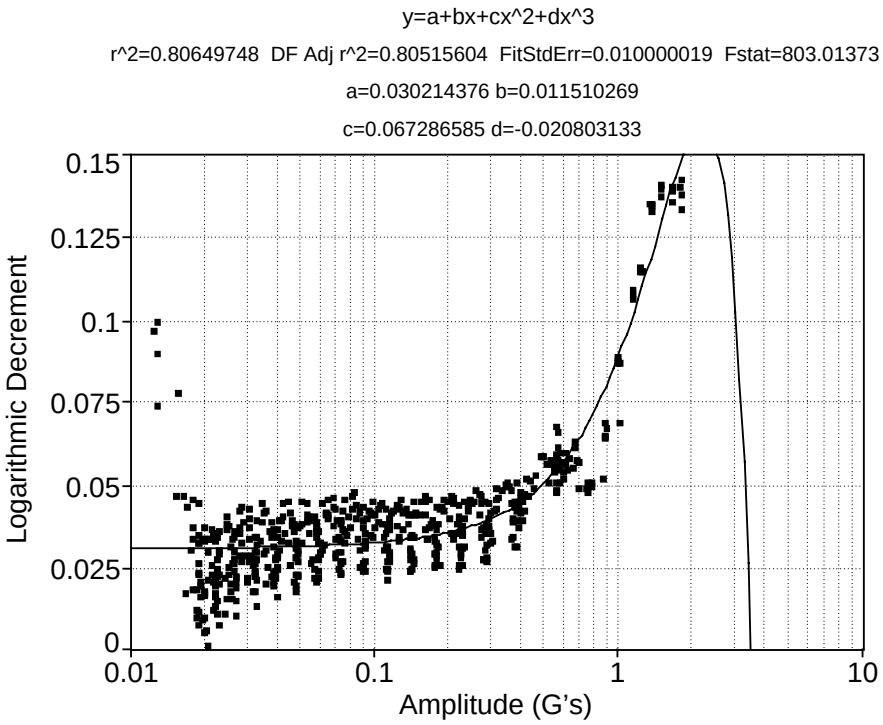

Fig. 120. Bend 1 test, upper peaks, in the 90° truss orientation using pin set three.

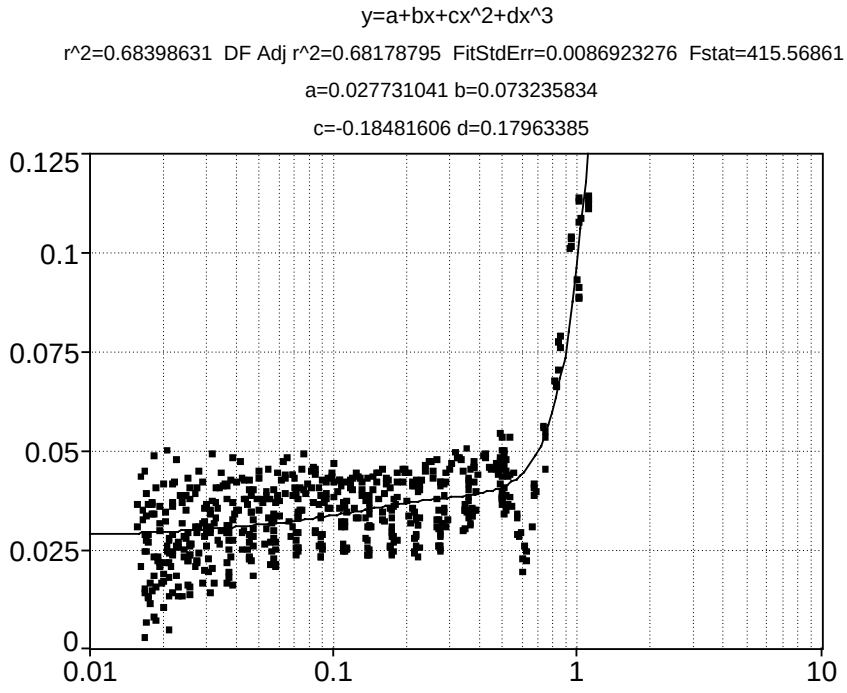

Fig. 121. Bend 1 test, lower peaks, in the 90° truss orientation using pin set three.

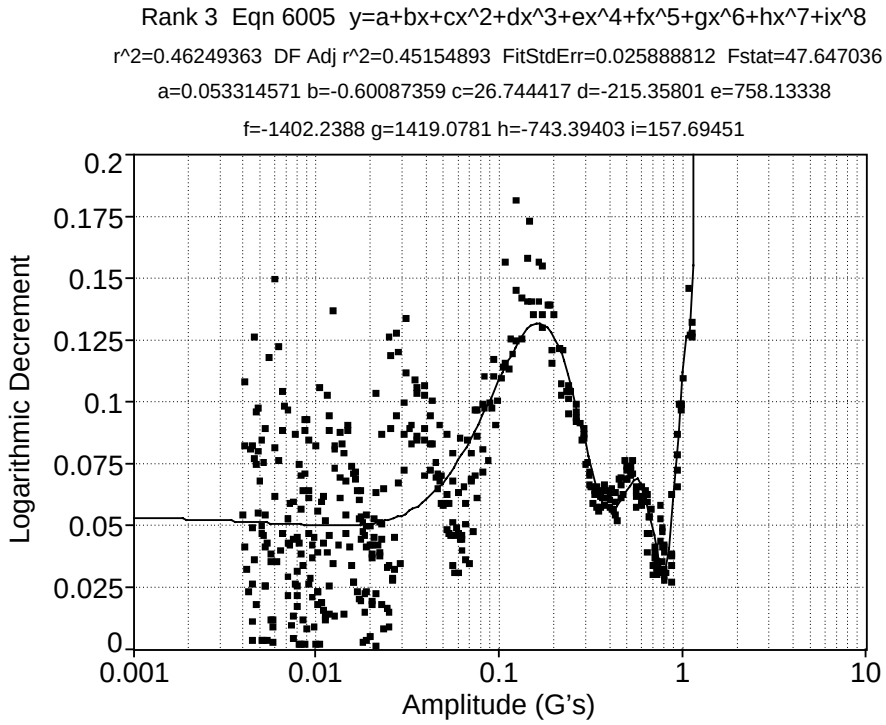

Fig. 122. Baseline bend 1 test, upper peaks, in the 90° truss orientation.

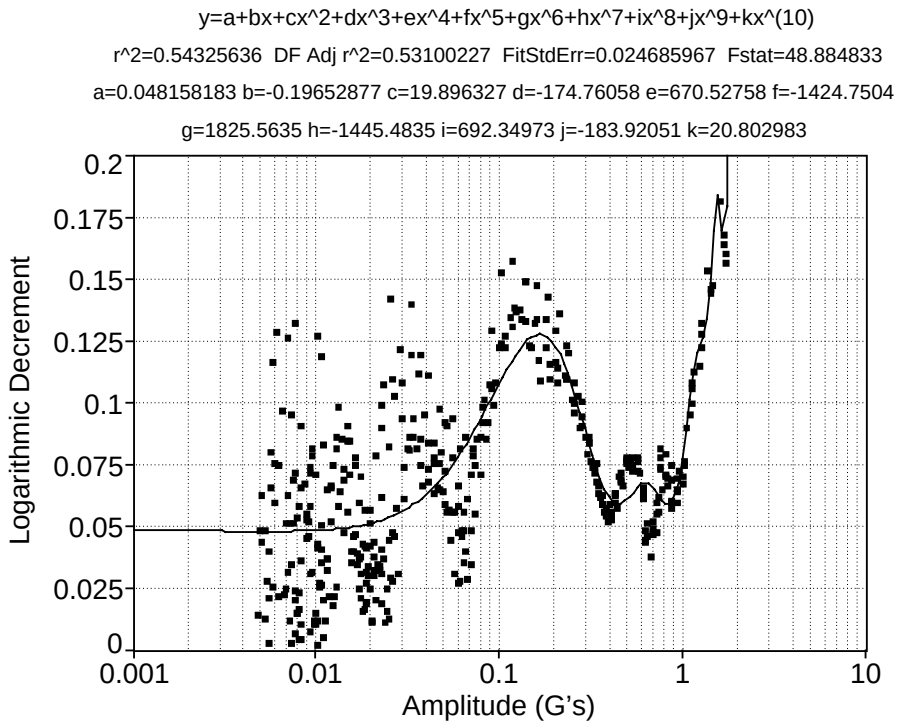

Fig. 123. Baseline bend 1 test, lower peaks, in the 90° truss orientation.

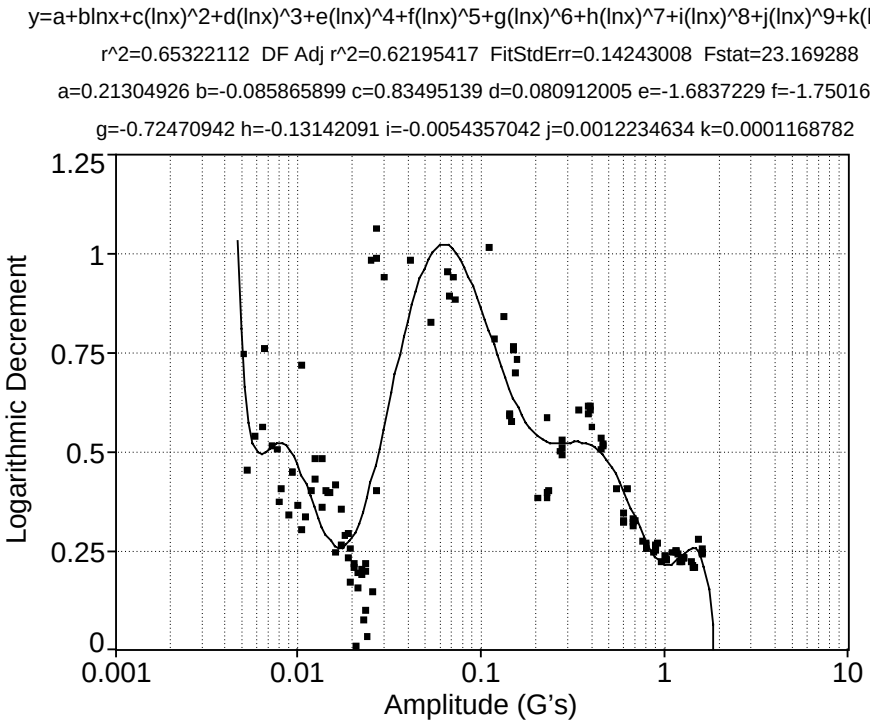

Fig. 124. Baseline bend 1 test in the 180° truss orientation.

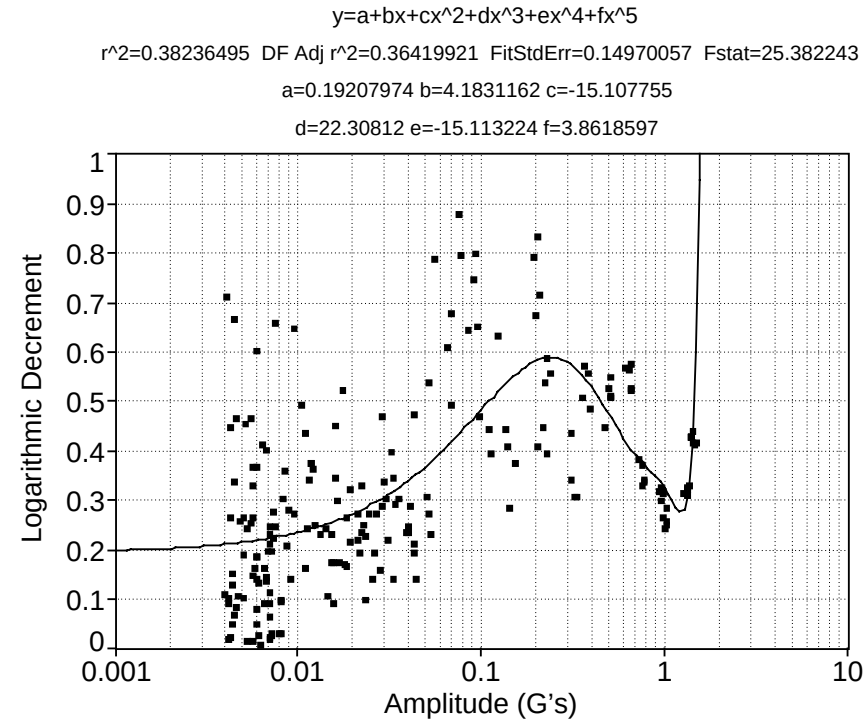

Fig. 125. Cold cell bend 1 test at 20° C.

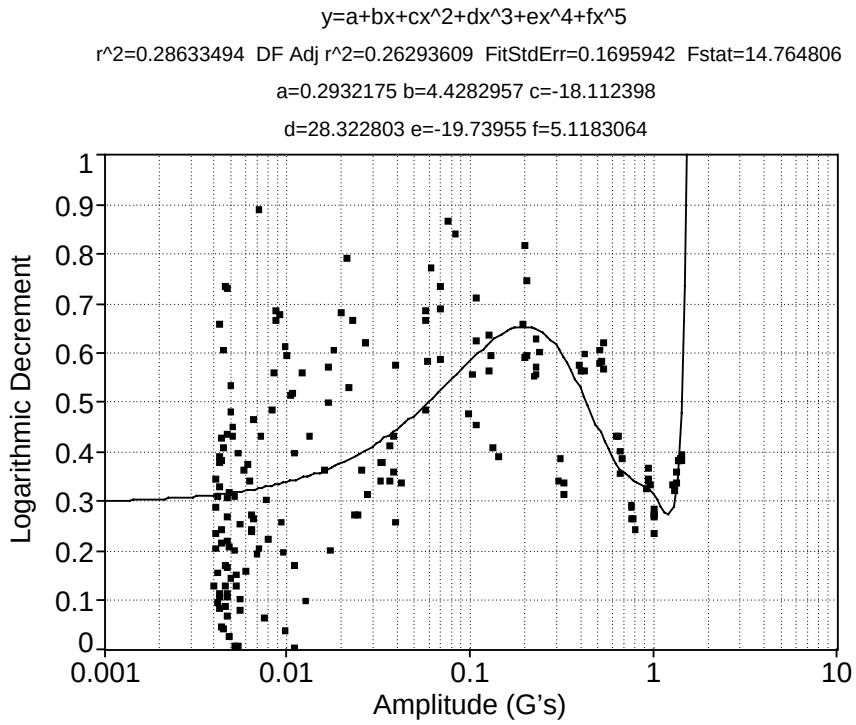

Fig. 126. Cold cell bend 1 test at 10° C.

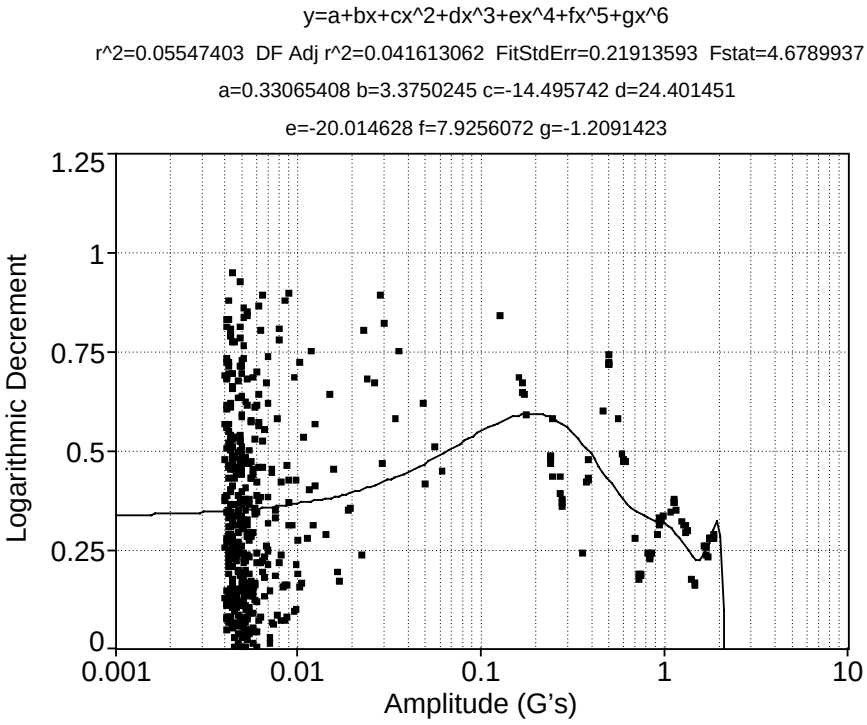

Fig. 127. Cold cell bend 1 test at 0° C.

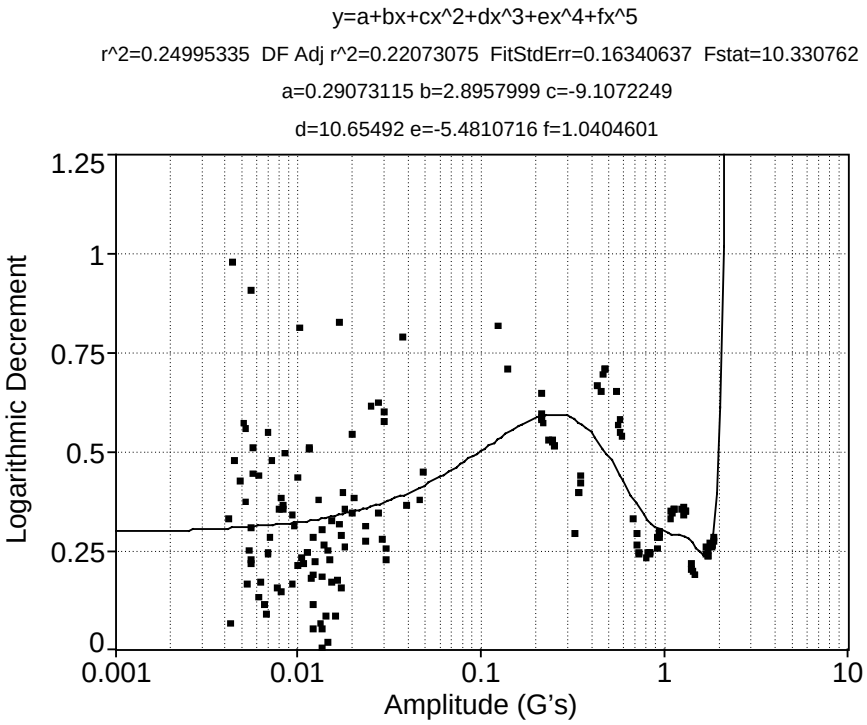

Fig. 128. Cold cell bend 1 test at -10° C.

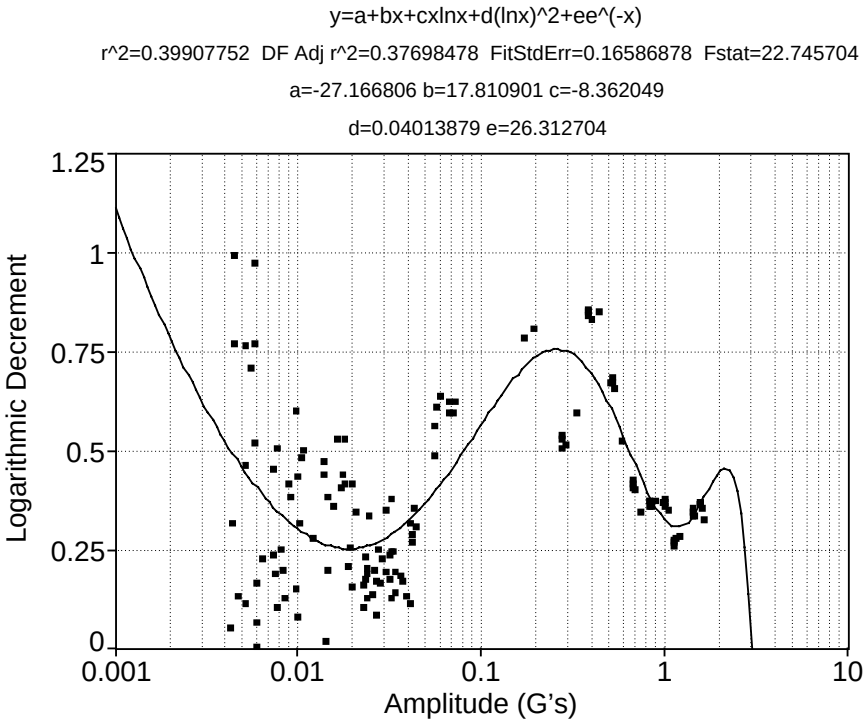

Fig. 129. Cold cell bend 1 test at -20° C.

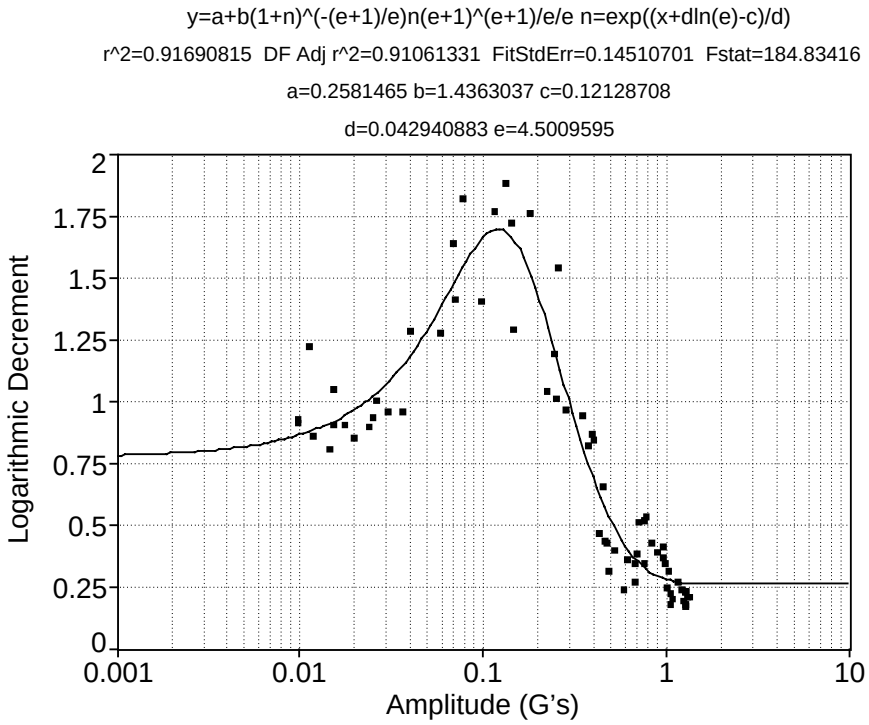

Fig. 130. Low-G bend 1 test.

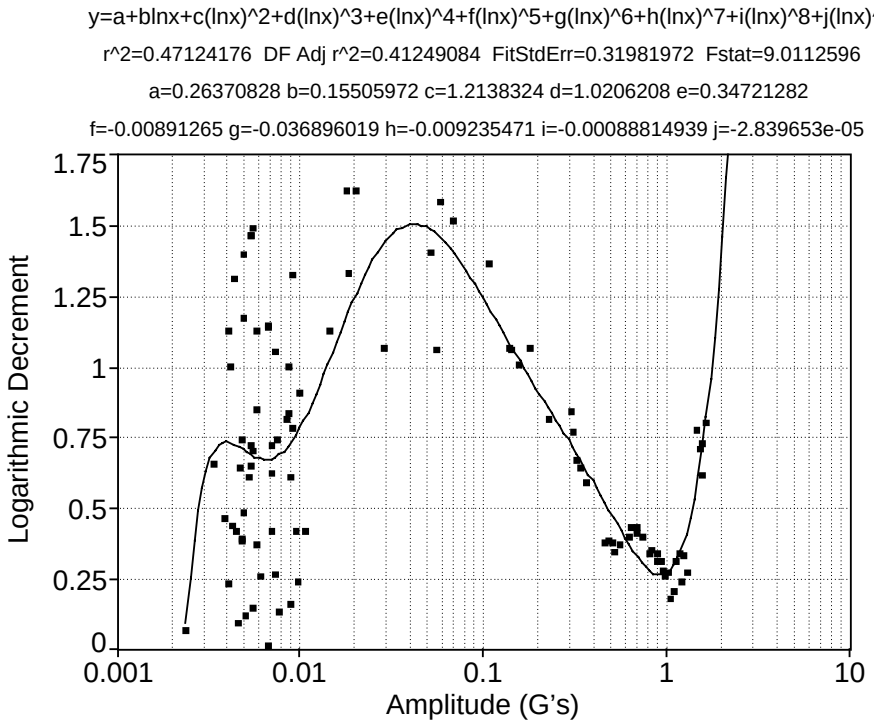

Fig. 131. Bend 1 test during the Space Shuttle flight.

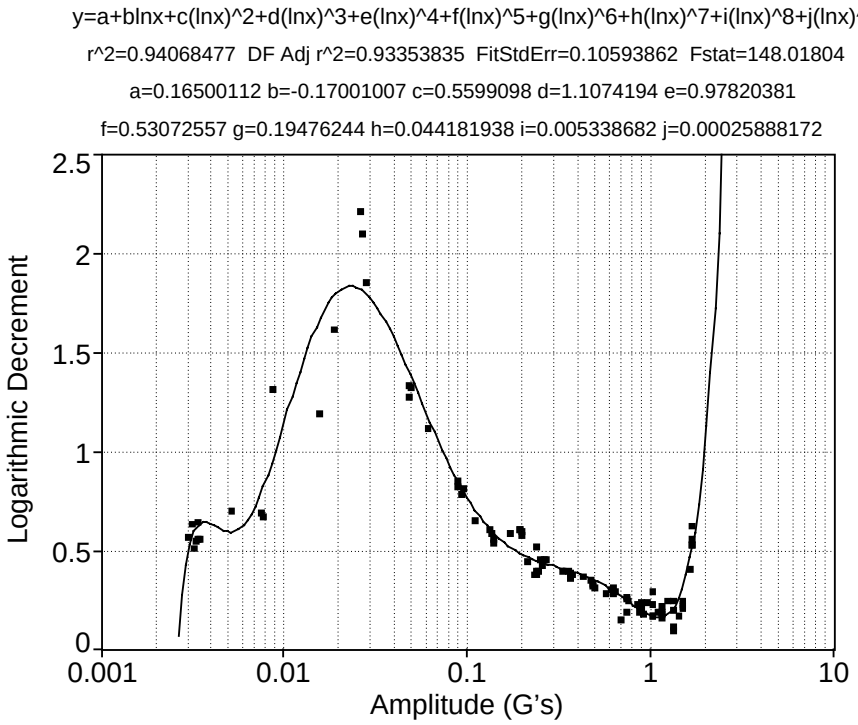

Fig. 132. Bend 1 post flight test in the 0° truss orientation.

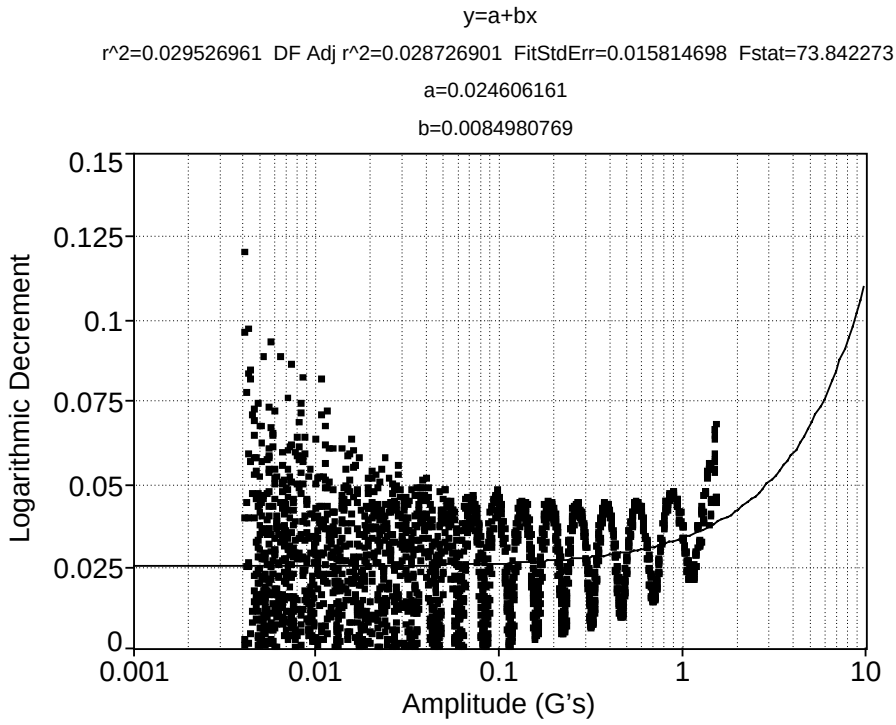

Fig. 133. Bend 2 test in the 0° truss orientation with all joints locked.

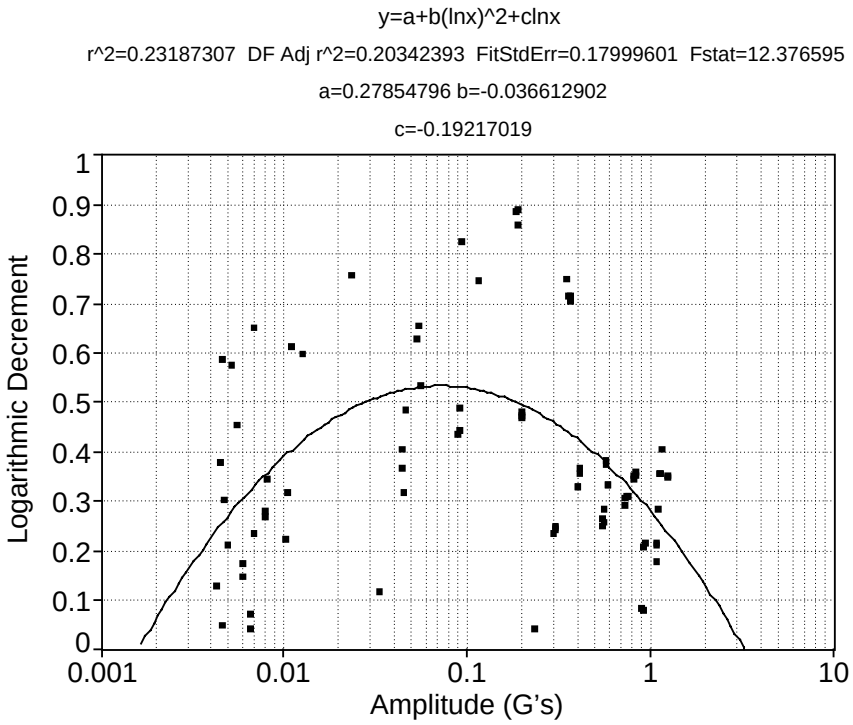

Fig. 134. Bend two test in the 0° truss orientation using pin set three.

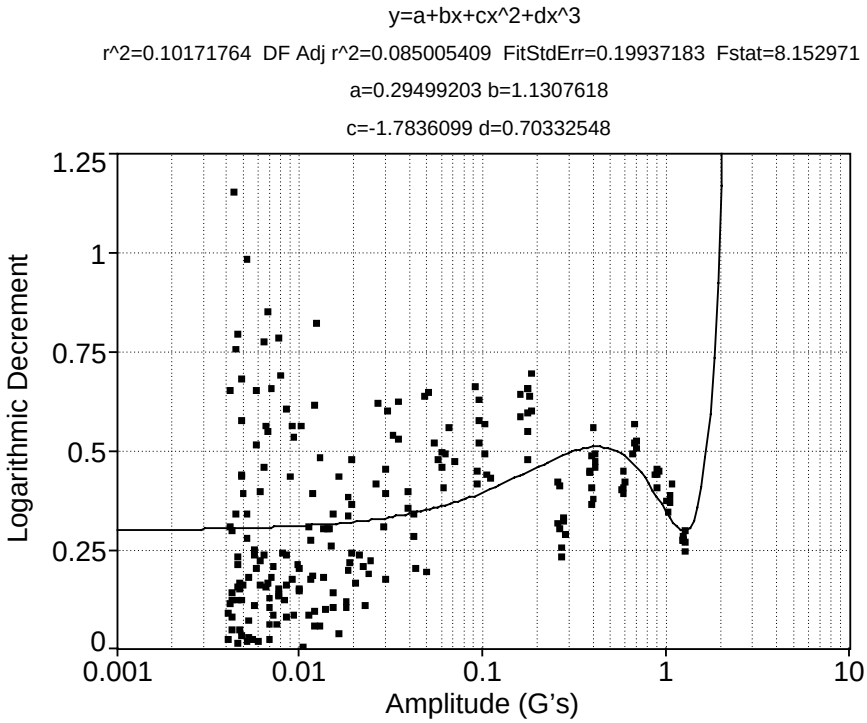

Fig. 135. Baseline bend 2 test in the 0° truss orientation.

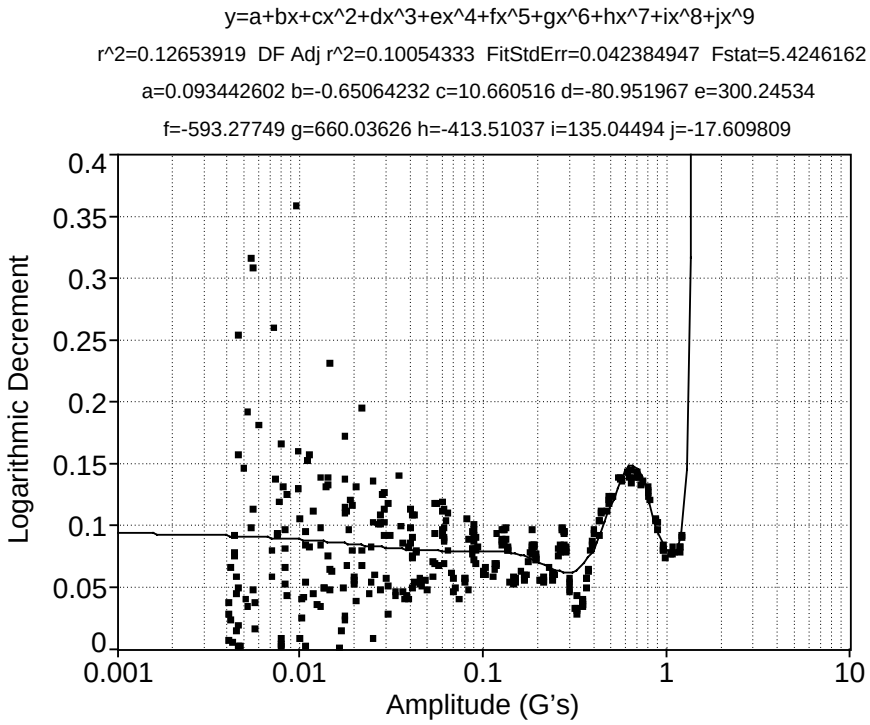

Fig. 136. Baseline bend 2 test, lower peaks, in the 90° truss orientation.

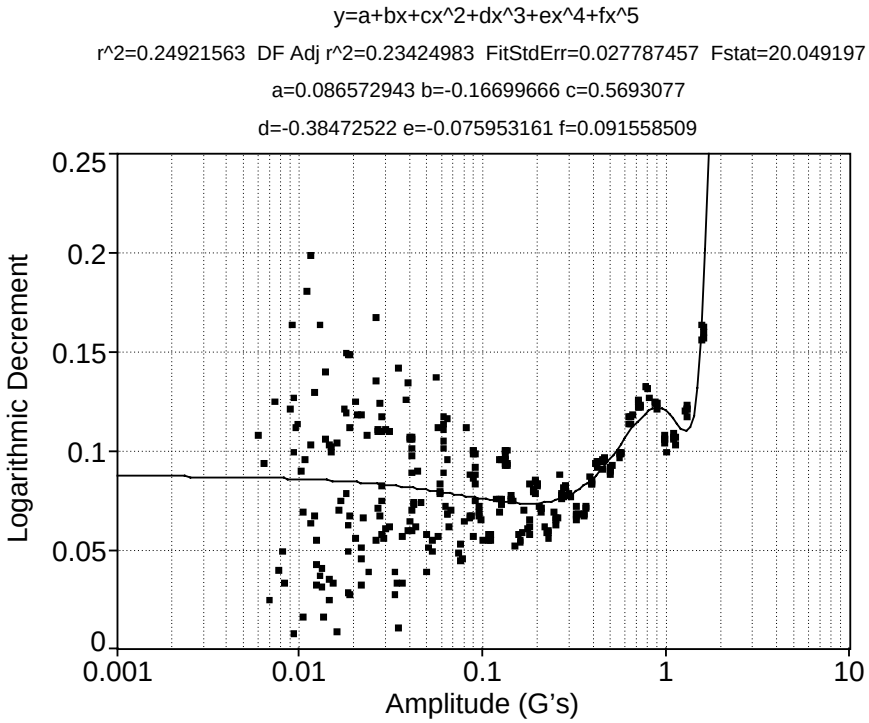

Fig. 137. Baseline bend 2 test, upper peaks, in the 90° truss orientation.

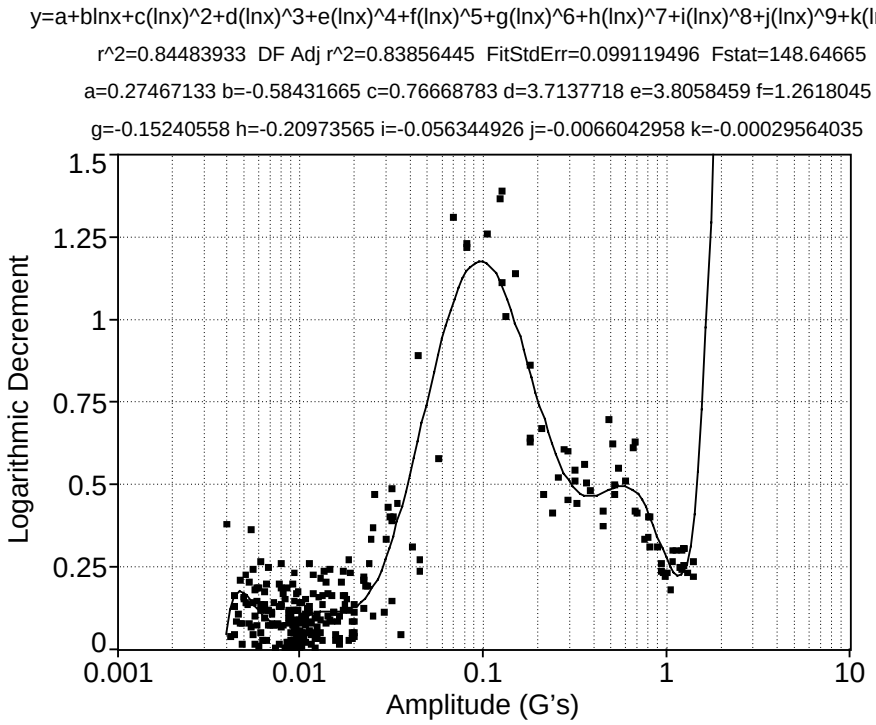

Fig. 138. Baseline bend 2 test in the 180° truss orientation.

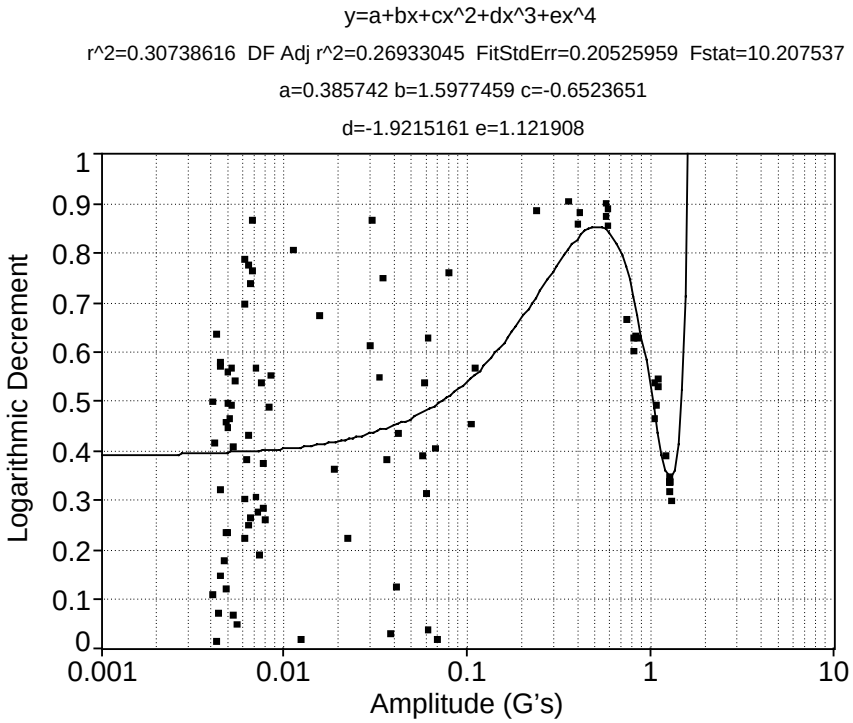

Fig. 139. Cold cell bend 2 test at 20° C.

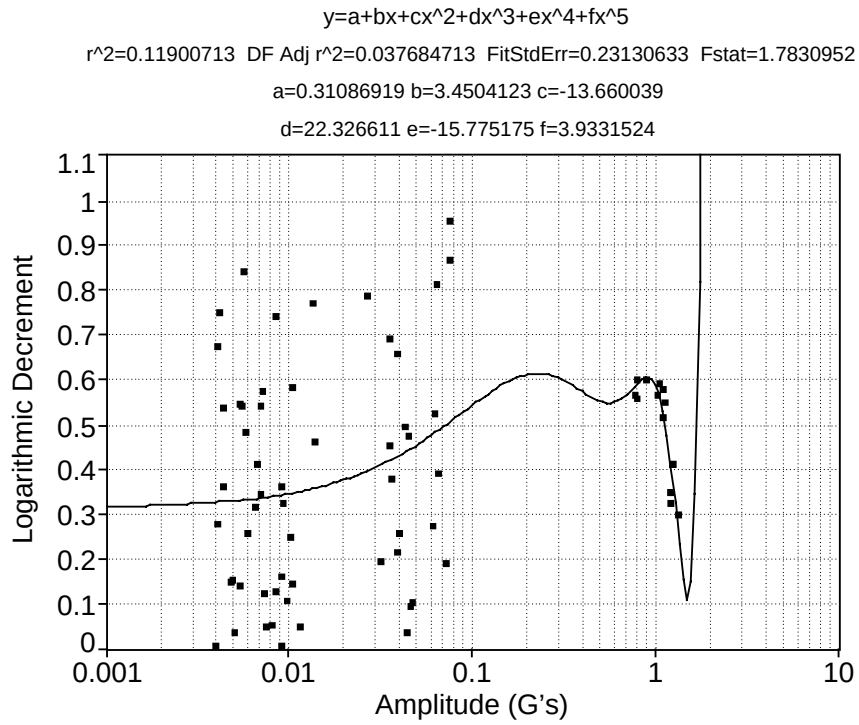

Fig. 140. Cold cell bend 2 test at 10° C.

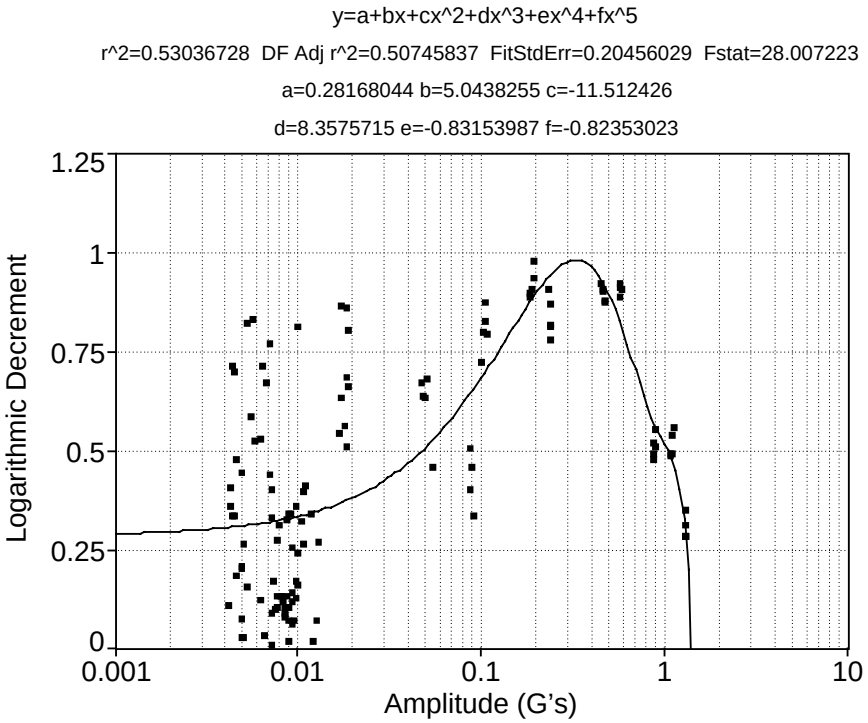

Fig. 141. Cold cell bend 2 test at 0° C.

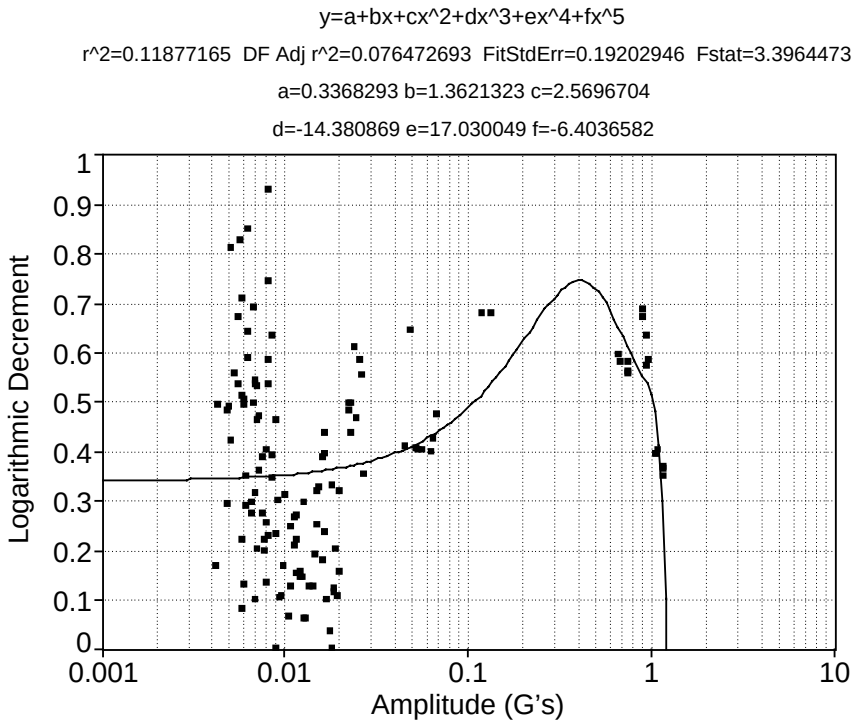

Fig. 142. Cold cell bend 2 test at -10° C.

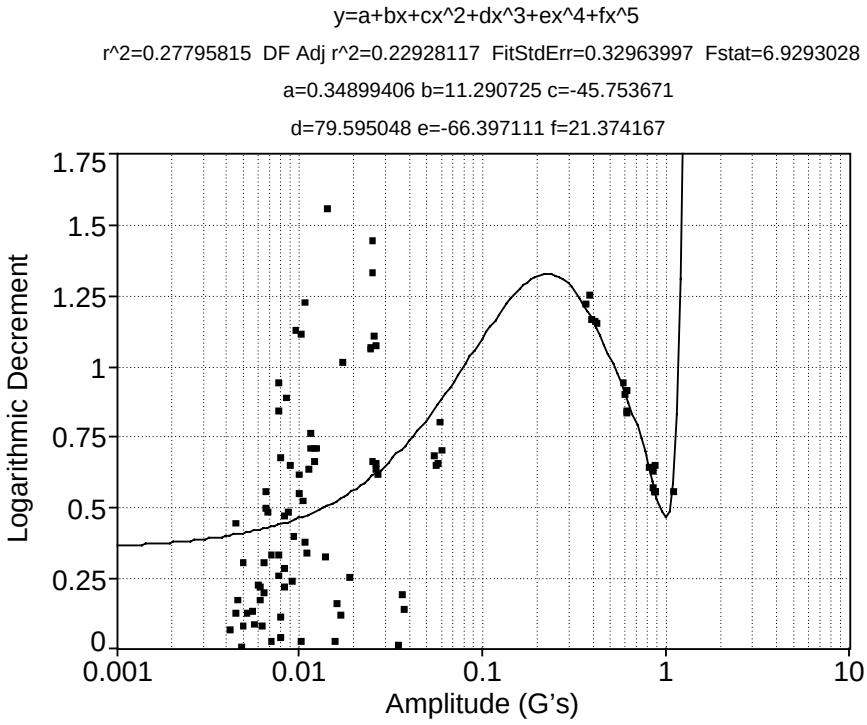

Fig. 143. Cold cell bend 2 test at -20° C.

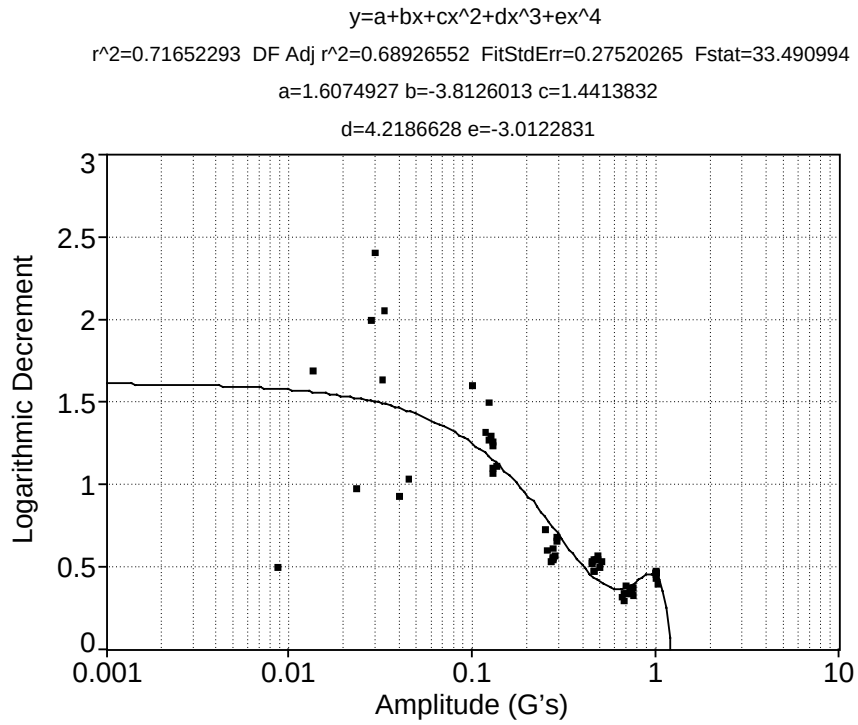

Fig. 144. Bend 2 test during a low-G flight.

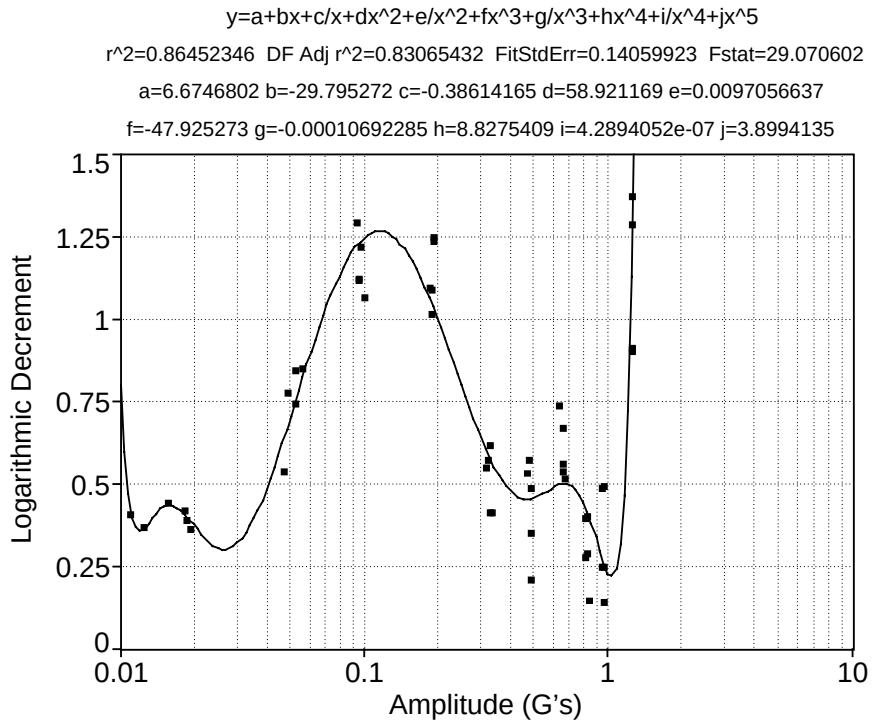

Fig. 145. Bend 2 test during the Space Shuttle flight.

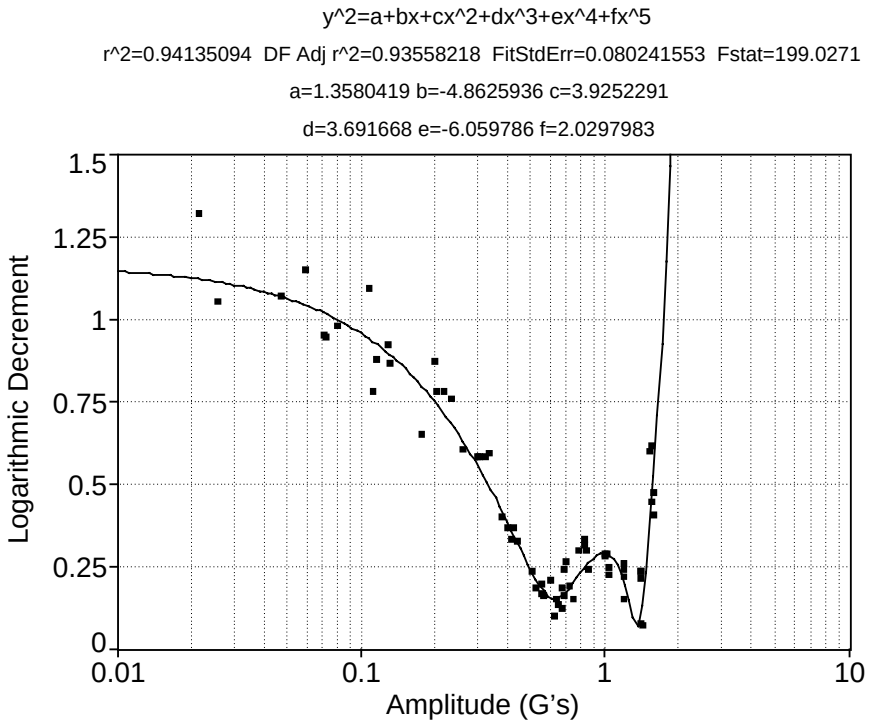

Fig. 146. Bend 2 post flight test in the 0° truss orientation.

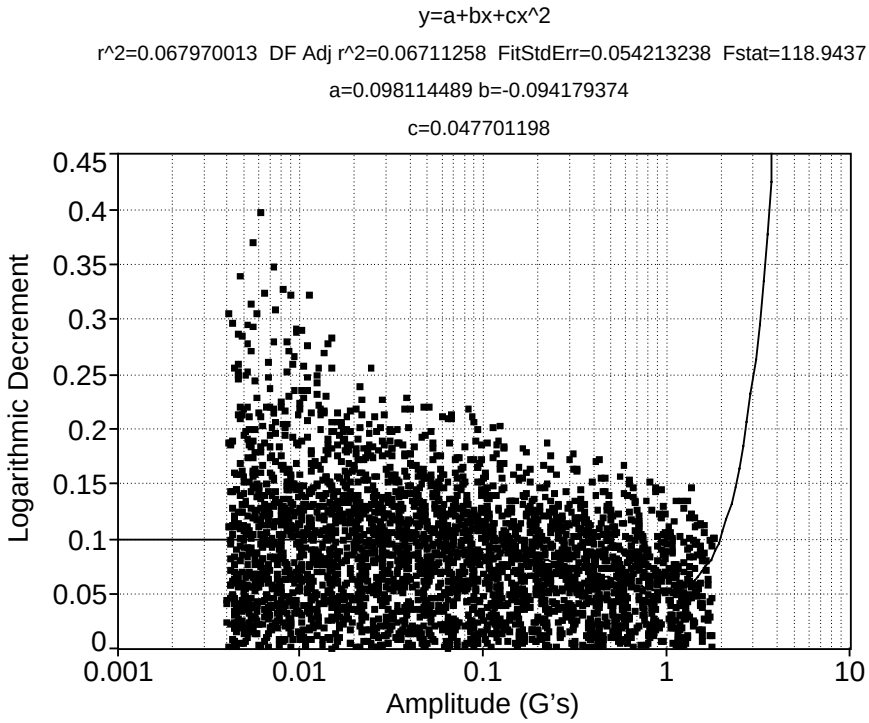

Fig. 147. Torsion test in the 0° truss orientation with all joints locked.

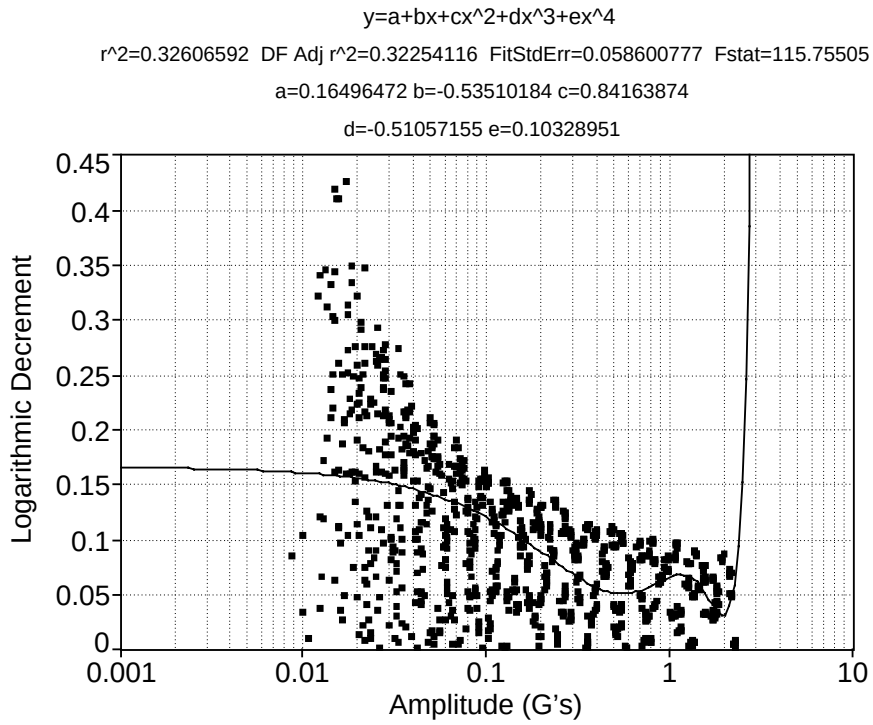

Fig. 148. Baseline torsion test, lower peaks, in the 90° truss orientation.

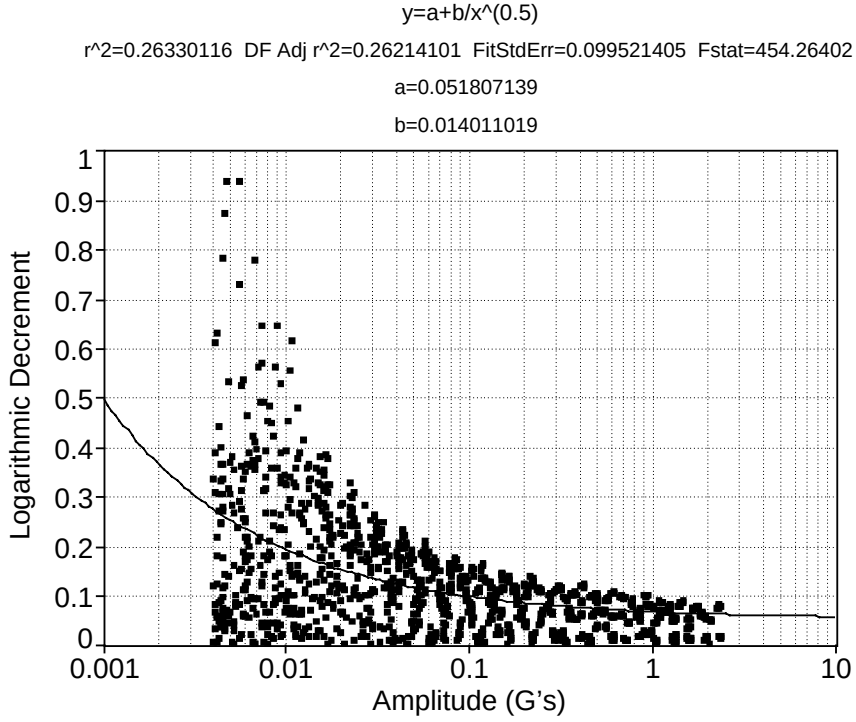

Fig. 149. Baseline torsion test, upper peaks, in the 90° truss orientation.